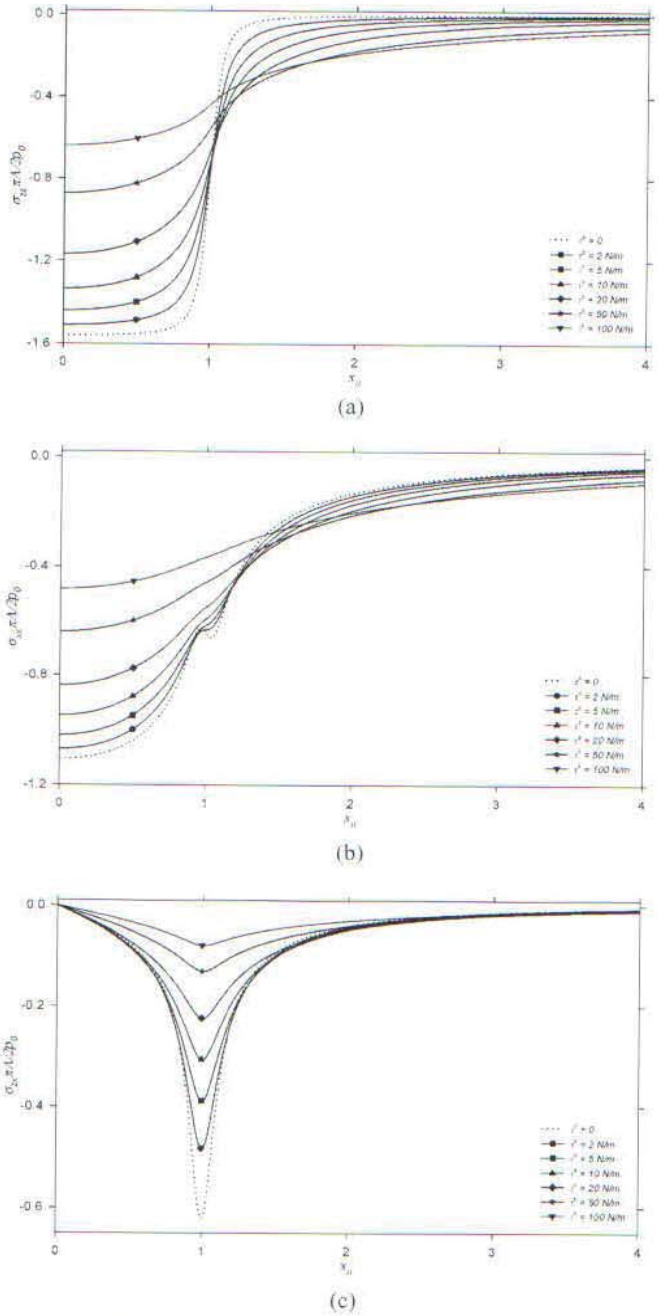

(a)

(b)

(c)

Fig. 5 Non-dimensional stress profiles at $z_0 = 0.1$ under vertical surface load for different residual surface stresses: (a) Vertical stress, (b) Horizontal stress, (c) Shear stress

vertical load p_0 and a horizontal load q_0 over a region $2a$ (with $a_0 = 1$) at the free surface are presented in Figs. 8 and 9 respectively. In this case, it is convenient to define the non-dimensional

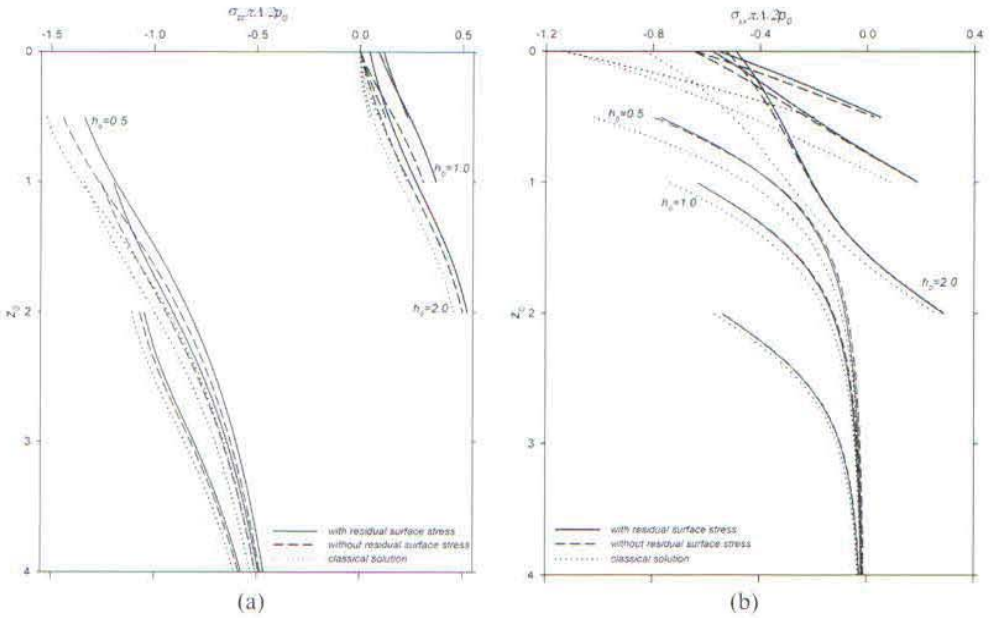

Fig. 6 Non-dimensional stress profiles along the z-axis of a half-plane under internal vertical load: (a) Vertical stress, (b) Horizontal stress

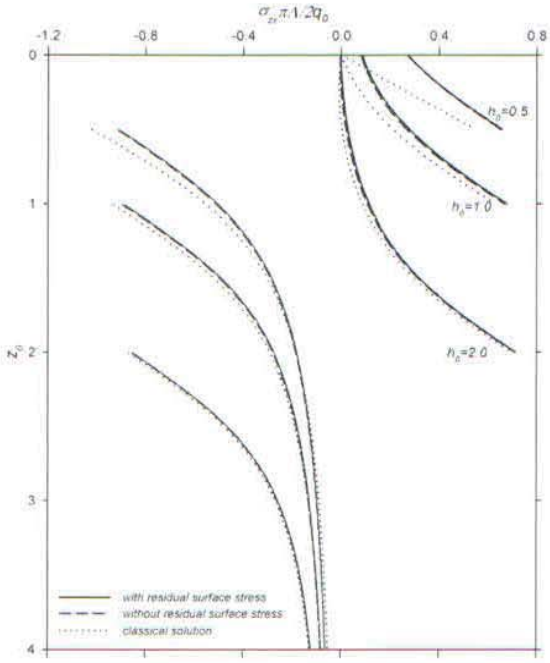

Fig. 7 Non-dimensional shear stress profiles along the z-axis of a half-plane under internal horizontal load

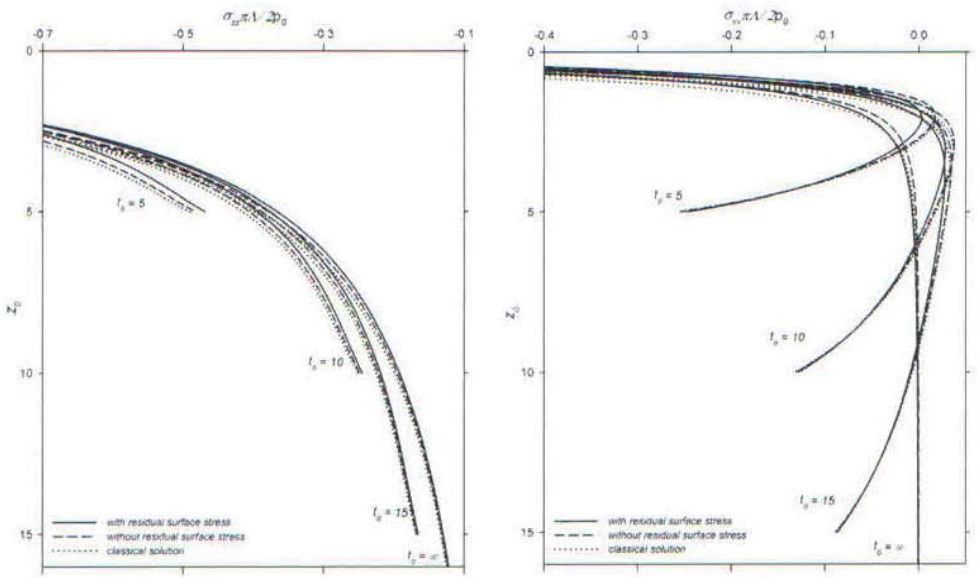

(a) (b)

Fig. 8 Non-dimensional stress profiles along the z-axis of a finite layer under vertical surface load: (a) Vertical stress, (b) Horizontal stress

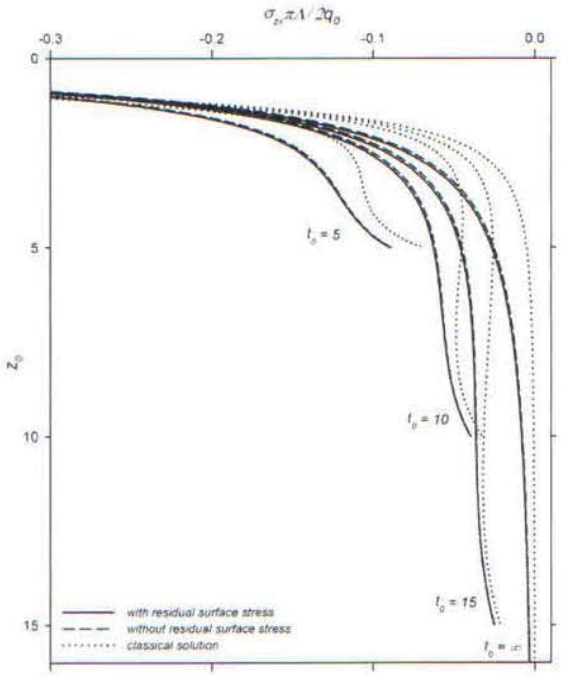

Fig. 9 Non-dimensional shear stress along the z-axis of a finite layer under horizontal surface load

layer thickness, $t_0 = t / \Lambda$. Once again, the residual surface stress shows more significant influence in the case of a vertical strip load when compared to a horizontal strip load. It is clear from these figures that the thickness of a layer has a significant influence on the stress field for both classical and non-classical cases. The stresses in both cases are mainly compressive and decrease with increasing layer thickness, except for the horizontal stresses under vertical strip load in Fig. 8(b), in which tensile stresses are also noted for layers with finite thickness. Numerical results shown in Figs. 2-9 confirm the fact that the influence of the residual surface stress should not be ignored in the analysis of the problems involving nanoscale layers or soft elastic materials.

5. Conclusions

A theoretical formulation based on the Gurtin-Murdoch continuum theory of elastic material surfaces is presented to study the elastic response of a nanoscale layer. An important aspect of the present study is the consideration of the out-of-plane term of the surface displacement gradient in the formulation. It is shown that the elastic field can be solved explicitly by using Fourier integral transform techniques. The final solution is expressed in terms of semi-infinite integrals that can be accurately computed by employing a numerical quadrature scheme. It is found from the analytical solution and numerical results that the effects of the surface energy on the elastic field are characterized by both the characteristic length parameter Λ that is related to the surface and bulk elastic moduli and the residual surface stress (τ^s). As expected, the influence of the surface elasticity and the residual surface stress becomes more significant in the vicinity of the layer surface. Numerical results also indicate that increasing Λ and τ^s result in a decrease in bulk stresses.

Acknowledgements

The work presented in this paper was supported by grants from the Thailand Research Fund and the Natural Sciences and Engineering Research Council of Canada.

References

Chen, C.S., Wang, C.K. and Chang, S.W. (2008), "Atomistic simulation and investigation of nanoindentation, contact pressure and nanohardness", *Interact. Multiscale Mech.*, **1**(4), 411-422.

Chen, J. and Lee, J.D. (2010), "Atomistic analysis of nano/micro biosensors", *Interact. Multiscale Mech.*, **3**(2), 111-121.

Dingreville, R. and Qu, J. (2007), "A semi-analytical method to compute surface elastic properties", *Acta Mater.*, **55**, 141-147.

Gurtin, M.E. and Murdoch, A.I. (1975), "A continuum theory of elastic material surfaces", *Arch. Rat. Mech. Anal.*, **57**, 291-323.

Gurtin, M.E. and Murdoch, A.I. (1978), "Surface stress in solids", *Int. J. Solids Struct.*, **14**, 431-440.

He, L.H. and Lim, C.W. (2006), "Surface green functions for a soft elastic half-space: influence of surface stress", *Int. J. Solids Struct.*, **43**, 132-143.

Huang, G.Y. and Yu, S.W. (2007), "Effect of surface elasticity on the interaction between steps", *J. Appl. Mech.*, **74**, 821-823.

Intarit, P., Senjuntichai, T. and Rajapakse, R.K.N.D. (2010), "Dislications and internal loading in a semi-infinite

elastic medium with surface stresses", *Eng. Fracture Mech.*, **77**, 3592-3603.
Miller, R.E. and Shenoy, V.B. (2000), "Size-dependent elastic properties of nanosized structural elements", *Nanotechnology*, **11**, 139-147.
Peters, R.D., Yang, X.M., Wang, Q., de Pablo, J.J. and Nealey, P.F. (2000), "Combining advanced lithographic techniques and self-assembly of thin films of diblock copolymers to produce templates for nanofabrication", *J. Vac. Sci. Technol. B*, **18**, 3530-3534.
Piessens, R., Doncker-Kapenga, E., Uberhuber, C.W. and Kahaner, D.K. (1983), *QUADPACK: A subroutine package for automatic integration*, Springer, Berlin.
Povstenko, Y.Z. (1993), "Theoretical investigation of phenomena caused by heterogeneous surface tension in solids", *J. Mech. Phys. Solids*, **41**, 1499-1514.
Shenoy, V.B. (2005), "Atomistic calculations of elastic properties of metallic fcc crystal surfaces", *Phys. Rev. B*, **71**, 094104.
Sneddon, I.N. (1951), *Fourier transforms*, McGraw-Hill, New York.
Srinivasan, U., Liepmann, D. and Howe, R.T. (2001), "Microstructure to substrate self-assembly using capillary forces", *J. Microelectromech. Syst.*, **10**, 17-24.
Wang, Z.Q., Zhao, Y.P. and Huang, Z.P. (2010), "The effects of surface tension on the elastic properties of nano structures", *Int. J. Eng. Sci.*, **48**, 140-150.
Wong, E., Sheehan, P.E. and Lieber, C.M. (1997), "Nanobeam mechanics: elasticity, strength and toughness of nanorods and nanotubes", *Science*, **277**, 1971-1975.
Yakobson, B.I., *Nanomechanics*, In: Goddard, W.A., Brenner, D.W., Lyshevsk, S.E. and Iafrate, G.J. editors. (2003), *Handbook of nanoscience, engineering and technology*, CRC Press, Boca Raton.
Zhao, X.J. and Rajapakse R.K.N.D. (2009) "Analytical solutions for a surface-loaded isotropic elastic layer with surface energy effects", *Int. J. Eng. Sci.*, **47**, 1433-1444.

Appendix

The expressions of A_i to H_i ($i = p, q$) and I appearing in Eqs. (30) - (34) are given as follows:

$$A_p = \left\{ \begin{array}{l} (\lambda+3\mu)\left[\left(\frac{\lambda+\mu}{\lambda+2\mu}h+\Lambda\right)|\xi|\cosh\left(\xi(2t-h)\right)+\left(1+\frac{\lambda+\mu}{\lambda+2\mu}\Lambda h\xi^2\right)\sinh\left(|\xi|(2t-h)\right)\right] \\ -(\lambda+\mu)\left[\left(2t+\frac{\lambda+3\mu}{\lambda+\mu}\Lambda-\frac{\lambda+\mu}{\lambda+2\mu}\left(2t(t-h)\Lambda\xi^2+h\right)\right)|\xi|\cosh\left(\xi h\right)+\left(\frac{\lambda+3\mu}{\lambda+\mu}+\frac{\lambda+\mu}{\lambda+2\mu}\left(2t(t-h)-\Lambda h\right)\xi^2+2\Lambda t\xi^2\right)\sinh\left(|\xi|h\right)\right] \\ -\frac{\tau^s}{2\mu}|\xi|\left\{(\lambda+3\mu)\left[\left(\frac{\lambda+3\mu}{\lambda+2\mu}\Lambda+h\right)|\xi|\cosh\left(\xi(2t-h)\right)+\frac{\lambda+2\mu}{\lambda+\mu}\sinh\left(|\xi|(2t-h)\right)+\frac{(\lambda+\mu)^2}{2(\lambda+2\mu)^2}\left(e^{|\xi|(2t-h)}-\frac{\lambda+3\mu}{\lambda+\mu}e^{-|\xi|(2t-h)}\right)\Lambda h\xi^2\right]\right. \\ +(\lambda+\mu)\left[\left(h-\frac{2(\lambda+2\mu)}{\lambda+\mu}t-\frac{\lambda+3\mu}{\lambda+2\mu}\left(\frac{\lambda+3\mu}{\lambda+\mu}+2t|\xi|\right)\Lambda\right)|\xi|\cosh\left(\xi h\right)-\left(\frac{(\lambda+2\mu)(\lambda+3\mu)}{(\lambda+\mu)^2}+2t(t-h)\xi^2\right)\sin\left(|\xi|h\right)\right] \\ \left.+\frac{(\lambda+\mu)^3}{(\lambda+2\mu)^2}\Lambda\xi^2\left[\frac{(\lambda+3\mu)^2}{2(\lambda+\mu)^2}h-\left(t(t-h)|\xi|\right)e^{|\xi|h}-\frac{\lambda+3\mu}{2(\lambda+\mu)}\left(2t(t-h)|\xi|+h\right)e^{-|\xi|h}\right]\right\} \end{array} \right\} \frac{\overline{p}(\xi)}{2\xi^2} \tag{A.1}$$

$$B_p = \left\{ \begin{array}{l} (\lambda+\mu)(\lambda+3\mu)\left[2\Lambda|\xi|\left(\cosh\left(\xi(2t-h)\right)-\cosh\left(\xi h\right)\right)+\left(2h|\xi|+\frac{\lambda+3\mu}{\lambda+\mu}\right)e^{|\xi|(2t-h)}-e^{-|\xi|(2t-h)}-\left(\frac{\lambda+3\mu}{\lambda+\mu}+2t|\xi|\right)e^{|\xi|h}\right] \\ +(\lambda+\mu)^2\left[4(t-h)\left(\Lambda\sinh\left(|\xi|h\right)-te^{|\xi|h}\right)\xi^2+\left(\frac{\lambda+3\mu}{\lambda+\mu}-2(t-h)|\xi|\right)e^{-|\xi|h}\right] \\ -\frac{\tau^s}{2\mu}|\xi|\left\{(\lambda+3\mu)\left[\frac{2(\lambda+\mu)(\lambda+3\mu)}{(\lambda+2\mu)}\Lambda|\xi|\cosh\left(\xi(2t-h)\right)+2(\lambda+2\mu)\left(\sinh\left(|\xi|(2t-h)\right)+\sinh\left(|\xi|h\right)\right)\right]\right. \\ -2(\lambda+\mu)\left[2(\lambda+2\mu)(t-h)+\frac{(\lambda+3\mu)^2}{\lambda+2\mu}\Lambda\right]|\xi|\cosh\left(\xi h\right)+\frac{2(\lambda+\mu)^2(\lambda+3\mu)}{\lambda+2\mu}\Lambda h\xi^2e^{|\xi|(2t-h)} \\ \left.-\frac{2(\lambda+\mu)^2}{\lambda+2\mu}\Lambda\xi^2\left[\left((\lambda+3\mu)t+2(\lambda+\mu)t(t-h)|\xi|\right)e^{|\xi|h}-(\lambda+3\mu)(t-h)e^{-|\xi|h}\right]\right\} \end{array} \right\} \frac{\overline{p}(\xi)}{4(\lambda+2\mu)|\xi|} \tag{A.2}$$

$$C_p = -\left\{ \begin{array}{l} (\lambda+3\mu)\left[\left(\frac{\lambda+\mu}{\lambda+2\mu}h+\Lambda\right)|\xi|\cosh\left(\xi(2t-h)\right)+\left(1+\frac{\lambda+\mu}{\lambda+2\mu}\Lambda h\xi^2\right)\sinh\left(|\xi|(2t-h)\right)\right] \\ -(\lambda+\mu)\left[\left(2t+\frac{\lambda+3\mu}{\lambda+\mu}\Lambda+\frac{\lambda+\mu}{\lambda+2\mu}\left(2t(t-h)\Lambda\xi^2-h\right)\right)|\xi|\cosh\left(\xi h\right)+\left(\frac{\lambda+3\mu}{\lambda+\mu}+\frac{\lambda+\mu}{\lambda+2\mu}\left(2t(t-h)-\Lambda h\right)\xi^2+2\Lambda t\xi^2\right)\sinh\left(|\xi|h\right)\right] \\ +\frac{\tau^s}{2\mu}|\xi|\left\{(\lambda+3\mu)\left[\left(\frac{\lambda+3\mu}{\lambda+2\mu}\Lambda+h\right)|\xi|\cosh\left(\xi(2t-h)\right)+\frac{\lambda+2\mu}{\lambda+\mu}\sinh\left(|\xi|(2t-h)\right)+\frac{(\lambda+\mu)^2}{2(\lambda+2\mu)^2}\left(\frac{\lambda+3\mu}{\lambda+\mu}e^{|\xi|(2t-h)}-e^{|\xi|(2t-h)}\right)\Lambda h\xi^2\right]\right. \\ +(\lambda+\mu)\left[\left(h|\xi|-\frac{2(\lambda+2\mu)}{(\lambda+\mu)}t|\xi|-\frac{\lambda+3\mu}{\lambda+\mu}\left(\frac{\lambda+3\mu}{\lambda+2\mu}\Lambda|\xi|-\frac{\lambda+2\mu}{\lambda+\mu}\right)\right)\cosh\left(\xi h\right)-\left(2(t-h)+\frac{2(\lambda+3\mu)}{\lambda+2\mu}\Lambda\right)t\xi^2\sin\left(|\xi|h\right)\right] \\ \left.-\frac{(\lambda+\mu)^3}{(\lambda+2\mu)^2}\Lambda\xi^2\left[\frac{\lambda+3\mu}{\lambda+\mu}\left(t(t-h)|\xi|-\frac{\lambda+3\mu}{2(\lambda+\mu)}h\right)e^{|\xi|h}+\left(\frac{(\lambda+3\mu)^2}{2(\lambda+\mu)^2}h-t(t-h)|\xi|\right)e^{-|\xi|h}\right]\right\} \end{array} \right\} \frac{\overline{p}(\xi)}{2\xi^2} \tag{A.3}$$

$$D_p = \left\{ \begin{array}{l} (\lambda+\mu)(\lambda+3\mu)\left[2\Lambda|\xi|\left(\cosh\left(\xi(2t-h)\right)-\cosh\left(\xi h\right)\right)+e^{|\xi|(2t-h)}+\left(2h|\xi|-\frac{\lambda+3\mu}{\lambda+\mu}\right)e^{-|\xi|(2t-h)}+\left(\frac{\lambda+3\mu}{\lambda+\mu}-2t|\xi|\right)e^{-|\xi|h}\right] \\ -(\lambda+\mu)^2\left[4(t-h)\left(\Lambda\sinh\left(|\xi|h\right)-te^{-|\xi|h}\right)\xi^2+\left(\frac{\lambda+3\mu}{\lambda+\mu}+2(t-h)|\xi|\right)e^{|\xi|h}\right] \\ +\frac{\tau^s}{2\mu}|\xi|\left\{(\lambda+3\mu)\left[\frac{2(\lambda+\mu)(\lambda+3\mu)}{(\lambda+2\mu)}\Lambda|\xi|\cosh\left(\xi(2t-h)\right)+2(\lambda+2\mu)\sinh\left(|\xi|(2t-h)\right)\right]\right. \\ -2(\lambda+\mu)\left[2(\lambda+2\mu)(t-h)+\frac{(\lambda+3\mu)^2}{\lambda+2\mu}\Lambda\right]|\xi|\cosh\left(\xi h\right)-\frac{2(\lambda+\mu)^2(\lambda+3\mu)}{\lambda+2\mu}\Lambda h\xi^2e^{-|\xi|(2t-h)} \\ \left.-\frac{2(\lambda+\mu)^2}{\lambda+2\mu}\Lambda\xi^2\left[\left((\lambda+3\mu)(t-h)+2(\lambda+\mu)t(t-h)|\xi|\right)e^{|\xi|h}-\left((\lambda+3\mu)t-2(\lambda+\mu)t(t-h)|\xi|\right)e^{-|\xi|h}\right]\right\} \end{array} \right\} \frac{\overline{p}(\xi)}{4(\lambda+2\mu)|\xi|} \tag{A.4}$$

$$E_p=\left\{\begin{array}{l}(\lambda+3\mu)(1+\Lambda|\xi|)\left[\left(1-\frac{\lambda+\mu}{\lambda+2\mu}h|\xi|\right)e^{|\xi|(2t+h)}+\left(1+\frac{\lambda+\mu}{\lambda+2\mu}h|\xi|\right)e^{|\xi|(2t-h)}\right]+(\lambda+\mu)(1-\Lambda|\xi|)\left[\frac{\lambda+3\mu}{\lambda+\mu}-2t|\xi|+\frac{\lambda+\mu}{\lambda+2\mu}(2t(t+h)|\xi|+h)|\xi|\right]e^{-|\xi|h}\\ +\left[\frac{\lambda^2+4\lambda\mu+7\mu^2}{\lambda+\mu}-(\lambda+3\mu)\left(\frac{\lambda+3\mu}{\lambda+2\mu}h+\Lambda\right)|\xi|-(\lambda+\mu)\left(2(1-\Lambda|\xi|)-\frac{2(\lambda+3\mu)}{\lambda+2\mu}t|\xi|\right)t|\xi|+\frac{(\lambda+\mu)^2}{\lambda+2\mu}\left(2th(1-2|\xi|t)-\Lambda\left(2t(t+h)|\xi|-h\right)\right)\xi^2\right]e^{|\xi|h}\\ +\frac{\tau^s}{2\mu}|\xi|\left\{(\lambda+3\mu)\left[\left(\frac{\lambda+2\mu}{\lambda+\mu}+\frac{\lambda+3\mu}{\lambda+2\mu}\Lambda|\xi|\right)\left(1-\frac{\lambda+\mu}{\lambda+2\mu}h|\xi|\right)e^{|\xi|(2t+h)}-\left(\frac{\lambda+2\mu}{\lambda+\mu}+h|\xi|+\frac{\lambda+3\mu}{\lambda+2\mu}\Lambda|\xi|+\frac{(\lambda+\mu)^2}{(\lambda+2\mu)^2}\Lambda h\xi^2\right)e^{|\xi|(2t-h)}\right]\right.\\ +(\lambda+\mu)\left[\left(2t(t+h)|\xi|-h\right)|\xi|+\frac{\lambda+2\mu}{\lambda+\mu}\left(\frac{\lambda+3\mu}{\lambda+\mu}-2t|\xi|\right)-\frac{\lambda+3\mu}{\lambda+2\mu}\left(\frac{\lambda+3\mu}{\lambda+\mu}-2t|\xi|-\frac{\lambda+3\mu}{\lambda+2\mu}h|\xi|+\frac{2(\lambda+\mu)}{\lambda+2\mu}t^2\xi^2\right)\Lambda|\xi|-\frac{2(\lambda+\mu)^2}{(\lambda+2\mu)^2}(1-2|\xi|t)\Lambda th|\xi|^3\right]e^{|\xi|h}\\ \left.-(\lambda+\mu)\left[\left(2t(t-h)|\xi|+h\right)|\xi|+\frac{\lambda+2\mu}{\lambda+\mu}\left(\frac{\lambda+3\mu}{\lambda+\mu}-2t|\xi|\right)-\frac{\lambda+3\mu}{\lambda+2\mu}\left(\frac{\lambda+3\mu}{\lambda+\mu}-2t|\xi|+\frac{\lambda+\mu}{\lambda+2\mu}(2t(t-h)|\xi|+h)|\xi|\right)\Lambda|\xi|\right]e^{-|\xi|h}\right\}\end{array}\right\}\frac{\overline{p}(\xi)}{4\xi^2} \tag{A.5}$$

$$F_p=\left\{\begin{array}{l}(\lambda+\mu)(\lambda+3\mu)\left[(1+\Lambda|\xi|)e^{|\xi|(2t+h)}+\left(\frac{\lambda+3\mu}{\lambda+\mu}+(\Lambda+2h)|\xi|\right)e^{|\xi|(2t-h)}\right]\\ +(\lambda+\mu)^2\left[1-\frac{\lambda+3\mu}{\lambda+\mu}(\Lambda+2t)|\xi|+\left(2\Lambda(t+h)+4th\right)\xi^2\right]e^{|\xi|h}+(\lambda+\mu)(1-\Lambda|\xi|)\left[\lambda+3\mu-2(\lambda+\mu)(t-h)|\xi|\right]e^{-|\xi|h}\\ +\frac{\tau^s}{2\mu}|\xi|\left\{(\lambda+3\mu)\left[\left(\lambda+2\mu+\frac{(\lambda+\mu)(\lambda+3\mu)}{\lambda+2\mu}\Lambda|\xi|\right)e^{|\xi|(2t+h)}-\left(\lambda+2\mu+\frac{(\lambda+\mu)^2}{\lambda+2\mu}\left(\frac{(\lambda+3\mu)}{\lambda+\mu}+2h|\xi|\right)\Lambda|\xi|\right)e^{|\xi|(2t-h)}\right]\right.\\ +(\lambda+\mu)\left[(\lambda+2\mu)\left(\frac{\lambda+3\mu}{\lambda+\mu}-2(t+h)|\xi|\right)-\frac{\lambda+3\mu}{\lambda+2\mu}\left(\lambda+3\mu-2(\lambda+\mu)t|\xi|\right)\Lambda|\xi|-\frac{2(\lambda+\mu)^2}{\lambda+2\mu}\Lambda th|\xi|^3\right]e^{|\xi|h}\\ \left.-(\lambda+\mu)\left[(\lambda+2\mu)\left(\frac{\lambda+3\mu}{\lambda+\mu}-2(t-h)|\xi|\right)-\frac{\lambda+3\mu}{\lambda+2\mu}\left(\lambda+3\mu-2(\lambda+\mu)(t-h)|\xi|\right)\Lambda|\xi|\right]e^{-|\xi|h}\right\}\end{array}\right\}\frac{\overline{p}(\xi)}{4(\lambda+2\mu)|\xi|} \tag{A.6}$$

$$G_p=\left\{\begin{array}{l}(\lambda+3\mu)(1-\Lambda|\xi|)\left[\left(1+\frac{\lambda+\mu}{\lambda+2\mu}h|\xi|\right)e^{-|\xi|(2t+h)}+\left(1-\frac{\lambda+\mu}{\lambda+2\mu}h|\xi|\right)e^{-|\xi|(2t-h)}\right]+(\lambda+\mu)(1+\Lambda|\xi|)\left[\frac{\lambda+3\mu}{\lambda+\mu}+2t|\xi|+\frac{\lambda+\mu}{\lambda+2\mu}\left(2t(t-h)|\xi|-h\right)|\xi|\right]e^{|\xi|h}\\ +\left[\frac{\lambda^2+4\lambda\mu+7\mu^2}{\lambda+\mu}+(\lambda+3\mu)\left(\frac{\lambda+3\mu}{\lambda+2\mu}h+\Lambda\right)|\xi|+(\lambda+\mu)\left(2(1+\Lambda|\xi|)+\frac{2(\lambda+3\mu)}{\lambda+2\mu}t|\xi|\right)t|\xi|+\frac{(\lambda+\mu)^2}{\lambda+2\mu}\left(2th(1+2|\xi|t)+\Lambda\left(2t(t+h)|\xi|+h\right)\right)\xi^2\right]e^{-|\xi|h}\\ +\frac{\tau^s}{2\mu}|\xi|\left\{(\lambda+3\mu)\left[\left(\frac{\lambda+2\mu}{\lambda+\mu}-h|\xi|-\frac{\lambda+3\mu}{\lambda+2\mu}\Lambda|\xi|+\frac{(\lambda+\mu)^2}{(\lambda+2\mu)^2}\Lambda h\xi^2\right)e^{-|\xi|(2t-h)}-\left(\frac{\lambda+2\mu}{\lambda+\mu}-\frac{\lambda+3\mu}{\lambda+2\mu}\Lambda|\xi|\right)\left(1+\frac{\lambda+\mu}{\lambda+2\mu}h|\xi|\right)e^{-|\xi|(2t+h)}\right]\right.\\ +(\lambda+\mu)\left[\left(2t(t-h)|\xi|-h\right)|\xi|+\frac{\lambda+2\mu}{\lambda+\mu}\left(\frac{\lambda+3\mu}{\lambda+\mu}+2t|\xi|\right)+\frac{\lambda+3\mu}{\lambda+2\mu}\left(\frac{\lambda+3\mu}{\lambda+\mu}+2t|\xi|+\frac{\lambda+\mu}{\lambda+2\mu}\left(2t(t-h)|\xi|-h\right)|\xi|\right)\Lambda|\xi|\right]e^{|\xi|h}\\ \left.-(\lambda+\mu)\left[\left(2t(t+h)|\xi|+h\right)|\xi|+\frac{\lambda+2\mu}{\lambda+\mu}\left(\frac{\lambda+3\mu}{\lambda+\mu}+2t|\xi|\right)+\frac{\lambda+3\mu}{\lambda+2\mu}\left(\frac{\lambda+3\mu}{\lambda+\mu}+2t|\xi|+\frac{\lambda+3\mu}{\lambda+2\mu}h|\xi|+\frac{2(\lambda+\mu)}{\lambda+2\mu}t^2\xi^2\right)\Lambda|\xi|+\frac{2(\lambda+\mu)}{(\lambda+2\mu)^2}(1+2t|\xi|)\Lambda th|\xi|^3\right]e^{-|\xi|h}\right\}\end{array}\right\}\frac{\overline{p}(\xi)}{4\xi^2} \tag{A.7}$$

$$H_p=-\left\{\begin{array}{l}(\lambda+\mu)(\lambda+3\mu)\left[(1-\Lambda|\xi|)e^{-|\xi|(2t+h)}+\left(\frac{\lambda+3\mu}{\lambda+\mu}-(\Lambda+2h)|\xi|\right)e^{-|\xi|(2t-h)}\right]\\ +(\lambda+\mu)(1+\Lambda|\xi|)\left[\lambda+3\mu-2(\lambda+\mu)(t-h)|\xi|\right]e^{|\xi|h}+(\lambda+\mu)^2\left[1+\frac{\lambda+3\mu}{\lambda+\mu}(\Lambda+2t)|\xi|+\left(2\Lambda(t+h)+4th\right)\xi^2\right]e^{-|\xi|h}\\ -\frac{\tau^s}{2\mu}|\xi|\left\{(\lambda+3\mu)\left[\left(\lambda+2\mu-\frac{(\lambda+\mu)(\lambda+3\mu)}{\lambda+2\mu}\Lambda|\xi|\right)e^{-|\xi|(2t+h)}-\left(\lambda+2\mu-\frac{(\lambda+\mu)^2}{\lambda+2\mu}\left(\frac{\lambda+3\mu}{\lambda+\mu}-2h|\xi|\right)\Lambda|\xi|\right)e^{-|\xi|(2t-h)}\right]\right.\\ -(\lambda+\mu)\left[(\lambda+2\mu)\left(\frac{\lambda+3\mu}{\lambda+\mu}+2(t-h)|\xi|\right)+\frac{\lambda+3\mu}{\lambda+2\mu}\left(\lambda+3\mu+2(\lambda+\mu)(t-h)|\xi|\right)\Lambda|\xi|\right]e^{|\xi|h}\\ \left.+(\lambda+\mu)\left[(\lambda+2\mu)\left(\frac{\lambda+3\mu}{\lambda+\mu}+2(t+h)|\xi|\right)+\frac{\lambda+3\mu}{\lambda+2\mu}\left(\lambda+3\mu+2(\lambda+\mu)t|\xi|\right)\Lambda|\xi|-\frac{2(\lambda+\mu)^2}{\lambda+2\mu}\Lambda th|\xi|^3\right]e^{-|\xi|h}\right\}\end{array}\right\}\frac{\overline{p}(\xi)}{4(\lambda+2\mu)|\xi|} \tag{A.8}$$

$$A_q=\left\{\begin{array}{l}(\lambda+3\mu)\left[\left(\mu-(\lambda+\mu)\Lambda h\xi^2\right)\cosh\left(\xi(2t-h)\right)+\left(\mu\Lambda-(\lambda+\mu)h\right)\xi\sinh\left(\xi(2t-h)\right)\right]\\ -(\lambda+\mu)\left[\left(\frac{\mu(\lambda+3\mu)}{\lambda+\mu}-\mu\Lambda t\xi^2+(\lambda+\mu)\left(t(t-h)-h\Lambda\right)\xi^2\right)\cosh(\xi h)-\left(\mu t-\frac{\mu(\lambda+3\mu)}{\lambda+\mu}\Lambda-(\lambda+\mu)\left(\Lambda t(t-h)\xi^2-h\right)\right)\xi\sinh(\xi h)\right]\\ +\frac{\tau^s}{2}|\xi|\left\{(\lambda+3\mu)\left[\left(-\frac{\lambda+2\mu}{\lambda+\mu}+\frac{\lambda+3\mu}{\lambda+2\mu}\Lambda|\xi|\right)\cosh\left(\xi(2t-h)\right)+\frac{\lambda+2\mu}{\mu}h\xi\sinh\left(\xi(2t-h)\right)+\frac{(\lambda+\mu)^2}{2\mu(\lambda+2\mu)}\left(e^{|\xi|(2t-h)}+\frac{\lambda+3\mu}{\lambda+\mu}e^{-|\xi|(2t-h)}\right)\Lambda h\xi^2\right]\right.\\ \left.+(\lambda+3\mu)\left[\frac{\lambda+2\mu}{\lambda+\mu}-\frac{\lambda+3\mu}{\lambda+2\mu}\Lambda|\xi|+\frac{2(\lambda+\mu)(\lambda+2\mu)}{\mu(\lambda+3\mu)}t(t-h)\xi^2\right]\cosh(\xi h)-(\lambda+2\mu)\left[2t+\frac{\lambda+\mu}{\mu}h-\frac{2(\lambda+\mu)(\lambda+3\mu)}{(\lambda+2\mu)^2}\Lambda t|\xi|\right]\xi\sin(\xi h)\right.\\ \left.+(\lambda+\mu)\left[\frac{(\lambda+\mu)^2}{\mu(\lambda+2\mu)}t(t-h)|\xi|-\frac{(\lambda+3\mu)^2}{2\mu(\lambda+2\mu)}h\right]\Lambda\xi^2e^{|\xi|h}-\frac{(\lambda+\mu)^2(\lambda+3\mu)}{2\mu(\lambda+2\mu)}\left(t(t-h)|\xi|+h\right)\Lambda\xi^2e^{-|\xi|h}\right\}\end{array}\right\}\frac{\overline{q}(\xi)}{2(\lambda+2\mu)|\xi|\xi}\qquad(A.9)$$

$$B_q=\left\{\begin{array}{l}(\lambda+\mu)(\lambda+3\mu)\left[-2\Lambda\xi\sinh\left(\xi(2t-h)\right)+\left(\frac{\lambda+3\mu}{\lambda+\mu}-2h|\xi|\right)e^{|\xi|(2t-h)}-e^{-|\xi|(2t-h)}-\frac{4(\lambda+\mu)}{\lambda+3\mu}\Lambda(t-h)\xi^2\cosh(\xi h)\right.\\ \left.+2\Lambda\xi\sinh(\xi h)-\left(\frac{\lambda+3\mu}{\lambda+\mu}-2t|\xi|+\frac{4(\lambda+\mu)}{\lambda+3\mu}t(t-h)\xi^2\right)e^{|\xi|h}+\left(1+\frac{2(\lambda+\mu)}{\lambda+3\mu}(t-h)|\xi|\right)e^{-|\xi|h}\right]\\ +\frac{\tau^s}{\mu}|\xi|\left\{(\lambda+3\mu)\left[\left(\lambda+2\mu-\frac{(\lambda+\mu)(\lambda+3\mu)}{\lambda+2\mu}\Lambda|\xi|\right)\left(\cosh\left(\xi(2t-h)\right)-\cosh(\xi h)\right)+\frac{(\lambda+\mu)^2}{\lambda+2\mu}\Lambda h\xi^2e^{|\xi|(2t-h)}\right]\right.\\ \left.+2(\lambda+\mu)(\lambda+2\mu)(t-h)\xi\sinh(\xi h)-\frac{(\lambda+\mu)^2(\lambda+3\mu)}{(\lambda+2\mu)}\left[\left(1-\frac{2(\lambda+\mu)}{\lambda+3\mu}(t-h)|\xi|\right)te^{|\xi|h}+(t-h)e^{-|\xi|h}\right]\Lambda\xi^2\right\}\end{array}\right\}\frac{\overline{q}(\xi)}{4(\lambda+2\mu)\xi}\qquad(A.10)$$

$$C_q=-\left\{\begin{array}{l}(\lambda+3\mu)\left[\left(\mu-(\lambda+\mu)\Lambda h\xi^2\right)\cosh\left(\xi(2t-h)\right)+\left(\mu\Lambda-(\lambda+\mu)h\right)\xi\sinh\left(\xi(2t-h)\right)\right]\\ -(\lambda+\mu)\left[\left(\frac{\mu(\lambda+3\mu)}{\lambda+3\mu}-\mu\Lambda t\xi^2-(\lambda+\mu)\left(t(t-h)+h\Lambda\right)\xi^2\right)\cosh(\xi h)-\left(\mu t-\frac{\mu(\lambda+3\mu)}{\lambda+\mu}\Lambda-(\lambda+\mu)\left(\Lambda t(t-h)\xi^2-h\right)\right)\xi\sinh(\xi h)\right]\\ +\frac{\tau^s}{2}|\xi|\left\{(\lambda+3\mu)\left[\left(\frac{\lambda+2\mu}{\lambda+\mu}+\frac{\lambda+3\mu}{\lambda+2\mu}\Lambda|\xi|\right)\cosh\left(\xi(2t-h)\right)-\frac{\lambda+2\mu}{\mu}h\xi\sinh\left(\xi(2t-h)\right)-\frac{(\lambda+\mu)^2}{2\mu(\lambda+2\mu)}\left(\frac{\lambda+3\mu}{\lambda+\mu}e^{|\xi|(2t-h)}-e^{-|\xi|(2t-h)}\right)\Lambda h\xi^2\right]\right.\\ \left.+(\lambda+3\mu)\left[\frac{\lambda+2\mu}{\lambda+\mu}-\frac{\lambda+3\mu}{\lambda+2\mu}\Lambda|\xi|-\frac{(\lambda+\mu)(\lambda+2\mu)}{\mu(\lambda+3\mu)}h|\xi|\right]\cosh(\xi h)-(\lambda+2\mu)\left[2t+\frac{2(\lambda+\mu)}{\mu}t(t-h)|\xi|-\frac{2(\lambda+\mu)(\lambda+3\mu)}{(\lambda+2\mu)^2}\Lambda t|\xi|\right]\xi\sin(\xi h)\right.\\ \left.+(\lambda+\mu)\left[\left(\frac{(\lambda+\mu)(\lambda+3\mu)}{\mu(\lambda+2\mu)}t(t-h)|\xi|-\frac{(\lambda+3\mu)^2}{2\mu(\lambda+2\mu)}h\right)e^{|\xi|h}-\left(\frac{(\lambda+3\mu)^2}{2\mu(\lambda+2\mu)}h-\frac{(\lambda+\mu)^2}{\mu(\lambda+2\mu)}t(t-h)|\xi|\right)e^{-|\xi|h}\right]\Lambda\xi^2\right\}\end{array}\right\}\frac{\overline{q}(\xi)}{2(\lambda+2\mu)|\xi|\xi}\qquad(A.11)$$

$$D_q=\left\{\begin{array}{l}(\lambda+\mu)(\lambda+3\mu)\left[-2\Lambda\xi\sinh\left(\xi(2t-h)\right)-e^{|\xi|(2t-h)}+\left(\frac{\lambda+3\mu}{\lambda+\mu}+2h|\xi|\right)e^{-|\xi|(2t-h)}-\frac{4(\lambda+\mu)}{\lambda+3\mu}\Lambda(t-h)\xi^2\cosh(\xi h)\right.\\ \left.+2\Lambda\xi\sinh(\xi h)+\left(1-\frac{2(\lambda+\mu)}{\lambda+3\mu}(t-h)|\xi|\right)e^{|\xi|h}-\left(\frac{\lambda+3\mu}{\lambda+\mu}+2t|\xi|+\frac{4(\lambda+\mu)}{\lambda+3\mu}t(t-h)\xi^2\right)e^{-|\xi|h}\right]\\ -\frac{\tau^s}{\mu}|\xi|\left\{(\lambda+3\mu)\left[\left(\lambda+2\mu+\frac{(\lambda+\mu)(\lambda+3\mu)}{\lambda+2\mu}\Lambda|\xi|\right)\left(\cosh\left(\xi(2t-h)\right)-\cosh(\xi h)\right)+\frac{(\lambda+\mu)^2}{\lambda+2\mu}\Lambda h\xi^2e^{-|\xi|(2t-h)}\right]\right.\\ \left.+(\lambda+\mu)\left[2(\lambda+2\mu)(t-h)+\frac{2(\lambda+\mu)(\lambda+3\mu)}{\lambda+2\mu}\Lambda t|\xi|\right]\xi\sinh(\xi h)-\frac{(\lambda+\mu)^3}{\lambda+2\mu}\left(\frac{\lambda+3\mu}{\lambda+\mu}he^{|\xi|h}+2t(t-h)|\xi|e^{-|\xi|h}\right)\Lambda\xi^2\right\}\end{array}\right\}\frac{\overline{q}(\xi)}{4(\lambda+2\mu)\xi}\qquad(A.12)$$

$$E_q=-\left\{\begin{array}{l}(\lambda+3\mu)(1+\Lambda|\xi|)\left[\left(\mu+(\lambda+\mu)h|\xi|\right)e^{|\xi|(2t+h)}-\left(\mu-(\lambda+\mu)h|\xi|\right)e^{|\xi|(2t-h)}\right]+\left[\mu(\lambda+3\mu)+(\lambda+\mu)\left((\lambda+\mu)(2t(t-h)|\xi|-h)-2\mu t\right)|\xi|\right](1-\Lambda|\xi|)e^{|\xi|h}\\ +(\lambda+\mu)\left[\frac{\mu(3\lambda^2+12\lambda\mu+13\mu^2)}{(\lambda+\mu)^2}+\frac{\lambda+3\mu}{\lambda+\mu}\left(\mu\Lambda+(\lambda+3\mu)h\right)|\xi|+2\mu(1-\Lambda|\xi|)t|\xi|+2(\lambda+3\mu)t^2\xi^2+(\lambda+\mu)\left(\Lambda\left(2t(t+h)|\xi|+h\right)+2th(1+2t|\xi|)\right)\xi^2\right]e^{-|\xi|h}\\ +\frac{\tau^s}{2}|\xi|\left\{(\lambda+3\mu)\left[\left(\frac{\lambda+2\mu}{\lambda+\mu}+\frac{(\lambda+3\mu)}{\lambda+2\mu}\Lambda|\xi|\right)\left(1+\frac{\lambda+\mu}{\mu}h|\xi|\right)e^{|\xi|(2t+h)}+\left(\frac{\lambda+2\mu}{\lambda+\mu}-\frac{\lambda+2\mu}{\mu}h|\xi|-\frac{\lambda+3\mu}{\lambda+2\mu}\Lambda|\xi|-\frac{(\lambda+\mu)^2}{\mu(\lambda+2\mu)}\Lambda h\xi^2\right)e^{|\xi|(2t-h)}\right]\right.\\ -(\lambda+\mu)(\lambda+2\mu)\left\{\left[\frac{\lambda+3\mu}{(\lambda+\mu)^2}+\frac{2}{\lambda+\mu}t|\xi|+\frac{1}{\mu}\left(2t(t-h)|\xi|+h\right)|\xi|-\frac{\lambda+3\mu}{(\lambda+2\mu)^2}\left(\frac{\lambda+3\mu}{\lambda+\mu}+2t|\xi|+\frac{\lambda+\mu}{\mu}\left(2t(t-h)|\xi|+h\right)|\xi|\right)\Lambda|\xi|\right]e^{-|\xi|h}\right.\\ \left.\left.+\left[\frac{\lambda+3\mu}{(\lambda+\mu)^2}+\frac{2}{\lambda+\mu}t|\xi|+\frac{1}{\mu}\left(2t(t+h)|\xi|-h\right)|\xi|+\frac{\lambda+3\mu}{(\lambda+2\mu)^2}\left(\frac{\lambda+3\mu}{\lambda+\mu}+2t|\xi|+\frac{\lambda+3\mu}{\mu}h|\xi|+\frac{2(\lambda+\mu)}{\mu}t^2\xi^2-\frac{2(\lambda+\mu)^2}{\mu(\lambda+3\mu)}\left(1-2t|\xi|\right)th\xi^2\right)\Lambda|\xi|\right]e^{|\xi|h}\right\}\right\}\end{array}\right\}\frac{\overline{q}(\xi)}{4(\lambda+2\mu)|\xi|\xi}\qquad(A.13)$$

$$F_{\bar{q}}=\left\{\begin{array}{l}(\lambda+\mu)(\lambda+3\mu)\left[\left(1+\Lambda|\xi|\right)e^{|\xi|(2t+h)}+\left(\frac{\lambda+3\mu}{\lambda+\mu}-(\Lambda+2h)|\xi|\right)e^{|\xi|(2t-h)}\right.\\ \left.+\left(\frac{\lambda+\mu}{\lambda+3\mu}\left(1+4th\xi^2+2(t+h)\Lambda\xi^2\right)+(\Lambda+2t)|\xi|\right)e^{|\xi|h}+\left(1-\Lambda|\xi|\right)\left(1+\frac{2(\lambda+\mu)}{\lambda+3\mu}(t-h)|\xi|\right)e^{-|\xi|h}\right]\\ +\frac{\tau^s}{2\mu}|\xi|\left\{(\lambda+3\mu)\left[\left(\lambda+2\mu+\frac{(\lambda+\mu)(\lambda+3\mu)}{\lambda+2\mu}\Lambda|\xi|\right)e^{|\xi|(2t+h)}+\left(\lambda+2\mu-\frac{(\lambda+\mu)(\lambda+3\mu)}{\lambda+2\mu}\Lambda|\xi|+\frac{2(\lambda+\mu)^2}{\lambda+2\mu}\Lambda h\xi^2\right)e^{|\xi|(2t-h)}\right]\right.\\ -(\lambda+\mu)\left[\frac{(\lambda+2\mu)(\lambda+3\mu)}{\lambda+\mu}+2(\lambda+2\mu)(t+h)|\xi|+\frac{(\lambda+3\mu)^2}{\lambda+2\mu}\left(1+\frac{2(\lambda+\mu)}{\lambda+3\mu}t|\xi|+\frac{2(\lambda+\mu)^2}{(\lambda+3\mu)^2}th\xi^2\right)\Lambda|\xi|\right]e^{|\xi|h}\\ \left.-(\lambda+\mu)\left[\frac{(\lambda+2\mu)(\lambda+3\mu)}{\lambda+\mu}+2(\lambda+2\mu)(t-h)|\xi|-\frac{(\lambda+3\mu)^2}{\lambda+2\mu}\left(1+\frac{2(\lambda+\mu)}{\lambda+3\mu}(t-h)|\xi|\right)\Lambda|\xi|\right]e^{-|\xi|h}\right\}\end{array}\right\}\frac{\bar{q}(\xi)}{4(\lambda+2\mu)\xi} \tag{A.14}$$

$$G_{\bar{q}}=\left\{\begin{array}{l}(\lambda+3\mu)(1-\Lambda|\xi|)\left[\left(\mu-(\lambda+\mu)h|\xi|\right)e^{-|\xi|(2t+h)}-\left(\mu+(\lambda+\mu)h|\xi|\right)e^{-|\xi|(2t-h)}\right]+\left[\mu(\lambda+3\mu)+(\lambda+\mu)\left((\lambda+\mu)(2t(t-h)|\xi|-h)-2\mu t\right)|\xi|\right](1+\Lambda|\xi|)e^{|\xi|h}\\ +(\lambda+\mu)\left[\frac{\mu\left(3\lambda^2+12\lambda\mu+13\mu^2\right)}{(\lambda+\mu)^2}-\frac{\lambda+3\mu}{\lambda+\mu}\left(\mu\Lambda+(\lambda+3\mu)h\right)|\xi|+2\mu\left(1+\Lambda|\xi|\right)t|\xi|+2(\lambda+3\mu)t^2\xi^2-(\lambda+\mu)\left(\Lambda\left(2t(t+h)|\xi|+h\right)+2th\left(1+2t|\xi|\right)\right)\xi^2\right]e^{-|\xi|h}\\ -\frac{\tau^s}{2}|\xi|\left\{(\lambda+3\mu)\left[\left(\frac{\lambda+2\mu}{\lambda+\mu}-\frac{(\lambda+3\mu)}{\lambda+2\mu}\Lambda|\xi|\right)\left(1-\frac{\lambda+\mu}{\mu}h|\xi|\right)e^{-|\xi|(2t+h)}+\left(\frac{\lambda+2\mu}{\lambda+\mu}+\frac{\lambda+2\mu}{\mu}h|\xi|+\frac{\lambda+3\mu}{\lambda+2\mu}\Lambda|\xi|-\frac{(\lambda+\mu)^2}{\mu(\lambda+2\mu)}\Lambda h\xi^2\right)e^{-|\xi|(2t-h)}\right]\right.\\ -(\lambda+\mu)(\lambda+2\mu)\left\{\left[\frac{\lambda+3\mu}{(\lambda+\mu)^2}-\frac{2}{\lambda+\mu}t|\xi|+\frac{1}{\mu}\left(2t(t-h)|\xi|-h\right)|\xi|+\frac{\lambda+3\mu}{(\lambda+2\mu)^2}\left(\frac{\lambda+3\mu}{\lambda+\mu}-2t|\xi|+\frac{\lambda+\mu}{\mu}\left(2t(t-h)|\xi|-h\right)|\xi|\right)\Lambda|\xi|\right]e^{|\xi|h}\right.\\ \left.\left.+\left[\frac{\lambda+3\mu}{(\lambda+\mu)^2}-\frac{2}{\lambda+\mu}t|\xi|+\frac{1}{\mu}\left(2t(t+h)|\xi|+h\right)|\xi|-\frac{\lambda+3\mu}{(\lambda+2\mu)^2}\left(\frac{\lambda+3\mu}{\lambda+\mu}-2t|\xi|-\frac{\lambda+3\mu}{\mu}h|\xi|+\frac{2(\lambda+\mu)}{\mu}t^2\xi^2-\frac{2(\lambda+\mu)^2}{\mu(\lambda+3\mu)}(1+2t|\xi|)th\xi^2\right)\Lambda|\xi|\right]e^{-|\xi|h}\right\}\right\}\end{array}\right\}\frac{\bar{q}(\xi)}{4(\lambda+2\mu)|\xi|\xi} \tag{A.15}$$

$$H_{\bar{q}}=\left\{\begin{array}{l}(\lambda+\mu)(\lambda+3\mu)\left[\left(1-\Lambda|\xi|\right)e^{-|\xi|(2t+h)}+\left(\frac{\lambda+3\mu}{\lambda+\mu}+(\Lambda+2h)|\xi|\right)e^{-|\xi|(2t-h)}\right.\\ \left.+\left(1+\Lambda|\xi|\right)\left(1-\frac{2(\lambda+\mu)}{\lambda+3\mu}(t-h)|\xi|\right)e^{|\xi|h}+\left(\frac{\lambda+\mu}{\lambda+3\mu}\left(1+4th\xi^2+2(t+h)\Lambda\xi^2\right)-(\Lambda+2t)|\xi|\right)e^{-|\xi|h}\right]\\ -\frac{\tau^s}{2\mu}|\xi|\left\{(\lambda+3\mu)\left[\left(\lambda+2\mu-\frac{(\lambda+\mu)(\lambda+3\mu)}{\lambda+2\mu}\Lambda|\xi|\right)e^{-|\xi|(2t+h)}+\left(\lambda+2\mu+\frac{(\lambda+\mu)(\lambda+3\mu)}{\lambda+2\mu}\Lambda|\xi|+\frac{2(\lambda+\mu)^2}{\lambda+2\mu}\Lambda h\xi^2\right)e^{-|\xi|(2t-h)}\right]\right.\\ -(\lambda+\mu)\left[\frac{(\lambda+2\mu)(\lambda+3\mu)}{\lambda+\mu}-2(\lambda+2\mu)(t-h)|\xi|+\frac{(\lambda+3\mu)^2}{\lambda+2\mu}\left(1-\frac{2(\lambda+\mu)}{\lambda+3\mu}(t-h)|\xi|\right)\Lambda|\xi|\right]e^{|\xi|h}\\ \left.-(\lambda+\mu)\left[\frac{(\lambda+2\mu)(\lambda+3\mu)}{\lambda+\mu}-2(\lambda+2\mu)(t+h)|\xi|-\frac{(\lambda+3\mu)^2}{\lambda+2\mu}\left(1-\frac{2(\lambda+\mu)}{\lambda+3\mu}t|\xi|+\frac{2(\lambda+\mu)^2}{(\lambda+3\mu)^2}th\xi^2\right)\Lambda|\xi|\right]e^{-|\xi|h}\right\}\end{array}\right\}\frac{\bar{q}(\xi)}{4(\lambda+2\mu)\xi} \tag{A.16}$$

$$\begin{array}{l}I=(\lambda+3\mu)\left[\cosh(2t\xi)+\Lambda\xi\sinh(2t\xi)\right]+2t\xi^2(\lambda+\mu)(\Lambda+t)+\frac{\lambda^2+4\lambda\mu+5\mu^2}{\lambda+\mu}\\ +\tau^s\left\{(\lambda+3\mu)\left[\frac{(\lambda+3\mu)}{2\mu(\lambda+2\mu)}\Lambda\xi^2\cosh(2t\xi)+\frac{(\lambda+2\mu)}{2\mu(\lambda+\mu)}\xi\sinh(2t\xi)-\frac{(\lambda+3\mu)}{2\mu(\lambda+2\mu)}\Lambda\xi^2\right]-\frac{(\lambda+2\mu)}{\mu}t\xi^2-\frac{(\lambda+\mu)^2}{\mu(\lambda+2\mu)}\Lambda t^2\xi^4\right\}\end{array} \tag{A.17}$$

FEM-SGBEM coupling for modeling of mode-I planar cracks in three-dimensional elastic media with residual surface tension effects

T. B. Nguyen[1], J. Rungamornrat[1,*], T. Senjuntichai[1] and A. C. Wijeyewickrema[2]

[1]Department of Civil Engineering, Faculty of Engineering, Chulalongkorn University, Bangkok 10330, Thailand

[2]Department of Civil and Environmental Engineering, Tokyo Institute of Technology, Tokyo 152-8552, Japan

Abstract

A computationally efficient numerical technique capable of modeling mode-I planar cracks in three-dimensional linear elastic media by taking the influence of the residual surface tension into account, is presented in this paper. The elastic medium (i.e., the bulk material) is modeled by the classical theory of linear elasticity, whereas the crack surface is treated as a zero-thickness layer perfectly bonded to the bulk material with its behavior governed by the special case of Gurtin-Murdoch surface elasticity model. Governing equations of the bulk material are formulated in terms of weakly singular, weak-form boundary integral equations, whereas those of the surface are cast in a weak form using a weighted residual technique. The solution of the final coupled system of governing equations is subsequently accomplished by using a numerical procedure based primarily on a coupling between standard finite element technique and a weakly singular, symmetric Galerkin boundary element method. Extensive numerical simulations are conducted and the results are compared with available benchmark solutions to verify the formulation and numerical implementation. Applications of the technique to the analysis of nano-crack problems are presented for some selected cases, to study nano-scale influence and size-dependency behavior.

Keywords: Crack opening displacement, Gurtin-Murdoch model, Nano-cracks, Residual surface tension, SGBEM, Surface elasticity

1. Introduction

Due to the rapid growth of the application of nano-sized devices and nano-structured materials in various fields, the physical modeling and corresponding comprehensive analysis to gain an insight into their complex behavior become important aspects in the optimal design of nano-scale products. Failure/damage analysis and assessment is one of the essential steps that must be properly considered to ensure their safety and integrity in the design procedure. To aid such crucial tasks, a classical approach based on the stress analysis of a body containing pre-existing defects or cracks is usually considered. While conventional linear elastic fracture mechanics has been well established

* Corresponding author. Tel.: +66-2-218-6460-2

E-mail address: Jaroon.r@chula.ac.th (J. Rungamornrat)

and employed in the modeling of cracks in linear elastic media, an enhancement of the classical model to incorporate the nano-scale influence is still required. Studies using atomistic calculations have pointed out that atoms near the free surface of solids behave differently from their bulk. In that sense, the whole body is not completely homogeneous, but when its size is in the range of micrometers or larger, the surface free energy effect can be neglected due to its insignificant influence on overall material properties. Unlike macro-structures, in the case of nano-sized objects (e.g., thin films, quantum dots, nano-wires, nano-tubes and nano-composites), the surface to volume ratio is much higher and, as a direct consequence, the surface free energy effect often plays a crucial role in the mechanical behavior [1]. Therefore, the classical theory of continuum-based mechanics commonly used in the modeling of macroscopic bodies cannot be directly applied to treat the problem of nano-sized cracks.

To be capable of capturing the surface free energy effect, a model that properly takes into account the surface free energy must be utilized. The most widely used continuum-based models which incorporate surface free energy effects are those using Gurtin-Murdoch surface elasticity theory. Gurtin and Murdoch [2, 3] proposed a mathematical framework to study the mechanical behavior of material surfaces through a continuum-based model which includes surface stresses. The elastic surface is assumed to be very thin and modeled as a mathematical layer of zero thickness that is perfectly bonded to the bulk material. In addition, such an idealized surface has different elastic moduli from those of the bulk material.

The Gurtin-Murdoch model has been widely used to study various size-dependent, nano-scale problems. For instance, He et al. [4], Dingreville et al. [5] and Huang [6] employed the Gurtin-Murdoch surface elasticity model to clearly elucidate the size-dependent elastic properties of nano-structured elements such as wires and films, while Tian and Rajapakse [7, 8, 9] applied such model to demonstrate the influence of surface stresses on elastic fields of nano-inhomogeneity problems. More recently, Pinyochotiwong et al. [10] investigated the effects of surface energy in the analysis of an axisymmetric rigid frictionless indentor acting on an isotropic, linearly elastic half-space by using the complete version of the Gurtin-Murdoch model.

The continuum-based surface/interface model of Gurtin and Murdoch has also been employed in the modeling of nano-sized cracks. Based upon an investigation of an elliptical void, Wu [11] argued that the presence of the surface stress has the capability of containing the severity of deformations of a blunt crack. Wang et al. [12] studied the surface stress effect on near-tip stresses for both mode-I and mode-III blunt cracks and found that when the curvature radius of the crack front decreases to nanometers, surface energy significantly affects the stress intensities near

the crack tip. Fu et al. [13, 14] incorporated the surface elasticity model into the finite element method (via ANSYS® and ABAQUS®) to study the influence of surface stresses on the mode-I and mode-II crack-tip fields and concluded that when the curvature radius of the blunt crack root decreases to micro-/nano-meters, surface elasticity exhibits significant influence on the stresses near the crack tip. Fang et al. [15] analyzed the influence of surface effects on dislocation emission from an elliptically blunt crack under mode-I and mode-II loading conditions and showed that the impact of surface stresses on the critical stress intensity factors for dislocation emission becomes remarkable when the size of the blunt crack is very small, typically of a nanometer scale. Kim et al. [16, 17, 18] examined mode-I, mode-II and mode-III crack problems including surface stress effects which assumed that the stresses at the sharp crack-tip are finite. Recently, Nan and Wang [19] considered the effect of the residual surface tension on the crack surface, to investigate the mode-I crack problem and demonstrated that the surface effect on the crack deformation and crack-tip field are prominent at nanoscale. Moreover, the results are influenced by the residual surface tension not only on the surface near the crack-tip region but also on the entire crack-face. Intarit et al. [20, 21] analytically investigated a nano-sized, penny-shaped crack in three-dimensional, linear elastic media under mode-I loading conditions.

On the basis of an extensive literature survey, it can be said that work related to the modeling of defects/cracks at nano-scale level has been very limited. Most of the studies are restricted to situations where cracks can be treated either within the context of two-dimensional boundary value problems [11-19] or within the context of relatively simple three-dimensional problems [20, 21]. However, bodies or components containing existing defects/flaws involved in practical applications are, in general, relatively complex in terms of geometries, loading conditions, and influences to be treated (e.g., surface free energy). The existing mathematical models are therefore of limited scope and insufficient for the prediction of responses in practical cases. This, as a result, necessitates the development of fully three-dimensional mathematical models, along with efficient and powerful numerical procedures to construct their solutions.

Numerical techniques based on boundary integral equations have been well-established and proven powerful for both two-dimensional and three-dimensional fracture analysis (e.g., [22-27]). The techniques possess attractive characteristics, such as governing equations with spatially reduced dimensions and simplicity of treating remote boundaries and infinite bodies, rendering them computationally efficient and convenient for modeling crack problems. The weakly singular, symmetric Galerkin boundary element method (SGBEM), which is a principal numerical technique proposed to model the cracks in the present study, is a particular boundary integral equation method

that has been continuously developed and widely adopted by various investigators in the past four decades. This special numerical technique has been widely and successfully employed to solve both linear elasticity and linear elastic fracture problems [28-38], since it has several important features. For instance, the governing integral equations contain only weakly singular kernels (of $\mathcal{O}(1/r)$); the technique is applicable for modeling cracks with arbitrary configurations and under general loading conditions and for treating an infinite body efficiently; and the formulation is established in a symmetric weak-form such that it gives rise to a system of linear equations with a symmetric coefficient matrix. The first feature renders that all involved integrals exist in an ordinary sense and their validity requires only the continuity of the boundary data; i.e., in the numerical implementation, it is possible to employ standard C^0 elements in the approximation of all primary unknowns and to apply existing quadrature schemes to numerically evaluate all involved integrals (e.g., [31, 32, 37, 38]). In addition, the last feature also allows the SGBEM to be conveniently coupled with the standard finite element procedure to enhance its computational efficiency and capability (e.g., [39, 40]). Extensive review of the weakly singular SGBEM can be found in Bonnet et al. [41], in Rungamornrat and Mear [37] and Rungamornrat and Senjuntichai [38] for its application to three-dimensional fracture analysis, in Rungamornrat and Mear [40] for its coupling with the standard FEM. It should be remarked that, on the basis of an extensive literature survey, applications of the SGBEM-FEM technique to the analysis of nano-size cracks has not been well recognized. Efficiency and capability of such technique, when applied to this particular class of problems, still requires full investigations.

In this paper, a computationally efficient numerical technique capable of modeling planar cracks in three-dimensional isotropic, linear elastic media including the influence of residual surface tension is presented. The residual surface tension effects are modeled using the well-known Gurtin-Murdoch theory of surface elasticity. A numerical procedure based primarily on the coupling of a standard finite element method (FEM) and a weakly singular, symmetric Galerkin boundary element method is employed. The former technique is mainly utilized to efficiently handle the governing equation of the surface. While the proposed technique follows, in principle, the standard coupling procedure, novelty of the current work should be reflected through its recent applications to the modeling of cracks with nano-scale influence. Extensive numerical simulations are conducted and the results are compared with available benchmark solutions to verify both the formulation and the numerical implementation. Applications of the technique to the analysis of mode-I, nano-sized, crack problems are presented for some selected cases, to study nano-scale influence and size-dependency behavior.

2. Formulation

This section begins with the clear description and essential assumptions of the boundary value problem that is the focus of the present study. All basic field equations and the development of key governing equations for both the bulk material and the crack surface are then briefly presented. Finally, the coupled system of weak-form equations governing the primary unknowns on the crack surface is derived.

2.1. Problem description

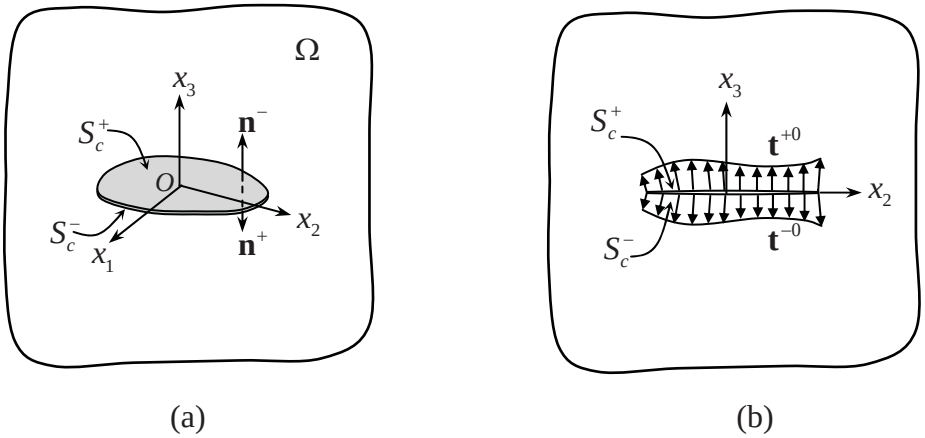

(a) (b)

Fig. 1. (a) Schematic of three-dimensional infinite elastic medium containing an isolated crack; (b) prescribed traction on crack surfaces.

Consider a three-dimensional, infinite, elastic medium Ω containing an isolated, planar crack as shown schematically in Fig. 1(a). The reference Cartesian coordinate system $\{O; x_1, x_2, x_3\}$ is also shown. The bulk material is made of a homogeneous, isotropic, linearly elastic material with shear modulus μ and Poisson's ratio ν. The crack surfaces which are geometrically identical are represented by S_c^+ and S_c^- with corresponding outward unit normal $\mathbf{n}^+$ and $\mathbf{n}^-$, respectively. The medium is assumed to be free of body forces and remote loading but subjected to prescribed tractions $\mathbf{t}^{+0}$ and $\mathbf{t}^{-0}$ on S_c^+ and S_c^-, respectively (Fig. 1(b)). In addition, infinitesimally thin layers on the crack surfaces (mathematically modeled by zero-thickness layers perfectly bonded to the crack surfaces) possess the constant residual surface tension under unstrained conditions which is denoted by τ^s.

In the formulation of the boundary value problem, the medium is decomposed into three parts: the bulk material, the zero-thickness layer S_c^+ and the zero-thickness layer S_c^- as shown in Fig. 2. The bulk material is simply the whole medium without the two infinitesimally thin layers on

the crack surfaces. Since both layers have zero thickness, the geometry of the bulk material is therefore identical to that of the whole medium (i.e., it can also be completely described by the region Ω and the two crack surfaces S_c^+ and S_c^-).

The key difference between the bulk material and the original medium is that the bulk material is homogeneous and the crack surfaces S_c^+ and S_c^- in the bulk part are subjected to unknown tractions (exerted directly by the two layers) $\mathbf{t}^{+b}$ and $\mathbf{t}^{-b}$, respectively. The layer S_c^+ is treated as a two-sided surface with one side subjected to the prescribed traction $\mathbf{t}^{+0}$ and the other side subjected to the traction $\mathbf{t}^{+s}$ exerted by the bulk material (Fig. 2(b)). Similarly, the layer S_c^- is treated as a two-sided surface with one side subjected to the prescribed traction $\mathbf{t}^{-0}$ and the other side subjected to the traction $\mathbf{t}^{-s}$ exerted by the bulk material (Fig. 2(c)). In what follows, Greek subscripts denote field quantities associated with the surface and take the values 1, 2 while the Latin subscripts take the values 1, 2, 3. We remark that, in the development to follow, it will suffice to make reference to the single crack surface $S_c \equiv S_c^+$.

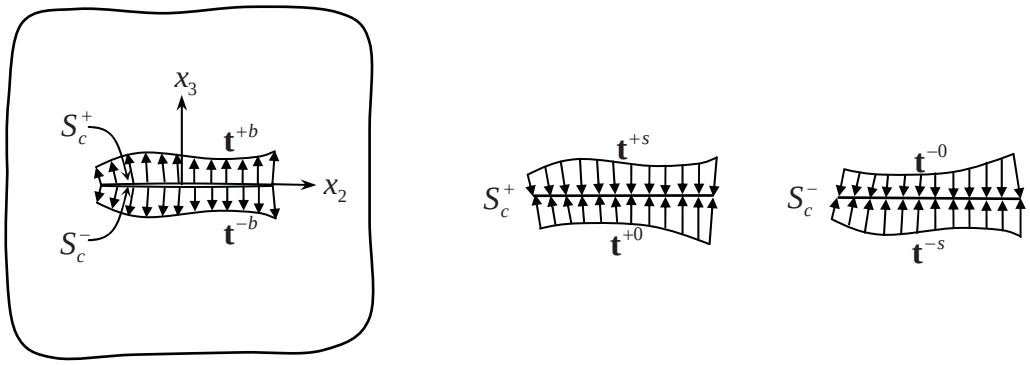

(a) (b) (c)

Fig. 2. Schematics of (a) the bulk material, (b) the zero-thickness layer S_c^+ and (c) the zero-thickness layer S_c^-.

2.2. Governing equations for bulk material

Since the bulk material is made of homogeneous, isotropic, linearly elastic material, its behavior is governed by the classical theory of linear elasticity. From results developed in the work of Rungamornrat and Mear [36] and Rungamornrat and Senjuntichai [38], the displacement and stress components at any interior point $\mathbf{x}$, denoted respectively by $u_p(\mathbf{x})$ and $\sigma_{ij}(\mathbf{x})$, can be expressed in terms of the traction data $\mathbf{t}^{+b}$ and $\mathbf{t}^{-b}$ and the displacement data $\mathbf{u}^{+b}$ and $\mathbf{u}^{-b}$ on the crack surfaces S_c^+ and S_c^- as

$$u_p(\mathbf{x}) = \int_{S_c} U_j^p(\boldsymbol{\xi}-\mathbf{x}) t_j^{b\Sigma}(\boldsymbol{\xi}) dS(\boldsymbol{\xi}) + \int_{S_c} G_{mj}^p(\boldsymbol{\xi}-\mathbf{x}) D_m u_j^{b\Delta}(\boldsymbol{\xi}) dS(\boldsymbol{\xi}) - \int_{S_c} H_{ij}^p(\boldsymbol{\xi}-\mathbf{x}) n_i(\boldsymbol{\xi}) u_j^{b\Delta}(\boldsymbol{\xi}) dS(\boldsymbol{\xi}) \tag{1}$$

$$\sigma_{ij}(\mathbf{x}) = \int_{S_c} \varepsilon_{irt} C_{lk,r}^{tj}(\boldsymbol{\xi}-\mathbf{x}) D_l u_k^{b\Delta}(\boldsymbol{\xi}) dS(\boldsymbol{\xi}) + \int_{S_c} \varepsilon_{irt} G_{tj,r}^p(\boldsymbol{\xi}-\mathbf{x}) t_p^{b\Sigma}(\boldsymbol{\xi}) dS(\boldsymbol{\xi}) - \int_{S_c} H_{ij}^p(\boldsymbol{\xi}-\mathbf{x}) t_p^{b\Sigma}(\boldsymbol{\xi}) dS(\boldsymbol{\xi}) \tag{2}$$

where $D_t(\cdot) = \varepsilon_{tmj} n_m \partial(\cdot)/\partial\xi_j$ is a surface differential operator, $t_j^{b\Sigma} = t_j^{+b} + t_j^{-b}$, $u_j^{b\Delta} = u_j^{+b} - u_j^{-b}$, ε_{irt} is the standard alternating symbol, the kernels $\{U_j^p, G_{mj}^p, C_{mj}^{tk}, H_{ij}^p\}$ for isotropic elastic materials are given by

$$U_j^p(\boldsymbol{\xi}-\mathbf{x}) = \frac{1}{16\pi(1-\nu)\mu r}\left[(3-4\nu)\delta_{pj} + \frac{(\xi_p - x_p)(\xi_j - x_j)}{r^2}\right] \tag{3}$$

$$G_{mj}^p(\boldsymbol{\xi}-\mathbf{x}) = \frac{1}{8\pi(1-\nu)r}\left[(1-2\nu)\varepsilon_{mpj} + \frac{(\xi_p - x_p)(\xi_a - x_a)}{r^2}\varepsilon_{ajm}\right] \tag{4}$$

$$C_{mj}^{tk}(\boldsymbol{\xi}-\mathbf{x}) = \frac{\mu}{4\pi(1-\nu)r}\left[(1-\nu)\delta_{tk}\delta_{mj} + 2\nu\delta_{km}\delta_{tj} - \delta_{kj}\delta_{tm} - \frac{(\xi_k - x_k)(\xi_j - x_j)}{r^2}\delta_{tm}\right] \tag{5}$$

$$H_{ij}^p(\boldsymbol{\xi}-\mathbf{x}) = -\frac{(\xi_i - x_i)\delta_{jp}}{4\pi r^3} \tag{6}$$

with $r = \|\boldsymbol{\xi}-\mathbf{x}\|$ and $\delta_{ij}, \varepsilon_{ijk}$ are standard Kronecker delta and alternating symbols, respectively. The boundary integral relations (1) and (2) allow the displacement and stress at any interior point to be determined once the data $\mathbf{t}^{+b}$, $\mathbf{t}^{-b}$, $\mathbf{u}^{+b}$ and $\mathbf{u}^{-b}$ are known. To establish the integral equations governing the unknown data $\mathbf{t}^{+b}$, $\mathbf{t}^{-b}$, $\mathbf{u}^{+b}$ and $\mathbf{u}^{-b}$, the integral relations (1) and (2) are utilized along with the process of taking limit to any point on the crack surface and the standard procedure using Stokes' theorem in the development of the weak-form equations. The final weak-form, boundary integral equations are given by (see details of the development in Rungamornrat and Mear [36] and Rungamornrat and Senjuntichai [38])

$$\frac{1}{2}\int_{S_c} \tilde{t}_p^{\Sigma}(\mathbf{y}) u_p^{b\Sigma}(\mathbf{y}) dS(\mathbf{y}) = \int_{S_c} \tilde{t}_p^{\Sigma}(\mathbf{y}) \int_{S_c} U_j^p(\boldsymbol{\xi}-\mathbf{y}) t_j^{b\Sigma}(\boldsymbol{\xi}) dS(\boldsymbol{\xi}) dS(\mathbf{y}) + \int_{S_c} \tilde{t}_p^{\Sigma}(\mathbf{y}) \int_{S_c} G_{mj}^p(\boldsymbol{\xi}-\mathbf{y}) D_m u_j^{b\Delta}(\boldsymbol{\xi}) dS(\boldsymbol{\xi}) dS(\mathbf{y}) - \int_{S_c} \tilde{t}_p^{\Sigma}(\mathbf{y}) \int_{S_c} H_{ij}^p(\boldsymbol{\xi}-\mathbf{y}) n_i(\boldsymbol{\xi}) u_j^{b\Delta}(\boldsymbol{\xi}) dS(\boldsymbol{\xi}) dS(\mathbf{y}) \tag{7}$$

$$-\frac{1}{2}\int_{S_c}\tilde{u}_k^{\Lambda}(\mathbf{y})t_k^{b\Delta}(\mathbf{y})dS(\mathbf{y})=\int_{S_c}D_t\tilde{u}_k^{\Lambda}(\mathbf{y})\int_{S_c}C_{mj}^{tk}(\xi-\mathbf{y})D_m u_j^{b\Delta}(\xi)dS(\xi)dS(\mathbf{y})$$
$$+\int_{S_c}D_t\tilde{u}_k^{\Lambda}(\mathbf{y})\int_{S_c}G_{tk}^{j}(\xi-\mathbf{y})t_j^{b\Sigma}(\xi)dS(\xi)dS(\mathbf{y}) \quad (8)$$
$$+\int_{S_c}\tilde{u}_k^{\Lambda}(\mathbf{y})\int_{S_c}H_{lk}^{j}(\xi-\mathbf{y})n_l(\mathbf{y})t_j^{b\Sigma}(\xi)dS(\xi)dS(\mathbf{y})$$

where $u_j^{b\Sigma}=u_j^{+b}+u_j^{-b}$, $t_j^{b\Delta}=t_j^{+b}-t_j^{-b}$, and $\{\tilde{t}_p^{\Sigma},\tilde{u}_k^{\Delta}\}$ are sufficiently smooth test functions. The pair of equations (7) and (8) has been well recognized as the weak-form boundary integral equations for the sum of the displacement $u_j^{b\Sigma}$ and the jump of the traction $t_j^{b\Delta}$ across the crack surface, respectively. It is worth noting that both integral equations contain only weakly singular kernels $\{U_j^p,G_{mj}^p,C_{mj}^{tk},H_{ij}^p n_j\}$ of $\mathcal{O}(1/r)$. This positive feature renders the existence of all involved double surface integrals in an ordinary sense and their validity requires only C^0- boundary data.

2.3. Governing equations for two layers

The two layers S_c^+ and S_c^- shown in Figs. 2(b) and 2(c) are considered as infinitesimally thin membranes adhered perfectly to the bulk material. The behavior of these two layers is modeled by Gurtin-Murdoch surface elasticity theory by ignoring terms associated with the surface elastic constants. It has been pointed out by various investigations that the influence of the surface elastic constants on the out-of-plane responses in the region very near the surface is negligibly weak [10, 19-21]. The simplified version of the Gurtin-Murdoch model is therefore considered suitable for modeling planar crack problems especially when mode-I behavior is of primary interest.

The equilibrium equations, the surface constitutive relations and the strain-displacement relationship of the layers S_c^+ and S_c^- are therefore given by [2, 3]

$$\sigma_{i\beta,\beta}^s+t_i^s+t_i^o=0 \quad (9)$$

$$\sigma_{\alpha\beta}^s=\tau^s\left\{(1+\varepsilon_{\gamma\gamma}^s)\delta_{\alpha\beta}-u_{\beta,\alpha}^s\right\}\quad,\quad \sigma_{3\beta}^s=\tau^s u_{3,\beta}^s \quad (10)$$

$$\varepsilon_{\alpha\beta}^s=\frac{1}{2}\left(u_{\alpha,\beta}^s+u_{\beta,\alpha}^s\right) \quad (11)$$

where $\sigma_{i\beta}^s,\varepsilon_{\alpha\beta}^s,u_i^s$ represent stress, strain and displacement components within the layer.

To construct the weak-form equation, we multiply the equilibrium equation (9) with a sufficiently smooth test function $\tilde{u}_i^s$ and then integrate the result over the entire crack surface to obtain

$$\int_{S_c} \tilde{u}_i^s \sigma_{i\beta,\beta}^s dS + \int_{S_c} \tilde{u}_i^s t_i^s dS + \int_{S_c} \tilde{u}_i^s t_i^0 dS = 0 \tag{12}$$

By using the fact that τ^s is spatially independent, it can be readily verified that $\sigma_{\alpha\beta,\beta}^s = 0$. With such condition along with carrying out the integration by parts of the first term using the Gauss-divergence theorem, it leads to

$$\int_{S_c} \tilde{u}_{3,\beta}^s \sigma_{3\beta}^s dS - \int_{S_c} \tilde{u}_i^s t_i^s dS = \int_{\partial S_c} \tilde{u}_3^s \sigma_{3\beta}^s n_\beta dS + \int_{S_c} \tilde{u}_i^s t_i^0 dS \tag{13}$$

Substituting (10) into (13) finally yields

$$\tau^s \int_{S_c} \tilde{u}_{3,\beta}^s u_{3,\beta}^s dS - \int_{S_c} \tilde{u}_i^s t_i^s dS = \int_{\partial S_c} \tilde{u}_3^s \sigma_{3\beta}^s n_\beta dS + \int_{S_c} \tilde{u}_i^s t_i^0 dS \tag{14}$$

Note that the weak-form equation (14) applies to both crack surfaces. For instance, the weak-form equations for the surface S_c^+ and the surface S_c^- can be obtained explicitly by

$$\tau^s \int_{S_c} \tilde{u}_{3,\beta}^{+s} u_{3,\beta}^{+s} dS - \int_{S_c} \tilde{u}_i^{+s} t_i^{+s} dS = \int_{\partial S_c} \tilde{u}_3^{+s} \sigma_{3\beta}^{+s} n_\beta dS + \int_{S_c} \tilde{u}_i^{+s} t_i^{+0} dS \tag{15}$$

$$\tau^s \int_{S_c} \tilde{u}_{3,\beta}^{-s} u_{3,\beta}^{-s} dS - \int_{S_c} \tilde{u}_i^{-s} t_i^{-s} dS = \int_{\partial S_c} \tilde{u}_3^{-s} \sigma_{3\beta}^{-s} n_\beta dS + \int_{S_c} \tilde{u}_i^{-s} t_i^{-0} dS \tag{16}$$

where superscripts "+" and "–" are added to differentiate quantities defined on each crack surface. Since the integral equations governing the bulk material are derived in terms of the unknown sum and jump of quantities across the crack surface, it is natural to establish the weak-form equations governing the surface containing the same type of unknowns. This can be readily accomplished by forming two linear combinations of (15) and (16) as follows: (i) choosing $\tilde{u}_i^{+s} = \tilde{u}_i^{-s} = \tilde{u}_i^{s\Sigma}$ and then adding (15) to (16) and (ii) choosing $\tilde{u}_i^{+s} = \tilde{u}_i^{-s} = \tilde{u}_i^{s\Delta}$ and then subtracting (15) from (16). Such pair of equivalent weak-form equations is given by

$$\tau^s \int_{S_c} \tilde{u}_{3,\beta}^{s\Sigma} u_{3,\beta}^{s\Sigma} dS - \int_{S_c} \tilde{u}_i^{s\Sigma} t_i^{s\Sigma} dS = \int_{\partial S_c} \tilde{u}_3^{s\Sigma} \sigma_{3\beta}^{s\Sigma} n_\beta dS + \int_{S_c} \tilde{u}_i^{s\Sigma} t_i^{0\Sigma} dS \tag{17}$$

$$\tau^s \int_{S_c} \tilde{u}_{3,\beta}^{s\Delta} u_{3,\beta}^{s\Delta} dS - \int_{S_c} \tilde{u}_i^{s\Delta} t_i^{s\Delta} dS = \int_{\partial S_c} \tilde{u}_3^{s\Delta} \sigma_{3\beta}^{s\Delta} n_\beta dS + \int_{S_c} \tilde{u}_i^{s\Delta} t_i^{0\Delta} dS \tag{18}$$

where superscripts "Σ" and "Δ" indicate the sum and jump of quantities across the crack surface. It should be remarked further that since the jump of the displacement along the crack front vanishes identically, the test function $\tilde{u}_i^{s\Delta}$ is chosen to satisfy the homogeneous condition $\tilde{u}_i^{s\Delta} = 0$ on ∂S_c. In addition, the traction boundary conditions $\sigma_{3\beta}^{s\Sigma} n_\beta = 0$ on ∂S_c are assumed. The weak-form equations (17) and (18) finally become

$$\tau^s \int_{S_c} \tilde{u}_{3,\beta}^{s\Sigma} u_{3,\beta}^{s\Sigma} dS - \int_{S_c} \tilde{u}_i^{s\Sigma} t_i^{s\Sigma} dS = \int_{S_c} \tilde{u}_i^{s\Sigma} t_i^{0\Sigma} dS \tag{19}$$

$$\tau^s \int_{S_c} \tilde{u}_{3,\beta}^{s\Delta} u_{3,\beta}^{s\Delta} dS - \int_{S_c} \tilde{u}_i^{s\Delta} t_i^{s\Delta} dS = \int_{S_c} \tilde{u}_i^{s\Delta} t_i^{0\Delta} dS \tag{20}$$

Equations (19) and (20) constitute a set of weak-form equations governing the unknown quantities $\{u_i^{s\Delta}, t_i^{s\Delta}, u_i^{s\Sigma}, t_i^{s\Sigma}\}$. It is worth noting that the formulation presented above is clearly not restricted only to applied normal traction to the crack surface, although the mathematical model of the surface is physically suitable for pure mode-I loading. Due to the vanishing $\sigma_{\alpha\beta,\beta}^s$, the equilibrium equation (9) indicates that the applied shear traction is transmitted directly to the crack surface of the bulk material.

2.4. Governing equations for whole medium

Since the two layers S_c^+ and S_c^- are adhered perfectly to the bulk material, the displacements and tractions along the interface of the two layers and the bulk material must be continuous. This yields the following continuity conditions:

$$u_i^{s\Delta} = u_i^{b\Delta} \equiv u_i^{\Delta} \tag{21}$$

$$u_i^{s\Sigma} = u_i^{b\Sigma} \equiv u_i^{\Sigma} \tag{22}$$

$$t_i^{s\Delta} = -t_i^{b\Delta} \equiv -t_i^{\Delta} \tag{23}$$

$$t_i^{s\Sigma} = -t_i^{b\Sigma} \equiv -t_i^{\Sigma} \tag{24}$$

Substituting (21)-(24) into (7), (8), (19) and (20), leads to a system of four equations involving four unknown functions $\{u_i^{\Delta}, t_i^{\Delta}, u_i^{\Sigma}, t_i^{\Sigma}\}$. By choosing appropriate test functions, (8) and (20) can be combined and the unknown t_i^{Δ} can be eliminated. The final system of three equations involving three unknown functions $\{u_i^{\Delta}, u_i^{\Sigma}, t_i^{\Sigma}\}$ is given by

$$\begin{aligned} &\mathcal{A}(\tilde{\mathbf{u}}^{s\Sigma}, \mathbf{u}^{\Sigma}) + \mathcal{B}(\tilde{\mathbf{u}}^{s\Sigma}, \mathbf{t}^{\Sigma}) &&= \mathcal{R}_1(\tilde{\mathbf{u}}^{s\Sigma}) \\ &\mathcal{B}(\tilde{\mathbf{t}}^{\Sigma}, \mathbf{u}^{\Sigma}) + \mathcal{C}(\tilde{\mathbf{t}}^{\Sigma}, \mathbf{t}^{\Sigma}) + \mathcal{D}(\tilde{\mathbf{t}}^{\Sigma}, \mathbf{u}^{\Delta}) &&= 0 \\ &\mathcal{D}(\mathbf{t}^{\Sigma}, \tilde{\mathbf{u}}^{\Delta}) + \mathcal{E}(\tilde{\mathbf{u}}^{\Delta}, \mathbf{u}^{\Delta}) &&= \mathcal{R}_2(\tilde{\mathbf{u}}^{\Delta}) \end{aligned} \tag{25}$$

where the bilinear integral operators $\mathcal{A}, \mathcal{B}, \mathcal{C}, \mathcal{D}, \mathcal{E}$ are defined by

$$\mathcal{A}(\mathbf{X}, \mathbf{Y}) = \frac{\tau^s}{2} \int_{S_c} X_{3,\alpha}(\mathbf{y}) Y_{3,\alpha}(\mathbf{y}) dS(\mathbf{y}) \tag{26}$$

$$\mathscr{B}(\mathbf{X},\mathbf{Y})=\frac{1}{2}\int_{S_c} X_p(\mathbf{y})Y_p(\mathbf{y})dS(\mathbf{y}) \tag{27}$$

$$\mathscr{C}(\mathbf{X},\mathbf{Y})=-\int_{S_c} X_p(\mathbf{y})\int_{S_c} U_j^p(\boldsymbol{\xi}-\mathbf{y})Y_j(\boldsymbol{\xi})dS(\boldsymbol{\xi})dS(\mathbf{y}) \tag{28}$$

$$\begin{aligned}\mathscr{D}(\mathbf{X},\mathbf{Y})=&-\int_{S_c} X_p(\mathbf{y})\int_{S_c} G_{mj}^p(\boldsymbol{\xi}-\mathbf{y})D_m Y_j(\boldsymbol{\xi})dS(\boldsymbol{\xi})dS(\mathbf{y})\\ &+\int_{S_c} X_p(\mathbf{y})\int_{S_c} H_{ij}^p(\boldsymbol{\xi}-\mathbf{y})n_i(\boldsymbol{\xi})Y_j(\boldsymbol{\xi})dS(\boldsymbol{\xi})dS(\mathbf{y})\end{aligned} \tag{29}$$

$$\mathscr{E}(\mathbf{X},\mathbf{Y})=-\int_{S_c} D_t X_k(\mathbf{y})\int_{S_c} C_{mj}^{tk}(\boldsymbol{\xi}-\mathbf{y})D_m Y_j(\boldsymbol{\xi})dS(\boldsymbol{\xi})dS(\mathbf{y})+\mathscr{A}(\mathbf{X},\mathbf{Y}) \tag{30}$$

and the linear integral operators $\{\mathscr{R}_1,\mathscr{R}_2\}$ are defined, in terms of prescribed data $\mathbf{t}^{0\Sigma}$ and $\mathbf{t}^{0\Delta}$, by

$$\mathscr{R}_1(\mathbf{X})=\frac{1}{2}\int_{S_c} X_l(\mathbf{y})t_l^{0\Sigma}(\mathbf{y})dS(\mathbf{y}) \tag{31}$$

$$\mathscr{R}_2(\mathbf{X})=\frac{1}{2}\int_{S_c} X_l(\mathbf{y})t_l^{0\Delta}(\mathbf{y})dS(\mathbf{y}) \tag{32}$$

3. Numerical implementation

In this section, all numerical treatments including the discretization and numerical integration are briefly discussed. In general, standard procedures for the weakly singular SGBEM (e.g., [31, 32, 35, 37]) and those for the standard finite element method (e.g., [42-44]) are utilized to form the discretized system of linear algebraic equations.

3.1. Discretization

Standard Galerkin approximation is employed in the discretization of the system of governing equations (25). Since all involved boundary integrals contain only weakly singular kernels of $\mathscr{O}(1/r)$, standard C^0 interpolation functions are utilized in the approximation of both trial and test functions. In particular, the following approximation for the test functions and the trial functions is introduced:

$$\tilde{u}_i^{s\Sigma}=\sum_{p=1}^{N}\tilde{U}_{3(p-1)+i}^{s\Sigma}\Phi_p\ ;\quad u_i^{\Sigma}=\sum_{q=1}^{N}U_{3(q-1)+i}^{\Sigma}\Phi_q \tag{33}$$

$$\tilde{u}_i^{\Delta}=\sum_{p=1}^{N}\tilde{U}_{3(p-1)+i}\Phi_p\ ;\quad u_i^{\Delta}=\sum_{q=1}^{N}U_{3(q-1)+i}^{\Delta}\Phi_q \tag{34}$$

$$\tilde{t}_i^{\Sigma}=\sum_{p=1}^{N}\tilde{T}_{3(p-1)+i}\Phi_p\;;\quad t_i^{\Sigma}=\sum_{q=1}^{N}T_{3(q-1)+i}^{\Sigma}\Phi_q \tag{35}$$

where N is the number of nodal points; Φ_q is the nodal basis function at node q; $U_{3(q-1)+i}^{\Sigma}$, $U_{3(q-1)+i}^{\Delta}$, and $T_{3(q-1)+i}^{\Sigma}$ are nodal degrees of freedom associated with the sum of the displacement, the jump of the displacement and the sum of the traction across the crack surfaces, respectively; and $\tilde{U}_{3(p-1)+i}^{s\Sigma}$, $\tilde{U}_{3(p-1)+i}$, and $\tilde{T}_{3(p-1)+i}$ are arbitrary nodal quantities. Substituting (33)-(35) into (25) along with using the arbitrariness of $\tilde{U}_{3(p-1)+i}^{s\Sigma}$, $\tilde{U}_{3(p-1)+i}$, and $\tilde{T}_{3(p-1)+i}$, leads to a symmetric system of linear algebraic equations

$$\begin{bmatrix}\mathbf{A}&\mathbf{B}&\mathbf{0}\\ \mathbf{B}^T&\mathbf{C}&\mathbf{D}\\ \mathbf{0}&\mathbf{D}^T&\mathbf{E}\end{bmatrix}\begin{Bmatrix}\mathbf{U}^{\Sigma}\\ \mathbf{T}^{\Sigma}\\ \mathbf{U}^{\Delta}\end{Bmatrix}=\begin{Bmatrix}\mathbf{R}_1\\ \mathbf{0}\\ \mathbf{R}_2\end{Bmatrix} \tag{36}$$

where the sub-matrices $\mathbf{A},\mathbf{B},\mathbf{C},\mathbf{D},\mathbf{E}$ are associated with the bilinear operators $\mathscr{A},\mathscr{B},\mathscr{C},\mathscr{D},\mathscr{E}$; sub-vectors $\mathbf{R}_1,\mathbf{R}_2$ correspond to the linear operators $\mathscr{R}_1,\mathscr{R}_2$; $\mathbf{U}^{\Sigma}$ is a vector of nodal quantities of the sum of the displacement; $\mathbf{U}^{\Delta}$ is a vector of nodal quantities of the jump of the displacement and $\mathbf{T}^{\Sigma}$ is a vector of nodal quantities of the sum of the traction. The sub-matrices **A**, **B**, **C**, **D**, **E** and sub-vectors $\mathbf{R}_1,\mathbf{R}_2$ are given explicitly by

$$[\mathbf{A}]_{3(p-1)+3,3(q-1)+3}=\frac{\tau^s}{2}\int_{S_c}\Phi_{p,\gamma}(\boldsymbol{y})\Phi_{q,\gamma}(\boldsymbol{y})dS(\boldsymbol{y}) \tag{37}$$

$$[\mathbf{B}]_{3(p-1)+i,3(q-1)+j}=\frac{1}{2}\int_{S_c}\delta_{ij}\Phi_p(\boldsymbol{y})\Phi_q(\boldsymbol{y})dS(\boldsymbol{y}) \tag{38}$$

$$[\mathbf{C}]_{3(p-1)+i,3(q-1)+j}=-\int_{S_c}\Phi_p(\boldsymbol{y})\int_{S_c}U_j^i(\xi-\boldsymbol{y})\Phi_q(\xi)dS(\xi)dS(\boldsymbol{y}) \tag{39}$$

$$\begin{aligned}[\mathbf{D}]_{3(p-1)+i,3(q-1)+j}=&-\int_{S_c}\Phi_p(\boldsymbol{y})\int_{S_c}G_{mj}^i(\boldsymbol{\xi}-\boldsymbol{y})D_m\Phi_q(\boldsymbol{\xi})dS(\boldsymbol{\xi})dS(\boldsymbol{y})\\&+\int_{S_c}\Phi_p(\boldsymbol{y})\int_{S_c}H_{mj}^i(\boldsymbol{\xi}-\boldsymbol{y})n_m(\boldsymbol{\xi})\Phi_q(\boldsymbol{\xi})dS(\boldsymbol{\xi})dS(\boldsymbol{y})\end{aligned} \tag{40}$$

$$[\mathbf{E}]_{3(p-1)+i,3(q-1)+j}=-\int_{S_c}D_t\Phi_p(\boldsymbol{y})\int_{S_c}C_{mj}^{ti}(\boldsymbol{\xi}-\boldsymbol{y})D_m\Phi_q(\boldsymbol{\xi})dS(\boldsymbol{\xi})dS(\boldsymbol{y})+[\mathbf{A}]_{3(p-1)+i,3(q-1)+j} \tag{41}$$

$$[\mathbf{R}_1]_{3(p-1)+i}=\frac{1}{2}\int_{S_c}\Phi_p(\mathbf{y})t_i^{0\Sigma}(\mathbf{y})dS(\mathbf{y})\;;\quad[\mathbf{R}_2]_{3(p-1)+i}=\frac{1}{2}\int_{S_c}\Phi_p(\mathbf{y})t_i^{0\Delta}(\mathbf{y})dS(\mathbf{y}) \tag{42}$$

$$[\mathbf{U}^{\Sigma}]_{3(q-1)+i}=U_{3(q-1)+i}^{\Sigma}\;;\quad[\mathbf{U}^{\Delta}]_{3(q-1)+i}=U_{3(q-1)+i}^{\Delta}\;;\quad[\mathbf{T}^{\Sigma}]_{3(q-1)+i}=T_{3(q-1)+i}^{\Sigma} \tag{43}$$

3.2. Numerical integration

To evaluate the sub-matrices **A**, **B**, **C**, **D**, **E** and sub-vectors $\mathbf{R}_1$, $\mathbf{R}_2$ numerically, the single and double surface integrals must be properly treated. All single surface integrals contain regular integrands and can be efficiently and accurately integrated using standard Gaussian quadrature. Unlike single surface integrals, double surface integrals can be categorized into three types depending on a pair of elements resulting from the discretization of the surface S_c. The first type is termed a regular double surface integral since its integrand is not singular with only mild variation. This type of integral arises when both elements in a pair are relatively remote in comparison with their characteristic size. Similar to the single surface integral, all regular double surface integrals can be accurately integrated by Gaussian quadrature. The second type, termed weakly singular double surface integrals, arises when both elements in a pair are identical and their integrand is therefore weakly singular due to the involved kernels. Although these integrals exist in the sense of Riemann, it was pointed out by Xiao [45] that they cannot be efficiently integrated by standard Gaussian quadrature. To circumvent such difficulty, similar techniques based on integrand regularization via a series of transformations proposed by Li and Han [46], Hayami and Brebbia [47] and Xiao [45] are employed. The last type of double surface integrals, which are considered most challenging, is a nearly singular integral. The integrand of these integrals is nearly singular since both elements in a pair are relatively close in comparison with their characteristic size and this renders the kernels contained in those integrals not only nearly singular but also exhibiting rapid variation. Similar to the weakly singular integrals, Gaussian quadrature cannot be used to integrate nearly singular integrals efficiently. Special techniques proposed by Hayami [48], Hayami and Matsumoto [49], and Xiao [45] are systematically adopted to perform the numerical integration of this type of integrals.

4. Numerical results

First, to verify the formulation and numerical implementations, a penny-shaped crack in an unbounded domain is considered, to compare results with existing benchmark solutions. Next the elliptical crack and two interacting penny-shaped cracks in an unbounded domain are fully investigated.

In the analysis, three meshes with different levels of refinement are utilized to investigate the convergence of numerical solutions. Nine-node isoparametric elements are used to discretize the entire crack front while the other parts of the crack surfaces are discretized by eight-node and six-node isoparametric elements. The material Si [100] is used for all of numerical examples, where

properties of the bulk material and the residual surface tension $E = 107\,GPa$, $\nu = 0.33$ and $\tau^s = 0.6056\,N/m$ are obtained from Miller and Shenoy [50]. For convenience in the handling of numerical analysis, presentation of results, and demonstration of the influence of residual surface tension, all involved quantities are normalized in a proper fashion. For instance, the unknown sum of the traction is normalized by the shear modulus μ (i.e., $t_0^{\Sigma} = t^{\Sigma}/\mu$); the unknown sum and jump of the crack-face displacement are normalized by a special length scale $\Lambda = \tau^s/\mu = 0.01506\ nm$ (i.e., $u_0^{\Delta} = u^{\Delta}/\Lambda$ and $u_0^{\Sigma} = u^{\Sigma}/\Lambda$); all characteristic lengths representing the geometry of the crack such as the crack radius a, the semi-major axis a, and the semi-minor axis b used in following examples are normalized by the length scale Λ (e.g., $a_0 = a/\Lambda$ and $b_0 = b/\Lambda$); and the prescribed traction on the crack surface is normalized by the shear modulus μ (i.e., $t_{i0} = t_i^0/\mu$).

4.1. Penny-shaped crack in an unbounded domain

As a means for verifying the proposed technique, the problem of a penny-shaped crack of radius a embedded in an isotropic, linear elastic infinite medium is considered (Fig. 3(a)). The crack is subjected to self-equilibrated, uniformly distributed normal traction $t_3^+ = -t_3^- = t^0$. This problem has been previously solved analytically by [20, 21] using Hankel integral transforms and a special technique for solving dual integral equations and their results are employed as the benchmark solutions to validate the proposed FEM-SGBEM technique. The three meshes of the crack surface used in the numerical study are shown in Fig. 3(b).

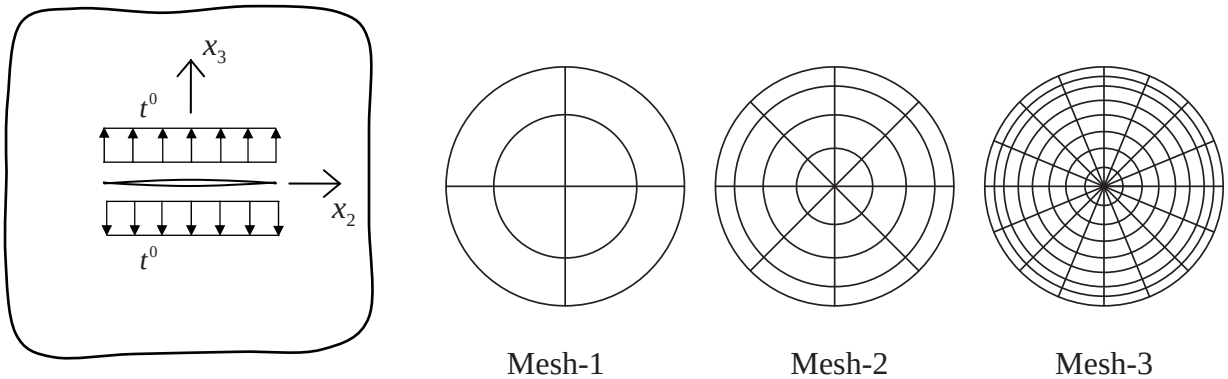

Fig. 3. (a) Schematic of a penny-shaped crack of radius a embedded in an isotropic, linear elastic infinite medium subjected to uniformly distributed normal traction $t_3^+ = -t_3^- = t^0$; (b) Meshes adopted in the analysis. Mesh-1: 8 elements and 29 nodes. Mesh-2: 32 elements and 105 nodes. Mesh-3: 128 elements and 401 nodes.

The normalized crack opening displacement and normalized stresses in the vicinity of the crack front, when the influence of the residual surface tension is taken into account, are shown in Fig. 4. Results are compared with those obtained by an analytical technique [20, 21]. It is seen that the current technique yields solutions that agree very well with the benchmark solutions for both crack opening displacement and stresses σ_{11}, σ_{22}, σ_{33} in the vicinity of the crack front. To further examine the influence of the residual surface tension, the normalized crack opening displacement and the normalized vertical stress σ_{33} in the vicinity of the crack front with different values of residual surface tension τ^s ranging from 0 to 1.0 *N/m* are reported in Fig. 5. It can be concluded that the residual surface tension exhibits significant influence on the crack opening displacement and the vertical stress. In particular, as τ^s becomes larger, the deviation of results from the classical case (i.e., without the residual surface tension) significantly increases and, clearly, it makes the elastic medium much stiffer.

To demonstrate the size-dependent behavior of results due to the presence of residual surface tension, the crack opening displacement and the vertical stress in the vicinity of the crack front are shown in Fig. 6 for both the classical case and the present study. It is evident that, by including the residual surface tension effects in the mathematical model, the solutions exhibit size-dependent behavior. In particular, the normalized crack opening displacement and vertical stress in the vicinity of crack front depend significantly on the crack size and this is in contrast with the classical case where the normalized crack opening displacement and normalized vertical stress are independent of crack radius.

4.2. Elliptical crack in infinite domain

To demonstrate the capability of the proposed technique for treating mode-I cracks of arbitrary shape, an elliptical crack embedded in an isotropic, linear elastic infinite domain is considered (see Fig. 7(a)). The crack front is parameterized in terms of a parameter t by

$$x_1 = a\cos t, \quad x_2 = b\sin t, \quad x_3 = 0; \quad t \in [0, 2\pi] \tag{44}$$

where a and b are the major and minor semi-axes of the crack, respectively. The crack is subjected to a self-equilibrated, uniformly distributed normal traction $t_3^+ = -t_3^- = t^0$. Numerical results are presented for the aspect ratio $a/b = 1, 2, 3$ and three meshes shown in Fig. 7(b) are used to model the elliptical crack.

The normalized crack opening displacement and the normalized stress σ_{33}/t^0 along the minor axis, when the influence of the residual surface tension is included, are presented in Fig. 8 for

aspect ratio $a/b = 1, 2, 3$. Clearly, converged results of the crack opening displacement are obtained with Mesh-2 and Mesh-3 for all three aspect ratios (see Fig. 8(a)). It can be seen in Fig. 8 that when the aspect ratio a/b increases, the influence of the residual surface tension on the crack opening displacement and the stresses near the crack decreases.

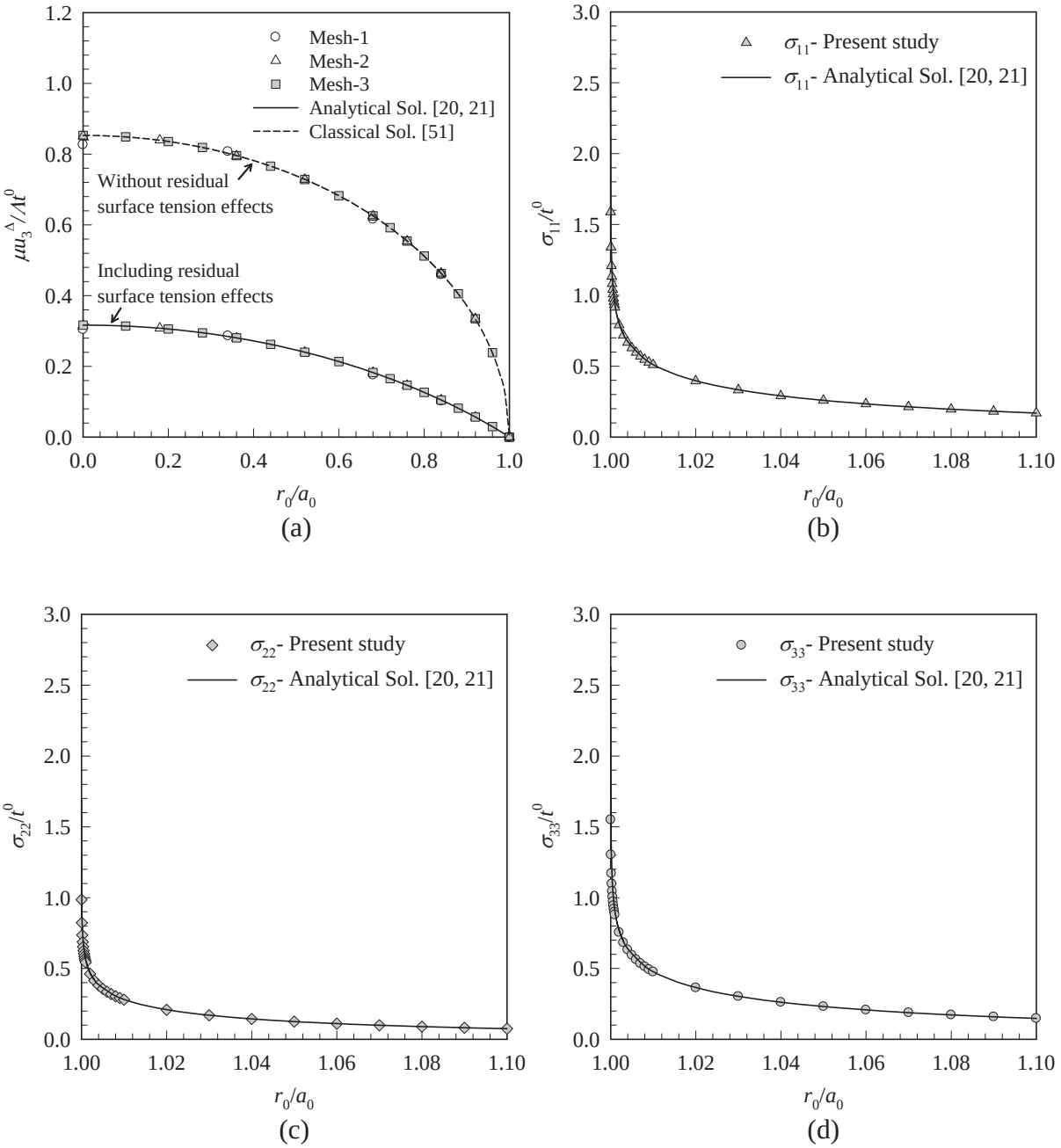

Fig. 4. Penny-shaped crack under uniformly distributed normal traction, for $E = 107\ GPa$, $\nu = 0.33$ and residual surface tension $\tau^s = 0.6056\ N/m$: (a) Normalized crack opening displacement, (b) Normalized stress σ_{11}/t^0 in the vicinity of the crack front, (c) Normalized stress σ_{22}/t^0 in the vicinity of the crack front, and (d) Normalized stress σ_{33}/t^0 in the vicinity of the crack front.

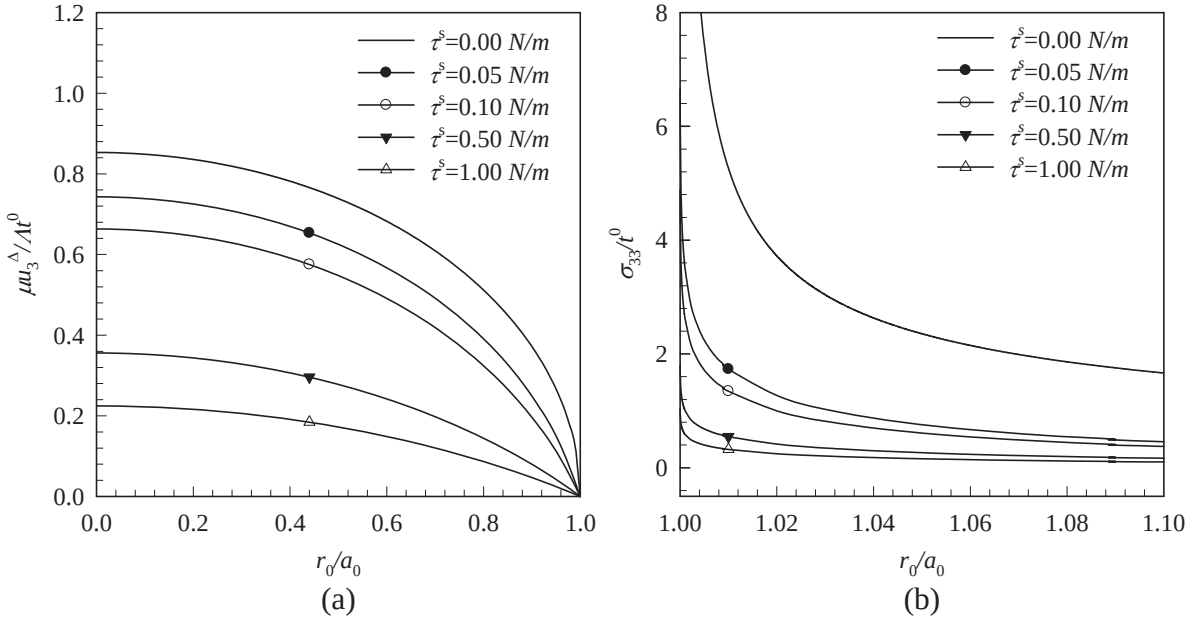

Fig. 5. Penny-shaped crack under uniformly distributed normal traction, for $E = 107\ GPa$, $\nu = 0.33$ for different residual surface tension τ^s: (a) Normalized crack opening displacement and (b) Normalized stress σ_{33}/t^0 in the vicinity of the crack front.

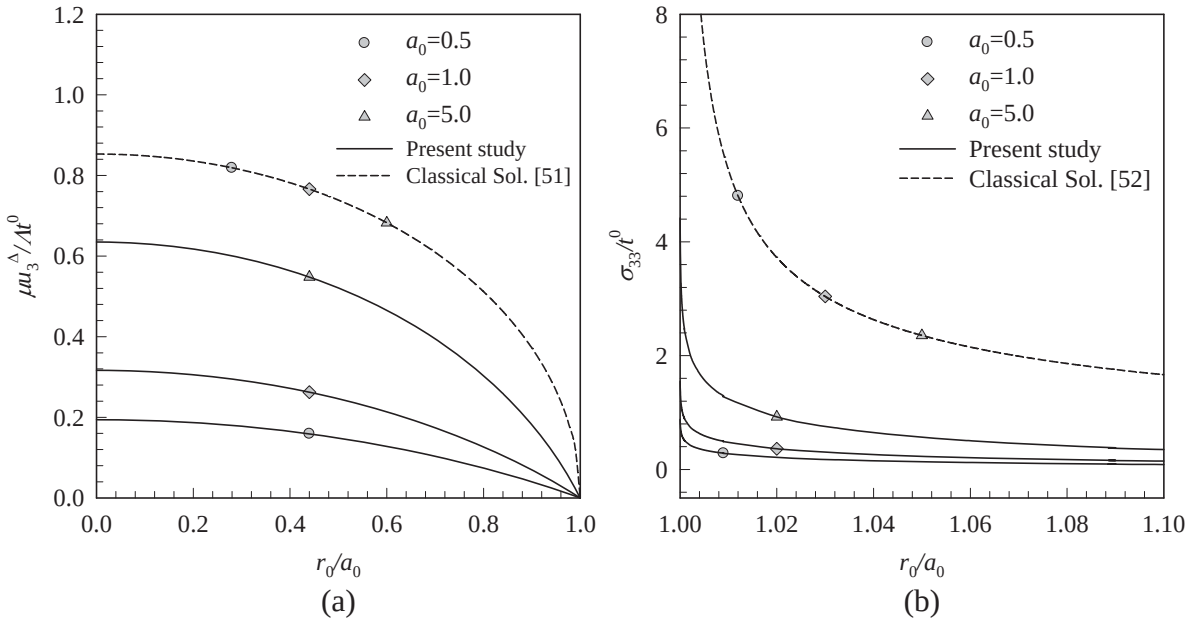

Fig. 6. Penny-shaped crack under uniformly distributed normal traction, for different crack radii $a_0 = a/\Lambda = 0.5, 1.0, 5.0$ for $E = 107\ GPa$, $\nu = 0.33$, $\tau^s = 0.6056\ N/m$: (a) Normalized crack opening displacement and (b) Normalized stress σ_{33}/t^0 in the vicinity of the crack front.

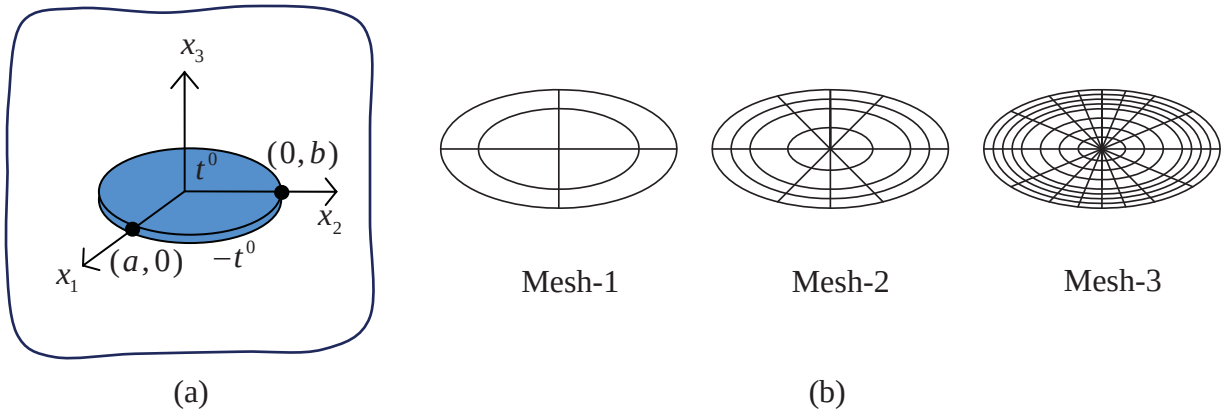

(a) (b)

Fig. 7. (a) Schematics of an elliptical crack embedded in an isotropic, linear elastic infinite medium subjected to uniformly distributed normal traction $t_3^+ = -t_3^- = t^0$ and (b) Meshes adopted in the analysis. Mesh-1: 8 elements and 29 nodes. Mesh-2: 32 elements and 105 nodes. Mesh-3: 128 elements and 401 nodes.

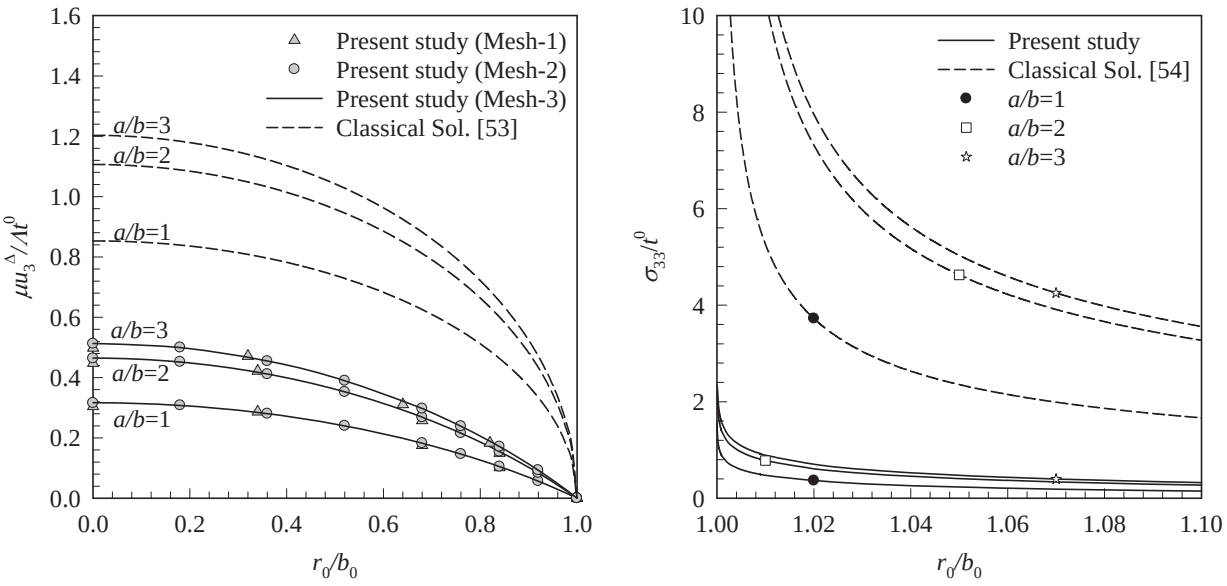

Fig. 8. Elliptical crack under uniformly distributed normal traction, for different aspect ratios $a/b = 1, 2, 3$ for $E = 107\ GPa$, $\nu = 0.33$, $\tau^s = 0.6056\ N/m$: (a) Normalized crack opening displacement along minor axis and (b) Normalized stress σ_{33}/t^0 in the vicinity of the crack front along the minor axis.

In order to demonstrate the influence of the residual surface tension, the normalized crack opening displacement and the normalized vertical stress σ_{33} in the vicinity of crack front with different values residual surface tension τ^s ranging from 0 to 1.0 *N/m* are reported in Fig. 9. Two aspect ratios, $a/b=2,3$, are considered in this particular case. As shown in Fig. 9, the influence of the residual surface tension is also significant and the medium is stiffer when the residual surface tension increases.

To examine the size-dependent behavior of results due to the influence of residual surface tension, the crack opening displacement and the vertical stress in the vicinity of the crack front for $a_0=0.5, 1.0, 5.0$ and two aspect ratios $a/b=2,3$ are shown in Fig. 10. As can be seen in Fig. 10, the normalized crack opening displacement and normalized stresses in the vicinity of the crack front are size-dependent. It is contrary to the classical case (i.e., without the residual surface tension) that the solutions are size-independent. When either the crack-size or the aspect ratio decreases, the influence of the residual surface tension becomes significant; in particular, it renders the medium stiffer.

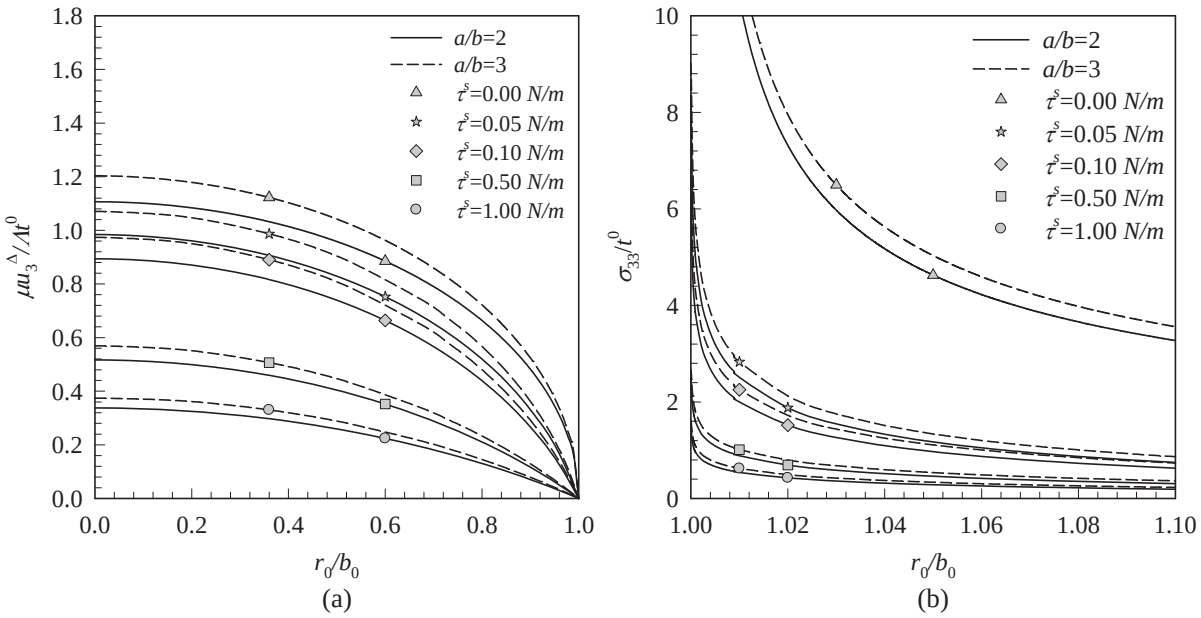

Fig. 9. Elliptical crack under uniformly distributed normal traction for different residual surface tension τ^s , for $E=107\,GPa$, $\nu=0.33$, for different aspect ratios $a/b=2,3$: (a) Normalized crack opening displacement along the minor axis and (b) Normalized stress σ_{33}/t^0 in the vicinity of the crack front along the minor axis.

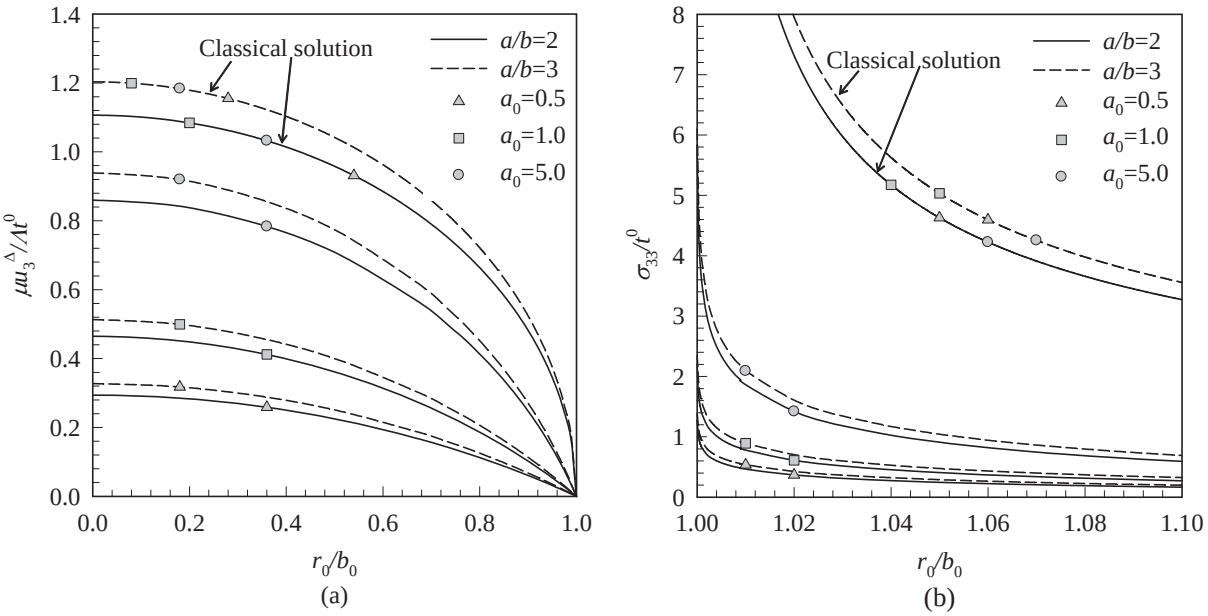

Fig. 10. Elliptical crack under uniformly distributed normal traction for different crack radii $a_0 = a/\Lambda = 0.5, 1.0, 5.0$ for $E = 107\ GPa$, $\nu = 0.33$, $\tau^s = 0.6056\ N/m$, for different aspect ratios $a/b = 2, 3$: (a) Normalized crack opening displacement along the minor axis and (b) Normalized stress σ_{33}/t^0 in the vicinity of the crack front along the minor axis.

4.3. Two interacting penny-shaped cracks in an unbounded domain

As a final example, we demonstrate another feature of the current technique, viz. modeling multiple cracks, by considering a pair of identical penny-shaped cracks of radius *a* embedded in an isotropic, linear elastic unbounded domain as shown in Fig. 11(a). The distance between the centers of the two cracks is denoted by *h*. Both cracks are subjected to a self-equilibrated, uniformly distributed normal traction $t_3^+ = -t_3^- = t^0$. Here, the influence of the interaction between the two cracks on the maximum crack opening displacement is considered. To investigate the size-dependent behavior, two cases are considered where the normalized radii of the identical penny-shaped cracks are taken as $a_0 = 1$ and 10. The three meshes shown in Fig. 11(b) are used to test the convergence of numerical solutions.

The normalized crack opening displacement of one of the penny-shaped cracks with radius $a_0 = 10$ is shown in Fig. 12 for $h/a = 2.4$. It is seen that converged results of the normalized crack opening displacement are obtained and the residual surface tension has a significant influence on the predicted crack opening displacement.

To study the interaction between the two cracks, the normalized maximum crack opening displacement is plotted for different values of h/a in Fig. 13. It can be observed in Fig. 13 that, in agreement with the previous examples of a penny-shaped crack and an elliptical crack, the maximum crack opening displacement decreases when the residual surface tension increases. The medium becomes much stiffer when the residual surface tension is taken into account.

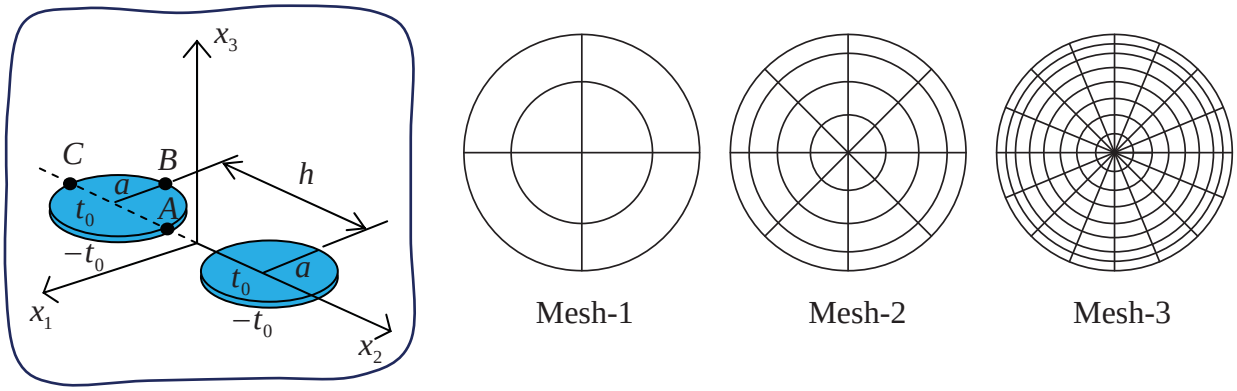

(a) (b)

Fig. 11. (a) Schematic of a pair of penny-shaped cracks of radius a embedded in an isotropic, linear elastic infinite medium subjected to uniformly distributed normal traction $t_3^+ = -t_3^- = t^0$ and (b) Meshes adopted for each crack. Mesh-1: 8 elements and 29 nodes. Mesh-2: 32 elements and 105 nodes. Mesh-3: 128 elements and 401 nodes.

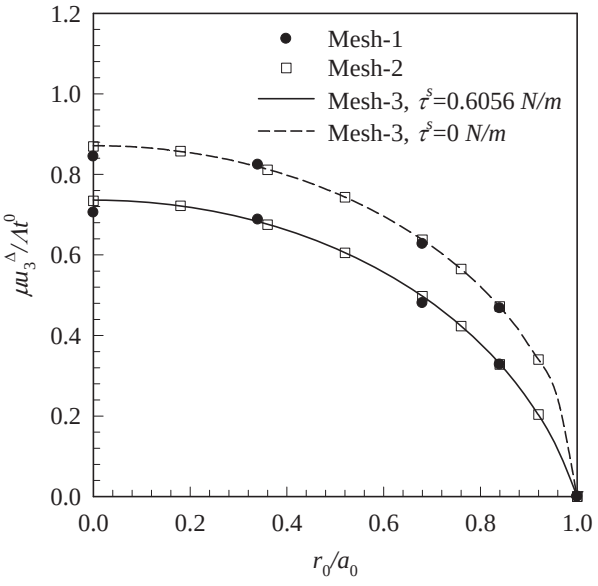

Fig. 12. Normalized crack opening displacement for a pair of penny-shaped cracks with radius $a_0 = 10$ and $h/a = 2.4$ under uniformly distributed normal traction, for $E = 107\,GPa$, $\nu = 0.33$ and $\tau^s = 0.6056\,N/m$.

It can also be observed from Figs. 13(a), 13(b) and 13(c) that results for the case of two interacting cracks converge very fast to those of a single crack when the residual surface tension increases. In particular, as the value of h/a is greater than 8, 5 and 3.5 for the classical case, $\tau^s = 0.6056\,N/m$, and $\tau^s = 1\,N/m$, respectively, the normalized maximum crack opening displacement of the two interacting crack and that of the single crack are nearly identical. This not only implies the significant reduction of the interaction between the two cracks due to the presence of the residual surface tension but also provides the applicable range of the aspect ratio h/a to allow the replacement of the two-crack model by the single crack model. In addition, as clearly indicated in Figs. 13(a) and 13(d), the interaction between the two cracks for the classical case is size-independent (i.e., solutions of the two cracks converge asymptotically to that of the single crack in the identical manner). On the contrary, when the residual surface tension is incorporated in the mathematical model, the size-dependent behavior can be clearly observed by comparing results in Figs. 13(b), 13(e) and results in Figs. 13(c), 13(f), respectively. The decrease in the crack size also lowers the interaction between the two cracks.

5. Conclusions

A computationally efficient numerical technique capable of modeling mode-I planar cracks in three-dimensional, linearly elastic media incorporating the influence of residual surface tension has been established. The governing equations have been formulated based on the classical theory of linear elasticity for the bulk medium and the Gurtin-Murdoch surface elasticity model for the infinitesimally thin layers on the crack surfaces. The fully coupled system of governing equations has been solved numerically by using the FEM-SGBEM coupling procedure. Numerical results for the penny-shaped crack problem have been compared with the analytical solution to validate the formulation and the proposed FEM-SGBEM method. By solving both the elliptical crack and two interacting cracks problems, the current technique has been found computationally promising to treat mode-I planar cracks including residual surface tension effects, for arbitrary shaped cracks and multiple cracks in three-dimensional isotropic linear elastic media. It has also been shown that the residual surface tension has a significant influence on the crack opening displacement and stresses in the vicinity of the crack front. Consideration of the surface stresses in the mathematical model not only renders the material stiffer but also introduces the size-dependency behavior of the solution. The presence of the residual surface tension also tends to weaken the interaction among cracks.

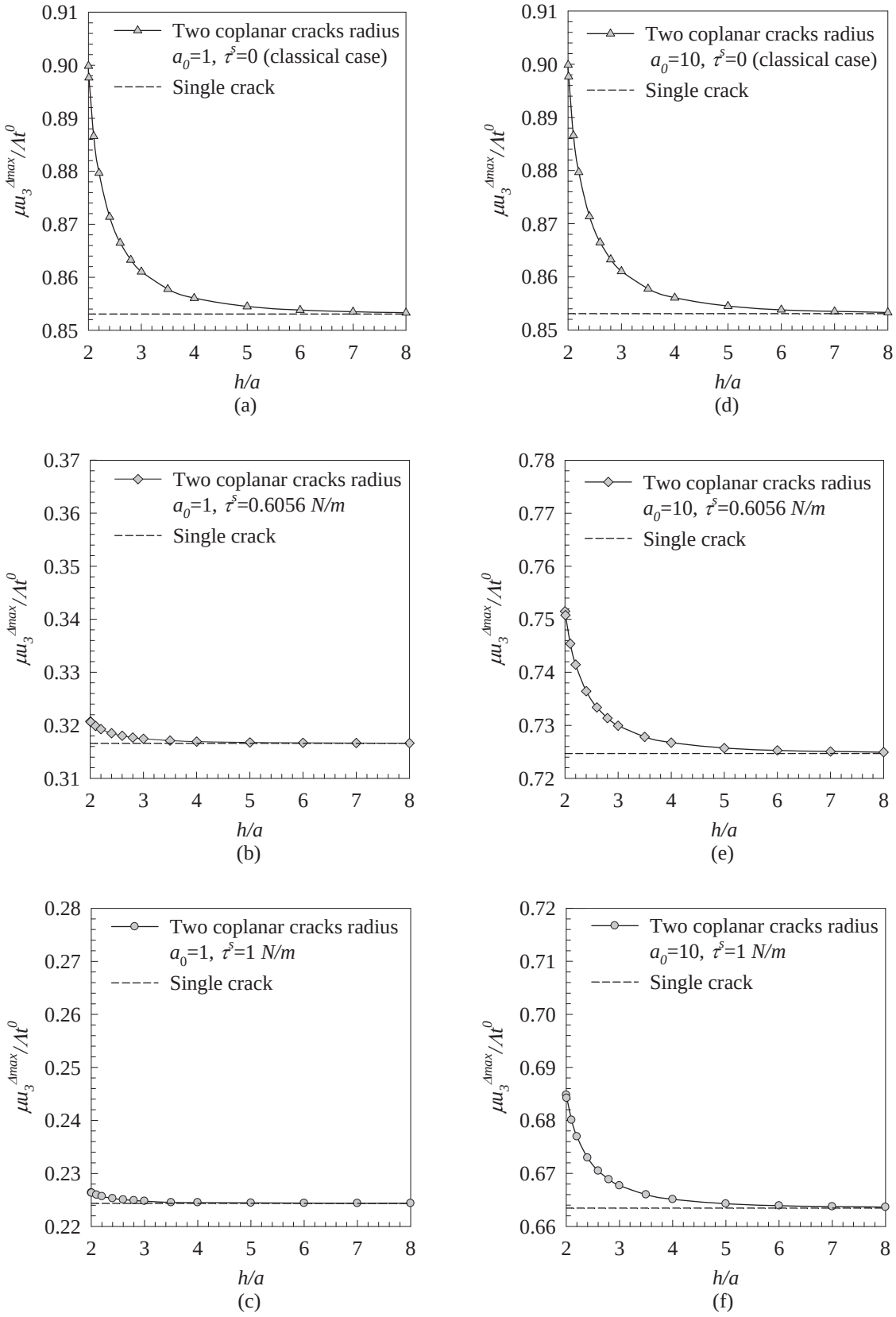

Fig. 13. Normalized maximum crack opening displacement for a pair of identical penny-shaped cracks under uniformly distributed normal traction, for $E = 107\ GPa$, $\nu = 0.33$: (a)-(c) $a_0 = 1$ and (d)-(f) $a_0 = 10$.

Acknowledgements

The first author is very grateful for a JICA AUN/SEED-Net scholarship. Financial support from JICA AUN/SEED-Net and Thailand Research Fund through Grant No. MRG5380159 and Grant No. BRG5480006 are gratefully acknowledged. Some parts of the work presented in this paper were completed while the first author was visiting Tokyo Institute of Technology.

References

[1] Yakobson, B. I., Nanomechanics. In: Goddard, W. A., Brenner, D. W., Lyshevski, S. E. and Iafrate G. J. editors, Handbook of nanoscience, engineering and technology. CRC Press, Boca Raton, 2003, pp. 17-1–17-18.

[2] Gurtin, M. E. and Murdoch, A. I., A continuum theory of elastic material surfaces, Archive for Rational Mechanics and Analysis 1975; 57(4):291-323.

[3] Gurtin, M. E. and Murdoch, A. I., Surface stress in solids, International Journal of Solids and Structures 1978; 14(6):431-440.

[4] He, L. H., Lim, C. W. and Wu, B. S., A continuum model for size-dependent deformation of elastic films of nano-scale thickness, International Journal of Solids and Structures 2004; 41(3-4): 847-857.

[5] Dingreville, R., Qu, J. and Cherkaoui, M., Surface free energy and its effect on the elastic behavior of nano-sized particles, wires and films, Journal of the Mechanics and Physics of Solids 2005; 53(8):1827-1854.

[6] Huang, D. W., Size-dependent response of ultra-thin films with surface effects, International Journal of Solids and Structures 2008; 45(2):568-579.

[7] Tian, L. and Rajapakse, R. K. N. D., Finite element modeling of nanoscale inhomogeneities in an elastic matrix, Computational Materials Science 2007; 41(1):44-53.

[8] Tian, L. and Rajapakse, R. K. N. D., Analytical Solution for Size-Dependent Elastic Field of a Nanoscale Circular Inhomogeneity, ASME Journal of Applied Mechanics 2007; 74(3):568-574.

[9] Tian, L. and Rajapakse, R. K. N. D., Elastic field of an isotropic matrix with a nanoscale elliptical inhomogeneity, International Journal of Solids and Structures 2007; 44(24):7988-8005.

[10] Pinyochotiwong, Y., Rungamornrat, J., Senjuntichai, T., Rigid frictionless indentation on

elastic half space with influence of surface stresses, International Journal of Engineering Science 2013; 71(0): 15-35.

[11] Wu, C. H., The effect of surface stress on the configurational equilibrium of voids and cracks, Journal of the Mechanics and Physics of Solids 1999; 47(12):2469-2492.

[12] Wang, G. F., Feng, X. Q., Wang, T. J. and Gao, W., Surface Effects on the Near-Tip Stresses for Mode-I and Mode-III Cracks, ASME Journal of Applied Mechanics 2008; 75(1):011001-011005.

[13] Fu, X. L., Wang, G. F. and Feng, X. Q., Surface effects on the near-tip stress fields of a mode-II crack, International Journal of Fracture 2008; 151(2):95-106.

[14] Fu, X. L., Wang, G. F. and Feng, X. Q., Surface effects on mode-I crack tip fields: A numerical study, Engineering Fracture Mechanics 2010; 77(7):1048-1057.

[15] Fang, Q. H., Liu, Y., Liu, Y. W. and Huang, B. Y., Dislocation emission from an elliptically blunted crack tip with surface effects, Physica B: Condensed Matter 2009; 404(20):3421-3424.

[16] Kim, C. I., Schiavone, P. and Ru, C. Q., Analysis of a mode-III crack in the presence of surface elasticity and a prescribed non-uniform surface traction, Zeitschrift für angewandte Mathematik und Physik 2010; 61(3):555-564.

[17] Kim, C. I., Schiavone, P. and Ru, C. Q., The effect of surface elasticity on a Mode-III interface crack, Archives of Mechanics 2011; 63(3):267-286.

[18] Kim, C. I., Schiavone, P. and Ru, C. Q., Analysis of Plane-Strain Crack Problems (Mode-I & Mode-II) in the Presence of Surface Elasticity, Journal of Elasticity 2011; 104(1):397-420.

[19] Nan, H. and Wang, B., Effect of residual surface stress on the fracture of nanoscale materials, Mechanics Research Communications 2012; 44(0):30-34.

[20] Intarit, P., Senjuntichai, T., Rungamornrat, J. and Rajapakse, R. K. N. D., Stress analysis of penny-shaped crack considering the effects of surface elasticity, Proceedings of 20th Annual International Conference on Composites or Nano Engineering (ICCE-20), Ramada Beijing North Hotel, Beijing, P.R. China 2012.

[21] Intarit, P., Solutions of elastic medium with surface stress effects, Ph.D. Dissertation 2013, Chulalongkorn University, Thailand.

[22] Blandford, G. E., Ingraffea, A. R. and Liggett, J. A., Two-diemnsional stress intensity factor computation using boundary element method, International Journal for Numerical Methods in

Engineering 1981; 17: 387-440

[23] Cruse, T. A., Boundary element analysis in computational fracture mechanics, Kluwer Academic Publishers, Dordrecht, 1988.

[24] Gray, L. J., Martha, L. F. and Ingraffea, A. R., Hypersingular integrals in boundary element fracture analysis, International Journal for Numerical Methods in Engineering 1990; 29: 1135-1158.

[25] Sutradhar, A. and Paulino, G. H., Symmetric Galerkin boundary element computation of T-stress and stress intensity factors for mixed-mode cracks by the interaction integral method, Engineering Analysis with Boundary Elements 2004; 28(11): 1335-1350

[26] Pan, E. and Yuan, F. G., Boundary element analysis of three-dimensional cracks in anisotropic solids, International Journal for Numerical Methods in Engineering 2000; 48: 211-237

[27] Saez, A., Ariza, M. P. and Dominguez, J., Three-dimensional fracture analysis in transversely isotropic solids, Engineering Analysis with Boundary Elements 1997; 20: 287-298.

[28] Gu, H. and Yew, C. H., Finite element solution of a boundary integral equation for mode I embedded three-dimensional fractures, International Journal for Numerical Methods in Engineering 1988; 26:1525-1540.

[29] Xu, G., Ortiz, M., A variational boundary integral method for the analysis of 3-D cracks of arbitrary geometry modeled as continuous distributions of dislocation loops, International Journal for Numerical Methods in Engineering 1993; 36: 3675-3701.

[30] Bonnet, M., Regularized direct and indirect symmetric variational BIE formulations for three-dimensional elasticity, Engineering Analysis with Boundary Elements 1995; 15: 93-102.

[31] Li, S., Mear, M. E., Singularity-reduced integral equations for displacement discontinuities in three-dimensional linear elastic media, International Journal of Fracture 1998; 93: 87-114.

[32] Li, S., Mear, M. E. and Xiao, L., Symmetric weak-form integral equation method for three-dimensional fracture analysis, Computer Methods in Applied Mechanics and Engineering 1998; 151: 435-459.

[33] Xu, G., A variational boundary integral method for the analysis of three-dimensional cracks of arbitrary geometry in anisotropic elastic solids, Journal of Applied Mechanics 2000; 67: 403-408.

[34] Frangi, A., Novati, G., Springhetti, R. and Rovizzi, M., 3D fracture analysis by the symmetric

Galerkin BEM, Computational Mechanics 2002; 28: 220-232.

[35] Rungamornrat, J., Analysis of 3D cracks in anisotropic multi-material domain with weakly singular SGBEM, Engineering Analysis with Boundary Elements 2006; 30 (10): 834-846.

[36] Rungamornrat, J. and Mear, M. E., Weakly-singular, weak-form integral equations for cracks in three-dimensional anisotropic media, International Journal of Solids and Structures 2008; 45(5):1283-1301.

[37] Rungamornrat, J. and Mear, M. E., A weakly-singular SGBEM for analysis of cracks in 3D anisotropic media, Computer Methods in Applied Mechanics and Engineering 2008; 197:4319-4332.

[38] Rungamornrat, J. and Senjuntichai, T., Regularized boundary integral representations for dislocations and cracks in smart media, Smart materials and structures 2009; 18:074010 (14pp).

[39] Frangi, A. and Novati, G., BEM-FEM coupling for 3D fracture mechanics applications, Computational Mechanics 2003; 32: 415-422

[40] Rungamornrat, J. and Mear, M. E., SGBEM-FEM coupling for analysis of cracks in 3D anisotropic media, International Journal for numerical methods in Engineering 2011; 86: 224-248.

[41] Bonnet, M., Maier, G. and Polizzotto, C., Symmetric Galerkin boundary element methods, Applied Mechanics Reveiws 1998; 51: 669-703.

[42] Bathe, K.J., Finite Element Procedures, Prentice-Hall, New Jersey, 1990.

[43] Hughes, T.J.R., The finite element method: linear static and dynamic finite element analysis, Dover Publications, New Jersey, 2000.

[44] Zienkiewicz, O.C., Taylor, R.L., The finite element method: Solid mechanics, volume 2, Butterworth-Heinemann, Oxford, 2000.

[45] Xiao, L., Symmetric weak-form integral equation method for three-dimensional fracture analysis, Ph.D. Dissertation 1998, The University of Texas at Austin, Texas.

[46] Li, H.B. and Han, G.M., A new method for evaluating singular integral in stress analysis of solids by the direct boundary element method, International Journal for Numerical Methods in Engineering 1985; 21: 2071-2098.

[47] Hayami, K. and Brebbia, C.A., Quadrature methods for singular and nearly singular integrals

in 3-D boundary element method, Boundary Element X, 1988, 237-264, Springer-Verlag, Berlin.

[48] Hayami, K., A projection transformation method for nearly singular surface boundary element integrals. In: Brebbia, c.a., Orszag, S.A. (eds) Lecture notes in Engineering 1992; 73; 1-2. Springer-Verlag, Berlin.

[49] Hayami, K. and Matsumoto, H., A numerical quadrature for nearly singular boundary element integrals, Engineering Analysis with Boundary Elements 1994; 13: 143-154.

[50] Miller, R. E. and Shenoy, V. B., Size-dependent elastic properties of nanosized structural elements, Nanotechnology 2000; 11(3):139-147.

[51] Tada, H., Paris, P. C., and Irwin, G. R., The Stress Analysis of Cracks Handbook, American Society of Mechanical Engineers, 2000.

[52] Kassir, M.K., Sih, G.C., Three-dimensional Crack Problems: A New Selection of Crack Solutions in Three-dimensional Elasticity, vol. 2, Noordhoff International Publishing, Leyden, 1975.

[53] Zeng-shen, C., Discussion on the SIF for points on border of elliptical flat crack inside infinite solid under uniform tension, Applied Mathematics and Mechanics 1982; 3(4): 521-526.

[54] Green, A. E., Sneddon, I. N., The distribution of stress in the neighborhood of a flat elliptical crack in an elastic solid, Mathematical Proceedings of the Cambridge Philosophical Society 1950; 46(1):159–163.

ANALYSIS OF 3D PLANAR CRACKS WITH CONSIDERATION OF SURFACE STRESS EFFECTS

Thai Binh Nguyen[1], Jaroon Rungamornrat[2*], Teerapong Senjuntichai[3] and Anil C. Wijeyewickrema[4]

[1,2,3]Department of Civil Engineering, Faculty of Engineering, Chulalongkorn University, Bangkok, Thailand

[4]Department of Civil and Environmental Engineering, Tokyo Institute of Technology, Tokyo, Japan

E-mails: Binh.T@student.chula.ac.th[1], Jaroon.R@chula.ac.th[2], Teerapong.S@chula.ac.th[3], wijeyewickrema.a.aa@m.titech.ac.jp[4]

Received Date: Xxxxxxxx xx, 2014

Abstract

An efficient numerical procedure for modeling planar cracks in a three-dimensional, linear elastic, infinite medium which accounts for the influence of surface stresses is presented in this paper. The concept of surface stresses, which has been widely employed in the investigation of nano-scale problems, is considered in the present study to derive a suitable mathematical model capable of simulating nano-sized cracks. An infinitesimally thin layer of material on the crack surface is modeled by a zero-thickness surface perfectly bonded to the bulk material, with its behavior governed by the Gurtin-Murdoch constitutive relation. In the formulation, the classical theory of isotropic linear elasticity is utilized to establish the governing equation of the bulk material in terms of completely regularized boundary integral equations for the displacement and traction on the crack surface. For the zero-thickness layer, the final governing equation incorporating the surface stress effect is obtained in a weak form following the standard weighted residual technique. The fully coupled system of equations is then solved by the FEM-SGBEM coupling numerical procedure. Due to the weakly singular feature of all involved boundary integral equations, standard continuous interpolation functions can be employed everywhere in the approximation of crack-face data and only special quadrature for evaluating nearly singular and weakly singular integrals is required. Once the implemented numerical scheme is validated with available benchmark solutions, it is applied to investigate the nano-scale influence of nano-sized cracks. Results from an extensive parametric study reveal that, the presence of surface stresses not only increases the near-surface material stiffness but also introduces size dependent behavior of solutions and the reduction of stresses in the region ahead of the crack front.

Keywords: FEM-SGBEM Coupling, Gurtin-Murdoch Model, Nano-sized Cracks, Size Dependency, Surface Stresses.

Introduction

Nano-structured materials such as nano-belts, nano-springs, nano-wires, nano-tubes, and nano-composites have received much attention in various fields in recent years due to their desirable and unique features. One obvious example of their vast applications is the invention of nano-scale components and devices. In the design procedure, analysis and assessment of failure/damage have been found to be an essential step that must be properly considered to ensure the safety and integrity throughout their lifespan. While conventional linear elastic fracture mechanics has been well established and successfully employed as a tool in the modeling of existing defects/flaws in linear elastic media at a macroscopic scale, those hypothetical models have failed to simulate the problem of nano-sized cracks due to the limitation of their underlying governing physics and simplified assumptions. The enhancement of classical continuum-based fracture models to properly incorporate the nano-scale influence is, therefore, required in order to accurately capture inherent physical

characteristics at such a small scale. Atomistic and molecular dynamics simulations have demonstrated that atoms in the vicinity of the free surface behave differently from those within the bulk material and effects of the surface free energy on the mechanical behavior can be very important at the nano-scale level. This near-surface phenomenon is one of the most important factors rendering the difference between macroscopic and nano-scale structures and must be properly integrated into the continuum-based models.

Gurtin and Murdoch [1] and Gurtin et al. [2] proposed a well-known, surface elasticity, continuum-based theory to enhance the modeling capability to capture the effects of surface free energy in solid materials. In their model, the surface is assumed to be elastic and very thin, which can be mathematically modeled as a layer of zero thickness perfectly bonded to the bulk material. The behavior of such an idealized surface is governed by a linear constitutive law involving surface material parameters different from those of the bulk material. In the past two decades, the Gurtin-Murdoch surface elasticity theory has been widely used to investigate various nano-scale problems (e.g., nano-scale elastic films [3-5], nano-sized particles and wires [4], nano-scale inhomogeneities [6-8], nano-indentations [9], etc.) and has also been validated because results predicted by this continuum-based model exhibit reasonably good agreement with those from atomistic and molecular dynamics simulations [4,10-12].

The Gurtin-Murdoch surface elasticity model has also been utilized in the investigation of nano-sized cracks; however, on the basis of an extensive literature survey, most existing studies are still limited to certain problem settings, formulations and solution techniques. For instance, studies of nano-sized cracks under various loading conditions using either the two-dimensional, blunt-crack or classical sharp-crack models can be extensively found in [12-16] and [17-21], respectively. In those studies, analytical, semi-analytical or numerical techniques were proposed to solve the associated boundary value problem. It should be remarked that while use of two-dimensional models in the simulation significantly reduces both theoretical and computational efforts, it, at the same time, poses several drawbacks including the loss of out-of-plane information and limited capability to treat cracks of general geometry. Recently, Intarit et al. [22] and Intarit [23] successfully developed an analytical technique based on Hankel integral transforms to investigate the influence of surface stresses on the behavior of three-dimensional, nano-sized cracks. Nevertheless, due to the limitation of their solution technique, only penny-shaped cracks under axisymmetric loading can be considered. In practical situations, nano-sized crack problems can be very complex in terms of geometries, loading conditions, and influences to be treated (e.g., surface free energy and residual surface tension). As a result, the development of a fully three-dimensional model and an efficient and powerful numerical procedure to enhance the capability of existing techniques is essential and still requires rigorous investigations. Most recently, Nguyen et al. [24] developed a computational procedure based on the coupling of the finite element technique and the boundary integral equation method to model nano-sized planar cracks in an infinite elastic medium. While their technique is applicable to planar cracks of arbitrary shapes, the formulation is still restricted to a limited version of Gurtin-Murdoch model accounting only for the residual surface tension and the implementation was carried out within the context of pure mode-I loading conditions.

The present study directly generalizes the work of Nguyen et al. [24] to incorporate the full Gurtin-Murdoch surface elasticity model including both surface elasticity and residual surface tension in modeling the zero-thickness layer. The incorporation of in-plane elasticity of the surface renders the mathematical model more complete and well-suited for studying the influence of in-plane surface stress on essential fracture data such as relative crack-face displacement and near-tip field, and the size-dependent behavior of the predicted solution.

Problem Formulation

In this section, the description of the boundary value problem considered in the present study is clearly stated and then the formulation of the key governing equations for both the bulk material and the zero-thickness layer on the crack surface are briefly summarized. The fully coupled system of governing equations resulting from the enforcement of interfacial conditions is finally presented.

Problem Description

Consider a three-dimensional, linearly elastic, infinite medium Ω containing an isolated, planar crack of arbitrary shape with a selected reference Cartesian coordinate system $\{O; x_1, x_2, x_3\}$, as shown schematically in Figure 1(a). The crack is represented by two geometrically identical surfaces, denoted by S_c^+ and S_c^- with the corresponding outward unit normal vectors $\mathbf{n}^+$ and $\mathbf{n}^-$, and, for convenience in further development, is oriented perpendicular to the x_3-axis. In the present study, the medium is assumed free of body forces and remote loading, but subjected to prescribed, self-equilibrated, normal tractions $\mathbf{t}^{0+}$ and $\mathbf{t}^{0-}$ on the crack surfaces S_c^+ and S_c^-, respectively (see Figure 1(b)). An infinitesimally thin layer on each crack surface possesses a constant residual surface tension τ^s (under unstrained conditions) and the surface Lamé constants λ^s and μ^s, whereas the rest of the medium, termed the "*bulk material*", is made of a homogeneous, isotropic, linearly elastic material with shear modulus μ and Poisson's ratio ν.

A clear problem statement of the present study is, to determine the complete elastic field including the displacements and stresses within the bulk material by taking the influence of surface stresses into account. Fracture related information such as relative crack-face displacement and local stress field in the vicinity of the crack front is also of primary interest.

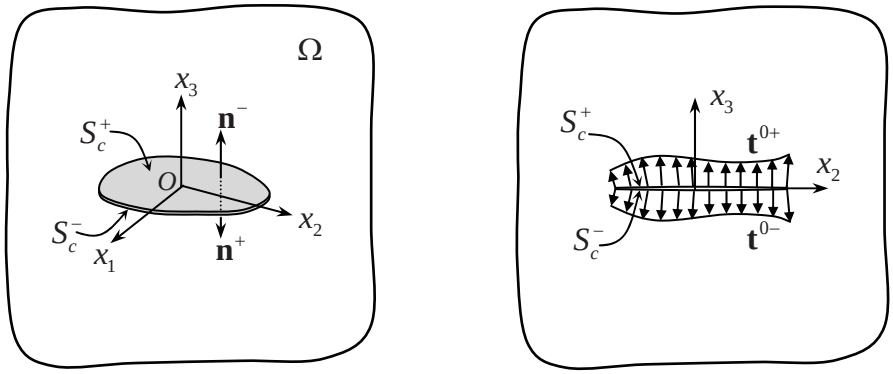

(a) (b)

Figure 1: (a) Schematic of a planar crack embedded in a three-dimensional, linearly elastic, infinite medium and (b) prescribed normal traction on crack surfaces.

Governing Equations

In the formulation of the boundary value problem, the whole medium is first decomposed into three parts: the bulk, a layer of zero thickness on the surface S_c^+, and a layer of zero thickness on the surface S_c^-. Both the zero-thickness layers are assumed to be perfectly bonded to the bulk material.

Since the bulk material is made of a homogeneous, isotropic, linearly elastic material, the classical theory of isotropic linear elasticity is used to describe its behavior. For convenience in the treatment of an infinite body containing cracks, the final governing equations are given in terms of boundary integral equations for the sum of the displacement and the jump of the tractions across the crack surface as (see details in Rungamornrat and Mear [28] and Rungamornrat and Senjuntichai [30]),

$$\begin{aligned}\frac{1}{2}\int_{S_c}\tilde{t}_p^{\Sigma}(\mathbf{y})u_p^{b\Sigma}(\mathbf{y})dS(\mathbf{y}) &= \int_{S_c}\tilde{t}_p^{\Sigma}(\mathbf{y})\int_{S_c}U_j^p(\boldsymbol{\xi}-\mathbf{y})t_j^{b\Sigma}(\boldsymbol{\xi})dS(\boldsymbol{\xi})dS(\mathbf{y}) \\ &+\int_{S_c}\tilde{t}_p^{\Sigma}(\mathbf{y})\int_{S_c}G_{mj}^p(\boldsymbol{\xi}-\mathbf{y})D_m u_j^{b\Delta}(\boldsymbol{\xi})dS(\boldsymbol{\xi})dS(\mathbf{y}) \\ &-\int_{S_c}\tilde{t}_p^{\Sigma}(\mathbf{y})\int_{S_c}H_{ij}^p(\boldsymbol{\xi}-\mathbf{y})n_i(\boldsymbol{\xi})u_j^{b\Delta}(\boldsymbol{\xi})dS(\boldsymbol{\xi})dS(\mathbf{y})\end{aligned} \tag{1}$$

$$\begin{aligned}-\frac{1}{2}\int_{S_c}\tilde{u}_k^{\Delta}(\mathbf{y})t_k^{b\Delta}(\mathbf{y})dS(\mathbf{y}) &= \int_{S_c}D_t\tilde{u}_k^{\Delta}(\mathbf{y})\int_{S_c}C_{mj}^{tk}(\boldsymbol{\xi}-\mathbf{y})D_m u_j^{b\Delta}(\boldsymbol{\xi})dS(\boldsymbol{\xi})dS(\mathbf{y}) \\ &+\int_{S_c}D_t\tilde{u}_k^{\Delta}(\mathbf{y})\int_{S_c}G_{tk}^j(\boldsymbol{\xi}-\mathbf{y})t_j^{b\Sigma}(\boldsymbol{\xi})dS(\boldsymbol{\xi})dS(\mathbf{y}) \\ &+\int_{S_c}\tilde{u}_k^{\Delta}(\mathbf{y})\int_{S_c}H_{lk}^j(\boldsymbol{\xi}-\mathbf{y})n_l(\mathbf{y})t_j^{b\Sigma}(\boldsymbol{\xi})dS(\boldsymbol{\xi})dS(\mathbf{y})\end{aligned} \tag{2}$$

where $S_c \equiv S_c^+$; $D_t(\cdot)=\varepsilon_{tmj}n_m\partial(\cdot)/\partial\xi_j$ is a surface differential operator with ε_{tmj} denoting the standard alternating symbol; $u_j^{b\Sigma}=u_j^{+b}+u_j^{-b}$ and $u_j^{b\Delta}=u_j^{+b}-u_j^{-b}$ are the sum and the jump of the displacement across the crack surface; $t_j^{b\Sigma}=t_j^{+b}+t_j^{-b}$ and $t_j^{b\Delta}=t_j^{+b}-t_j^{-b}$ are the sum and the jump of the traction across the crack surface; $\{\tilde{t}_p^{\Sigma},\tilde{u}_k^{\Delta}\}$ are sufficiently smooth test functions; and the singular kernels $\{U_j^p, G_{mj}^p, C_{mj}^{tk}, H_{ij}^p\}$ are defined for isotropic linearly elastic materials by,

$$U_j^p(\boldsymbol{\xi}-\mathbf{y})=\frac{1}{16\pi(1-\nu)\mu r}\left[(3-4\nu)\delta_{pj}+\frac{(\xi_p-y_p)(\xi_j-y_j)}{r^2}\right] \tag{3}$$

$$G_{mj}^p(\boldsymbol{\xi}-\mathbf{y})=\frac{1}{8\pi(1-\nu)r}\left[(1-2\nu)\varepsilon_{mpj}+\frac{(\xi_p-y_p)(\xi_a-y_a)}{r^2}\varepsilon_{ajm}\right] \tag{4}$$

$$C_{mj}^{tk}(\boldsymbol{\xi}-\mathbf{y})=\frac{\mu}{4\pi(1-\nu)r}\left[(1-\nu)\delta_{tk}\delta_{mj}+2\nu\delta_{km}\delta_{tj}-\delta_{kj}\delta_{tm}-\frac{(\xi_k-y_k)(\xi_j-y_j)}{r^2}\delta_{tm}\right] \tag{5}$$

$$H_{ij}^p(\boldsymbol{\xi}-\mathbf{y})=-\frac{(\xi_i-y_i)\delta_{jp}}{4\pi r^3} \tag{6}$$

where δ_{ij} is the Kronecker delta symbol and $r=\|\boldsymbol{\xi}-\mathbf{y}\|$. The boundary integral equations (1) and (2) are formulated in a weak form and contain only weakly singular kernels of $\mathcal{O}(1/r)$ and, in addition, involve only unknowns on the crack surface.

The behavior of the two zero-thickness layers is governed by the full version of Gurtin-Murdoch surface elasticity model, including the influence of both surface elasticity and residual surface tension. The equilibrium equations, surface constitutive relations, and strain-displacement relationship of the zero-thickness layers S_c^+ and S_c^- are of the same form and given by (see also [1, 2]),

$$\sigma^s_{i\beta,\beta} + t^s_i + t^0_i = 0 \tag{7}$$

$$\sigma^s_{\alpha\beta} = \tau^s \delta_{\alpha\beta} + \left(\lambda^s + \tau^s\right)\varepsilon^s_{\gamma\gamma}\delta_{\alpha\beta} + 2\left(\mu^s - \tau^s\right)\varepsilon^s_{\alpha\beta} + \tau^s u^s_{\alpha,\beta} \quad , \quad \sigma^s_{3\beta} = \tau^s u^s_{3,\beta} \tag{8}$$

$$\varepsilon^s_{\alpha\beta} = \tfrac{1}{2}\left(u^s_{\alpha,\beta} + u^s_{\beta,\alpha}\right) \tag{9}$$

where $\sigma^s_{i\beta}$, $\varepsilon^s_{\alpha\beta}$, u^s_i represent stress, strain and displacement components of each layer; $\mathbf{t}^0$ denotes prescribed traction on the top of each layer; and $\mathbf{t}^s$ denotes the unknown traction exerted on the interface of each layer by the bulk material. It is noted that the superscript "*s*" is utilized to emphasize that those quantities are associated with the two layers and Greek subscripts take the values 1, 2 (instead of 1, 2, and 3 as the Latin subscripts). The weak statement of (7)-(9) for both layers S_c^+ and S_c^- can readily be established following a standard procedure based on the weighted residual technique and the final results are given by (see also the development of weak statement for the special case of Gurtin-Murdoch model in the work of Nguyen et al. [24]),

$$\begin{aligned}
&\lambda^s \int_{S_c} \tilde{u}^{s\Sigma}_{\alpha,\alpha} u^{s\Sigma}_{\beta,\beta} dS + \frac{\mu^s}{2}\int_{S_c}\left(\tilde{u}^{s\Sigma}_{\alpha,\beta} + \tilde{u}^{s\Sigma}_{\beta,\alpha}\right)\left(u^{s\Sigma}_{\alpha,\beta} + u^{s\Sigma}_{\beta,\alpha}\right) dS + \tau^s \int_{S_c} \tilde{u}^{s\Sigma}_{3,\beta} u^{s\Sigma}_{3,\beta} dS \\
&-\left[\lambda^s \int_{\partial S_c} \tilde{u}^{s\Sigma}_{\alpha} n_\alpha u^{s\Sigma}_{\beta,\beta} d\Gamma + \frac{\mu^s}{2}\int_{\partial S_c}\left(\tilde{u}^{s\Sigma}_{\alpha} n_\beta + \tilde{u}^{s\Sigma}_{\beta} n_\alpha\right)\left(u^{s\Sigma}_{\alpha,\beta} + u^{s\Sigma}_{\beta,\alpha}\right) d\Gamma + \tau^s \int_{\partial S_c} \tilde{u}^{s\Sigma}_{3} n_\beta u^{s\Sigma}_{3,\beta} d\Gamma\right] \\
&\qquad\qquad -\int_{S_c} \tilde{u}^{s\Sigma}_i t^{s\Sigma}_i dS = \int_{S_c} \tilde{u}^{s\Sigma}_i t^{0\Sigma}_i dS
\end{aligned} \tag{10}$$

$$\begin{aligned}
&\lambda^s \int_{S_c} \tilde{u}^{s\Delta}_{\alpha,\alpha} u^{s\Delta}_{\beta,\beta} dS + \frac{\mu^s}{2}\int_{S_c}\left(\tilde{u}^{s\Delta}_{\alpha,\beta} + \tilde{u}^{s\Delta}_{\beta,\alpha}\right)\left(u^{s\Delta}_{\alpha,\beta} + u^{s\Delta}_{\beta,\alpha}\right) dS + \tau^s \int_{S_c} \tilde{u}^{s\Delta}_{3,\beta} u^{s\Delta}_{3,\beta} dS \\
&\qquad\qquad -\int_{S_c} \tilde{u}^{s\Delta}_i t^{s\Delta}_i dS = \int_{S_c} \tilde{u}^{s\Delta}_i t^{0\Delta}_i dS
\end{aligned} \tag{11}$$

where superscripts "Σ" and "Δ" indicate the sum and jump of quantities across the crack surfaces and $\tilde{u}^{s\Sigma}_\alpha$ and $\tilde{u}^{s\Delta}_\alpha$ are sufficiently smooth test functions. It is worth noting that the test function $\tilde{u}^{s\Delta}_\alpha$ satisfies the homogeneous condition on the boundary of the crack surface similar to the relative crack-face displacement $u^{s\Delta}_\alpha$, i.e., $\tilde{u}^{s\Delta}_\alpha = u^{s\Delta}_\alpha = 0$ on ∂S_c. By enforcing the continuity of the displacements and tractions along the interface of the two layers and the bulk material (i.e., $u^{s\Delta}_i = u^{b\Delta}_i \equiv u^{\Delta}_i$, $u^{s\Sigma}_i = u^{b\Sigma}_i \equiv u^{\Sigma}_i$, $t^{s\Delta}_i = -t^{b\Delta}_i \equiv -t^{\Delta}_i$, $t^{s\Sigma}_i = -t^{b\Sigma}_i \equiv -t^{\Sigma}_i$), the governing equations of the bulk material (1)-(2) and those of the surfaces (10)-(11) can be combined to obtain a final system of governing equations for the entire medium as,

$$\begin{aligned}
&\mathcal{A}(\tilde{\mathbf{u}}^{s\Sigma}, \mathbf{u}^{\Sigma}) + \mathcal{B}(\tilde{\mathbf{u}}^{s\Sigma}, \mathbf{t}^{\Sigma}) &&= \mathcal{R}_1(\tilde{\mathbf{u}}^{s\Sigma}) \\
&\mathcal{B}(\tilde{\mathbf{t}}^{\Sigma}, \mathbf{u}^{\Sigma}) + \mathcal{C}(\tilde{\mathbf{t}}^{\Sigma}, \mathbf{t}^{\Sigma}) + \mathcal{D}(\tilde{\mathbf{t}}^{\Sigma}, \mathbf{u}^{\Delta}) &&= 0 \\
&\qquad\quad \mathcal{D}(\mathbf{t}^{\Sigma}, \tilde{\mathbf{u}}^{\Delta}) + \mathcal{E}(\tilde{\mathbf{u}}^{\Delta}, \mathbf{u}^{\Delta}) &&= \mathcal{R}_2(\tilde{\mathbf{u}}^{\Delta})
\end{aligned} \tag{12}$$

where the bilinear integral operators $\mathcal{A}, \mathcal{B}, \mathcal{C}, \mathcal{D}$ and $\mathcal{E}$ are defined by,

$$\mathscr{A}(\mathbf{X},\mathbf{Y})=\frac{\lambda^s}{2}\int_{S_c} X_{\alpha,\alpha}Y_{\beta,\beta}dS+\frac{\mu^s}{4}\int_{S_c}\left(X_{\alpha,\beta}+X_{\beta,\alpha}\right)\left(Y_{\alpha,\beta}+Y_{\beta,\alpha}\right)dS+\frac{\tau^s}{2}\int_{S_c} X_{3,\beta}Y_{3,\beta}dS$$
$$-\left[\frac{\lambda^s}{2}\int_{\partial S_c} X_\alpha n_\alpha Y_{\beta,\beta}d\Gamma+\frac{\mu^s}{4}\int_{\partial S_c}\left(X_\alpha n_\beta+X_\beta n_\alpha\right)\left(Y_{\alpha,\beta}+Y_{\beta,\alpha}\right)d\Gamma+\frac{\tau^s}{2}\int_{\partial S_c} X_3 n_\beta Y_{3,\beta}d\Gamma\right] \tag{13}$$

$$\mathscr{B}(\mathbf{X},\mathbf{Y})=\frac{1}{2}\int_{S_c} X_p Y_p dS \tag{14}$$

$$\mathscr{C}(\mathbf{X},\mathbf{Y})=-\int_{S_c} X_p(\mathbf{y})\int_{S_c} U_j^p(\boldsymbol{\xi}-\mathbf{y})Y_j(\boldsymbol{\xi})dS(\boldsymbol{\xi})dS(\mathbf{y}) \tag{15}$$

$$\mathscr{D}(\mathbf{X},\mathbf{Y})=-\int_{S_c} X_p(\mathbf{y})\int_{S_c} G_{mj}^p(\boldsymbol{\xi}-\mathbf{y})D_m Y_j(\boldsymbol{\xi})dS(\boldsymbol{\xi})dS(\mathbf{y})$$
$$+\int_{S_c} X_p(\mathbf{y})\int_{S_c} H_{ij}^p(\boldsymbol{\xi}-\mathbf{y})n_i(\boldsymbol{\xi})Y_j(\boldsymbol{\xi})dS(\boldsymbol{\xi})dS(\mathbf{y}) \tag{16}$$

$$\mathscr{E}(\mathbf{X},\mathbf{Y})=-\int_{S_c} D_t X_k(\mathbf{y})\int_{S_c} C_{mj}^{tk}(\boldsymbol{\xi}-\mathbf{y})D_m Y_j(\boldsymbol{\xi})dS(\boldsymbol{\xi})dS(\mathbf{y})+\mathscr{F}(\mathbf{X},\mathbf{Y}) \tag{17}$$

$$\mathscr{F}(\mathbf{X},\mathbf{Y})=\frac{\lambda^s}{2}\int_{S_c} X_{\alpha,\alpha}Y_{\beta,\beta}dS+\frac{\mu^s}{4}\int_{S_c}\left(X_{\alpha,\beta}+X_{\beta,\alpha}\right)\left(Y_{\alpha,\beta}+Y_{\beta,\alpha}\right)dS+\frac{\tau^s}{2}\int_{S_c} X_{3,\beta}Y_{3,\beta}dS \tag{18}$$

and the linear integral operators $\mathscr{R}_1$ and $\mathscr{R}_2$ are defined, in terms of the prescribed traction data $\mathbf{t}^{0\Sigma}$ and $\mathbf{t}^{0\Delta}$, by,

$$\mathscr{R}_1(\mathbf{X})=\frac{1}{2}\int_{S_c} X_l t_l^{0\Sigma}dS \tag{19}$$

$$\mathscr{R}_2(\mathbf{X})=\frac{1}{2}\int_{S_c} X_l t_l^{0\Delta}dS \tag{20}$$

It is remarked in particular that the last equation of (12) is obtained by combining equations (2) and (11), along with choosing the test functions satisfying $\tilde{u}_i^{s\Delta}=\tilde{u}_i^{\Delta}$.

Numerical Implementation

Standard procedures for the weakly singular SGBEM (e.g., [25-27, 29]) and for the standard finite element method (e.g., [31-33]) are employed to form the discretized system of linear algebraic equations of (12). Since all involved boundary integrals in the governing equation of the bulk material contain only weakly singular kernels of $\mathscr{O}(1/r)$, standard C^0 interpolation functions are utilized everywhere in the approximation of both trial and test functions.

The construction of the coefficient matrix of the discretized system requires the numerical integration of two different types of integrals viz. the single and double surface integrals. The former which contains the regular and well-behaved integrand can be integrated accurately and efficiently by standard, low-order Gaussian quadrature, whereas the numerical integration of the latter type (appearing in the boundary integral equations for the bulk material) is more challenging, depending primarily on the behavior of the integrand. Due to the presence of the singular kernels $\{U_j^p, G_{mj}^p, C_{mj}^{tk}, H_{ij}^p n_i\}$, the integrand

becomes weakly singular, nearly singular, and regular when two elements involved in the double surface integral are identical, relatively close, and sufficiently remote, respectively. The transformation technique and integration rule proposed by Xiao [34] and Li and Han [35] are utilized to treat such double surface integrals. Once the system of linear algebraic equations is solved by a selected efficient linear solver, all the primary unknowns on the crack surface i.e., $\{u_i^{\Delta}, u_i^{\Sigma}, t_i^{\Sigma}\}$ are obtained and other quantities within the bulk material (e.g., the displacements and stresses) can then be obtained by using integral relations proposed by Rungamornrat and Mear [28].

Results and Discussions

In this section, results for a penny-shaped crack embedded in an infinite medium are first presented, to verify both the formulation and the numerical implementation of the proposed technique with available benchmark solutions. Then, an elliptical crack embedded in an unbounded domain is further investigated, to demonstrate the capability of the proposed numerical technique.

In the analysis, three different levels of mesh refinement are adopted to examine the convergence of numerical results. Nine-node isoparametric elements are used to discretize the entire crack front, whereas the rest of the crack surface is discretized by eight-node and six-node isoparametric elements. Young's modulus and Poisson's ratio for the bulk material are taken as $E = 107\ GPa$ and $\nu = 0.33$, respectively, and the surface elastic constants and the residual surface tension are chosen identical to those utilized by [22, 23] (i.e., $\lambda^s = 4.4939\ N/m$, $\mu^s = 2.7779\ N/m$, $\tau^s = 0.6056\ N/m$). For convenience in the numerical analysis, all quantities involved in the key governing equation are properly normalized. For instance, the unknown sum of the traction and the prescribed traction on the top surface of the two-thickness layers are normalized by the shear modulus μ (i.e., $t_0^{\Sigma} = t^{\Sigma}/\mu$ and $\sigma_{i0} = \sigma_i^0/\mu$); the unknown sum and jump of the relative crack-face displacement are normalized by a special length scale $\Lambda = \kappa^s/\mu = 0.24983\ nm$ (i.e., $u_0^{\Delta} = u^{\Delta}/\Lambda$ and $u_0^{\Sigma} = u^{\Sigma}/\Lambda$) where $\kappa^s = \left|\lambda^s + 2\mu^s\right|$; and all characteristic lengths representing the geometry of the crack such as the crack radius *a*, the semi-major axis *a*, and the semi-minor axis *b* used in following examples are normalized by the length scale Λ (e.g., $a_0 = a/\Lambda$ and $b_0 = b/\Lambda$).

Penny-shaped Crack in an Elastic Infinite Medium

In order to verify the proposed numerical technique, the problem of a penny-shaped crack of radius *a* embedded in a homogeneous, isotropic, linearly elastic infinite medium (see Figure 2(a)) is investigated. The crack is subjected to self-equilibrated, uniformly distributed traction σ^0 normal to its surface. This boundary value problem was previously studied by Intarit et al. [22] and Intarit [23] using Hankel integral transforms along with a solution technique for the dual integral equations, and their results are taken as the benchmark solutions.

The normalized crack opening displacement and vertical stress in the vicinity of the crack front obtained from the proposed numerical technique for the three meshes shown in Figure 2(b) are presented in Figure 3 along with the benchmark solution generated by [22, 23]. It is seen that the numerical results are slightly mesh dependent and that they are highly accurate and almost indistinguishable from the analytical solution. It can also be pointed out from the results shown in Figure 3 that the two models incorporating the surface stresses with and without the influence of in-plane surface elasticity yield results

significantly different from those predicted by the classical model (i.e., without the surface stress effects). While both the residual surface tension and the in-plane surface elasticity contribute to such discrepancy, the influence of the residual surface tension seems more significant. Similar to previous findings (e.g., [9, 22]), the medium tends to be much stiffer than the classical case, when the full version of the surface stress model is considered in the analysis.

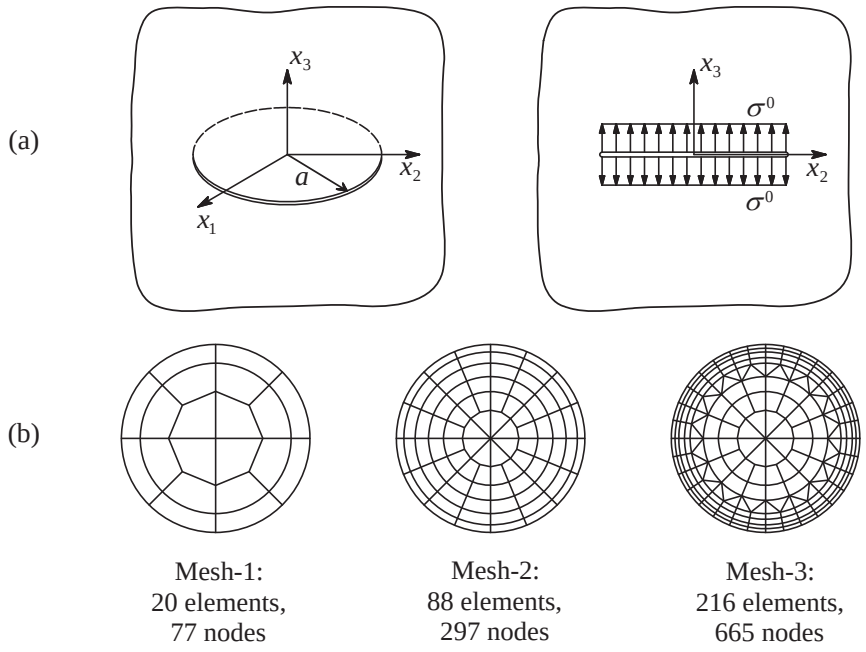

Figure 2: (a) Schematic of a penny-shaped crack of radius a embedded in a three-dimensional, isotropic, linear elastic infinite medium under self-equilibrated, uniformly distributed, normal traction and (b) three meshes adopted in the analysis.

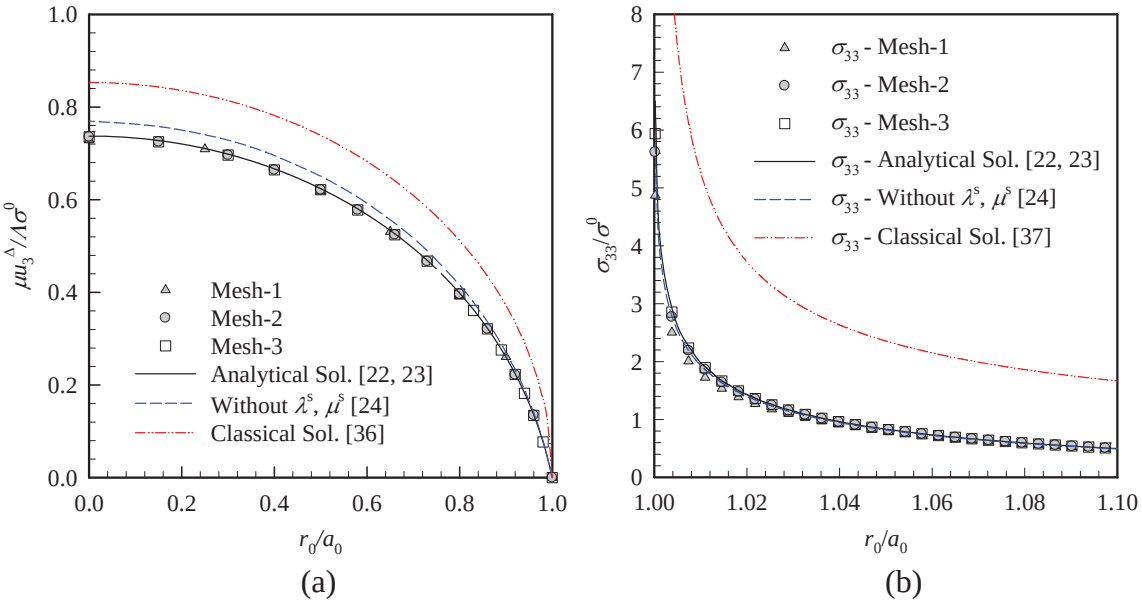

Figure 3: Results for penny-shaped crack under uniformly distributed normal traction; (a) normalized crack opening displacement and (b) normalized vertical stress along the x_1-axis where $r_0 = x_1/\Lambda$.

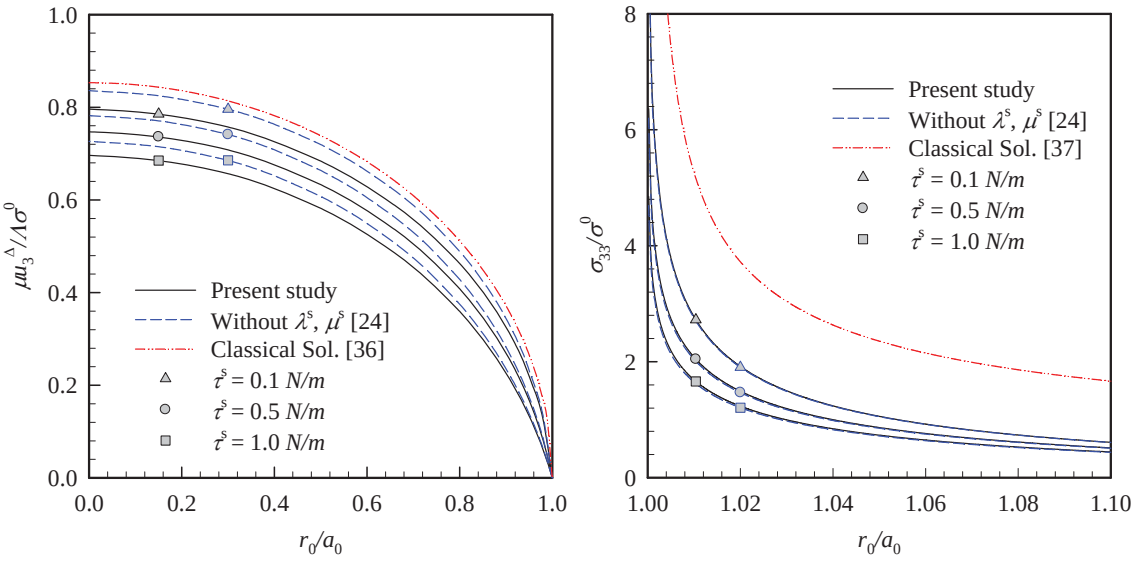

(a) (b)

Figure 4: Results for penny-shaped crack under uniformly distributed normal traction for different residual surface tension τ^s varied from 0 to 1 N/m and $E = 107\ GPa$, $\nu = 0.33$, $\lambda^s = 4.4939\ N/m$, $\mu^s = 2.7779\ N/m$; (a) normalized crack opening displacement and (b) normalized vertical stress along the x_1-axis where $r_0 = x_1/\Lambda$.

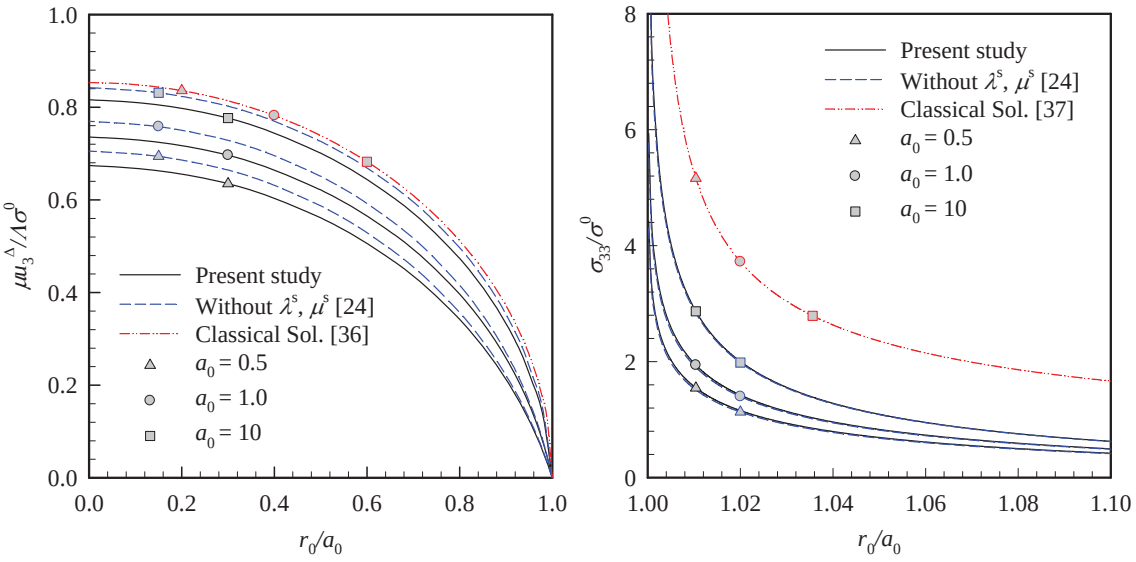

(a) (b)

Figure 5: Results for penny-shaped crack under uniformly distributed normal traction for different crack radii $a_0 \in \{0.5, 1.0, 10.0\}$ and $E = 107\ GPa$, $\nu = 0.33$, $\lambda^s = 4.4939\ N/m$, $\mu^s = 2.7779\ N/m$, $\tau^s = 0.6056\ N/m$; (a) normalized crack opening displacement and (b) normalized vertical stress along the x_1-axis where $r_0 = x_1/\Lambda$.

To further examine the influence of residual surface tension on the normalized crack opening displacement and vertical stress in the vicinity of the crack front when the surface elasticity is included, results are presented in Figure 4 for various values of the residual

surface tension τ^s ranging from 0 to 1.0 *N/m* with the surface elastic constants remaining fixed. It is evident that the residual surface tension exhibits significant influence on both the crack opening displacement and the vertical stress in the vicinity of the crack front. As τ^s becomes larger, the deviation of results from the classical case (i.e., without the surface stresses) increases significantly.

To demonstrate the size-dependent behavior of results due to the presence of surface stresses, the normalized crack opening displacement and vertical stress in the vicinity of the crack front obtained from three different models (i.e., the classical model without the surface stresses, the model incorporating only the residual surface tension [24], and the current model) are shown in Figure 5 for three different crack radii $a_0 = a/\Lambda \in \{0.5, 1.0, 10.0\}$. It is evident from this particular set of results that solutions predicted by the two models including surface stresses clearly exhibit size-dependent behavior, whereas those predicted by the classical model are size-independent. Furthermore, as the crack radius decreases, the influence of surface stresses is more significant, especially when the surface elastic constants are included.

In addition, the incorporation of in-plane surface elasticity further reduces the crack opening displacement (see Figure 4(a) and Figure 5(a)). However, the existence of such surface elastic constants does not significantly influence the vertical stress in the vicinity of the crack front. The discrepancy of predicted vertical stress in the vicinity of the crack front from the two models with and without the surface elastic constants is barely recognizable (see Figure 4(b) and Figure 5(b)).

Elliptical Crack in an Elastic Infinite Medium

To demonstrate the capability of the proposed numerical technique of treating cracks of arbitrary shape, an elliptical crack embedded in an isotropic, linear elastic unbounded domain is considered (see Figure 6(a)). The crack front is parameterized in terms of a parameter *t* by,

$$x_1 = a\cos t, \quad x_2 = b\sin t, \quad x_3 = 0; \quad t \in [0, 2\pi] \tag{21}$$

where *a* and *b* denote the major and minor semi-axes of the crack, respectively. The crack is subjected to a self-equilibrated, uniformly distributed normal traction σ^0. Numerical results are presented for three different aspect ratios $a/b \in \{1, 2, 3\}$ and three meshes shown in Figure 6(b) are adopted in the numerical study.

The normalized crack opening displacement and vertical stress along the minor axis, with the influence of the surface stresses, are presented in Figure 7 for all three aspect ratios considered. It can be seen from results in Figure 7, that when the aspect ratio a/b increases, the influence of the surface stresses on the crack opening displacement and the near-tip vertical stresses decreases. To further examine the size-dependent behavior of results due to the presence of the surface stresses, the crack opening displacement and the vertical stress in the vicinity of the crack front for $b_0 = b/\Lambda \in \{0.5, 1.0, 10.0\}$ and for the aspect ratio $a/b = 2$ are shown in Figure 8. It can be observed from these results that the normalized crack opening displacement and the vertical stress in the vicinity of the crack front are apparently size-dependent. This is in contrast to the classical model (i.e., without the surface stresses) whose predicted solutions are size-independent. When the crack-size decreases, the influence of surface stresses becomes significant; in particular, it renders the medium much stiffer. Additionally, in agreement with the previous example, it can also be

observed that in-plane surface elasticity further reduced the crack opening displacement. However, it has negligible influence on the vertical stress in the vicinity of the crack front.

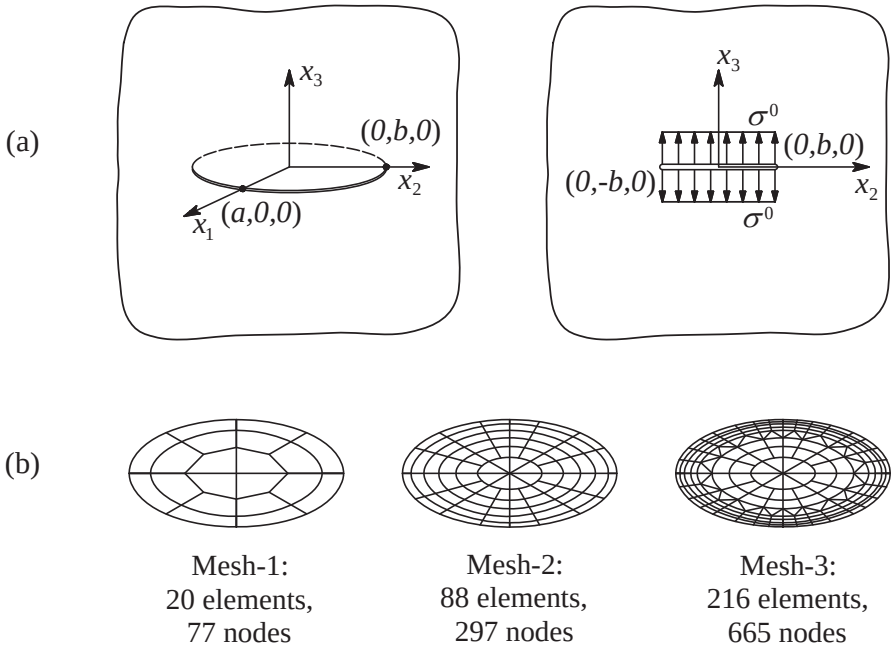

Figure 6: (a) Schematic of an elliptical crack embedded in a three-dimensional, isotropic, linear elastic infinite medium under self-equilibrated, uniformly distributed, normal traction and (b) three meshes adopted in the analysis.

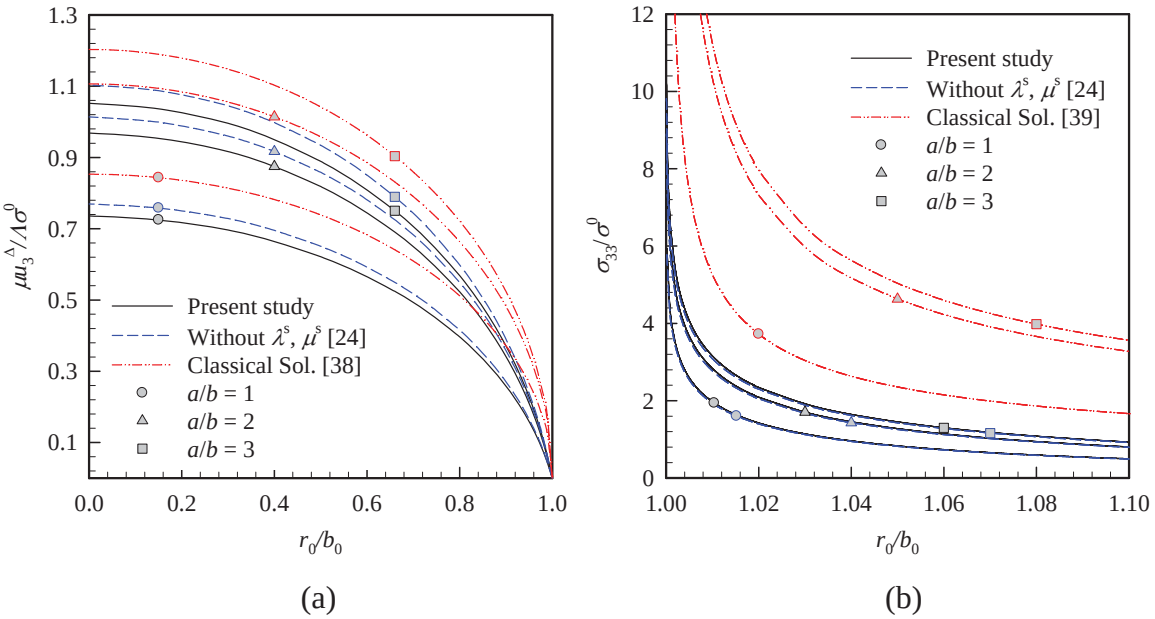

Figure 7: Results for elliptical crack under uniformly distributed normal traction and for different aspect ratios $a/b \in \{1, 2, 3\}$; (a) normalized crack opening displacement along the minor axis and (b) normalized vertical stress in the vicinity of the crack front along the minor axis.

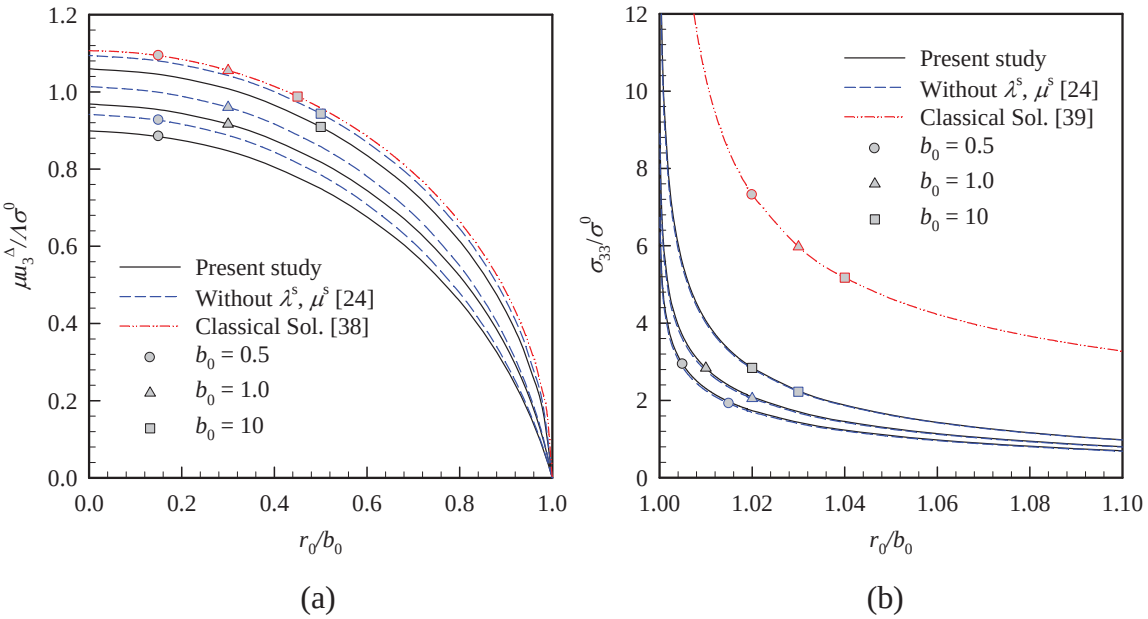

(a) (b)

Figure 8: Results for elliptical crack under uniformly distributed normal traction for different crack radii $b_0 \in \{0.5, 1.0, 10.0\}$ and $a/b = 2$; (a) normalized crack opening displacement along the minor axis and (b) normalized vertical stress in the vicinity of the crack front along the minor axis.

Conclusions

A numerical technique capable of modeling planar cracks in three-dimensional, linear elastic media including the surface stress effect has been established. The governing equations have been formulated using the classical theory of isotropic linear elasticity for the bulk medium and the full version of the Gurtin-Murdoch surface elasticity model for the infinitesimally thin layers on the crack surfaces. The full coupled system of governing equations has been solved numerically by using the FEM-SGBEM coupling procedure. The numerical results for a penny-shaped crack problem have been benchmarked with the available analytical solution, to verify the formulation and the proposed FEM-SGBEM technique. Results for an elliptical crack have also been investigated, to demonstrate the capability of the proposed computational procedure to treat cracks of arbitrary shape. The numerical technique developed in the present study has been found computationally promising and capable of modeling planar nano-sized cracks with arbitrary shape. Although results are presented only for the single crack problem for the sake of brevity, the formulation and implementation are definitely applicable to problems of multiple cracks. From an extensive numerical study, the significant role of surface stresses and the size-dependent behavior of the predicted solutions are confirmed. In particular, a model including both in-plane elasticity of the surface and residual surface tension, significantly increases the near-surface material stiffness and predicts a much lower crack opening displacement and near-tip vertical stress, in comparison with the classical solution.

Acknowledgements

Financial support from JICA AUN/SEED-Net Scholarship and Thailand Research Fund (Grant No. MRG5380159 and Grant No. BRG5480006) are gratefully acknowledged.

References:

[1] M.E. Gurtin and A.I. Murdoch, "A continuum theory of elastic material surfaces", *Archive for Rational Mechanics and Analysis*, 57(4):291-323, 1975.

[2] M.E. Gurtin and A.I. Murdoch, "Surface stress in solids", *International Journal of Solids and Structures*, 14(6):431-440, 1978.

[3] L.H. He, C.W. Lim and B.S. Wu, "A continuum model for size-dependent deformation of elastic films of nano-scale thickness", *International Journal of Solids and Structures*, 41(3-4): 847-857, 2004.

[4] R. Dingreville, J. Qu and M. Cherkaoui, "Surface free energy and its effect on the elastic behavior of nano-sized particles, wires and films", *Journal of the Mechanics and Physics of Solids*, 53(8):1827-1854, 2005.

[5] D.W. Huang, "Size-dependent response of ultra-thin films with surface effects", *International Journal of Solids and Structures*, 45(2):568-579, 2008.

[6] L. Tian, and R.K.N.D. Rajapakse, "Finite element modeling of nanoscale inhomogeneities in an elastic matrix", *Computational Materials Science*, 41(1):44-53, 2007.

[7] L. Tian, and R.K.N.D. Rajapakse, "Analytical Solution for Size-Dependent Elastic Field of a Nanoscale Circular Inhomogeneity", *ASME Journal of Applied Mechanics*, 74(3):568-574, 2007.

[8] L. Tian, and R.K.N.D. Rajapakse, "Elastic field of an isotropic matrix with a nanoscale elliptical inhomogeneity", *International Journal of Solids and Structures*, 44(24):7988-8005, 2007.

[9] Y. Pinyochotiwong, J. Rungamornrat, T. Senjuntichai, "Rigid frictionless indentation on elastic half space with influence of surface stresses", *International Journal of Engineering Science*, 71(0): 15-35, 2013.

[10] R.E. Miller and V.B. Shenoy, "Size-dependent elastic properties of nanosized structural elements", *Nanotechnology*, 11(3): 139-147, 2000.

[11] V.B. Shenoy, "Size-dependent rigidities of nanosized torsional elements", *International Journal of Solids and Structures*, 39(15): 4039-4052, 2002.

[12] G.F. Wang, X.Q. Feng, T.J. Wang and W. Gao, "Surface Effects on the Near-Tip Stresses for Mode-I and Mode-III Cracks", *ASME Journal of Applied Mechanics*, 75(1):011001-011005, 2008.

[13] X.L. Fu, G.F. Wang and X.Q. Feng, "Surface effects on the near-tip stress fields of a mode-II crack", *International Journal of Fracture*, 151(2):95-106, 2008.

[14] X.L. Fu, G.F. Wang and X.Q. Feng, "Surface effects on mode-I crack tip fields: A numerical study", *Engineering Fracture Mechanics*, 77(7):1048-1057, 2010.

[15] Q.H. Fang, Y.Liu, Y.W. Liu and B.Y. Huang, "Dislocation emission from an elliptically blunted crack tip with surface effects", *Physica B: Condensed Matter*, 404(20):3421-3424, 2009.

[16] G.F. Wang, and Y. Li, "Influence of surface tension on mode-I crack tip field", *Engineering Fracture Mechanics*, 109(0): 290-301, 2013.

[17] C.I. Kim, P. Schiavone and C.Q. Ru, "Analysis of a mode-III crack in the presence of surface elasticity and a prescribed non-uniform surface traction", *Zeitschrift für angewandte Mathematik und Physik*, 61(3):555-564, 2010.

[18] C.I. Kim, P. Schiavone and C.Q. Ru, "The effect of surface elasticity on a Mode-III interface crack", *Archives of Mechanics*, 63(3):267-286, 2011.

[19] C.I. Kim, P. Schiavone and C.Q. Ru, "Analysis of Plane-Strain Crack Problems (Mode-I & Mode-II) in the Presence of Surface Elasticity", *Journal of Elasticity*, 104(1):397-420, 2011.

[20] H. Nan, and B. Wang, “Effect of residual surface stress on the fracture of nanoscale materials”, *Mechanics Research Communications*, 44(0):30-34, 2012.
[21] H.S. Nan and B.L. Wang, “Effect of crack face residual surface stress on nanoscale fracture of piezoelectric materials”, *Engineering Fracture Mechanics*, 110(0): 68-80, 2013.
[22] P. Intarit, T. Senjuntichai, J. Rungamornrat and R.K.N.D. Rajapakse, “Stress analysis of penny-shaped crack considering the effects of surface elasticity”, Proceedings of 20th Annual International Conference on Composites or Nano Engineering (ICCE-20), Ramada Beijing North Hotel, Beijing, P.R. China, 2012.
[23] P. Intarit. *Solutions of elastic medium with surface stress effects*. Dissertation (PhD), Chulalongkorn University, Thailand, 2013.
[24] T.B. Nguyen, J. Rungamornrat, T. Senjuntichai and A. C. Wijeyewickrema, “FEM-SGBEM coupling for modeling of mode-I planar cracks in three-dimensional elastic media with residual surface tension effects”, *Engineering Analysis with Boundary Elements (under review)*, 2013.
[25] S. Li, M.E. Mear, “Singularity-reduced integral equations for displacement discontinuities in three-dimensional linear elastic media”, *International Journal of Fracture*, 93: 87-114, 1998.
[26] S. Li, M.E. Mear and L. Xiao, “Symmetric weak-form integral equation method for three-dimensional fracture analysis”, *Computer Methods in Applied Mechanics and Engineering*, 151: 435-459, 1998.
[27] J. Rungamornrat, “Analysis of 3D cracks in anisotropic multi-material domain with weakly singular SGBEM”, *Engineering Analysis with Boundary Elements*, 30 (10): 834-846, 2006.
[28] J. Rungamornrat, and M. E. Mear, “Weakly-singular, weak-form integral equations for cracks in three-dimensional anisotropic media”, *International Journal of Solids and Structures*, 45(5):1283-1301, 2008.
[29] J. Rungamornrat and M. E. Mear, “A weakly-singular SGBEM for analysis of cracks in 3D anisotropic media”, *Computer Methods in Applied Mechanics and Engineering*, 197:4319-4332, 2008.
[30] J. Rungamornrat and T. Senjuntichai, “Regularized boundary integral representations for dislocations and cracks in smart media”, *Smart Materials and Structures*, 18:074010 (14pp), 2009.
[31] K.J. Bathe, *Finite Element Procedures*, Prentice-Hall, New Jersey, 1990.
[32] T.J.R. Hughes, *The finite element method: linear static and dynamic finite element analysis*, Dover Publications, New Jersey, 2000.
[33] O.C. Zienkiewicz and R.L. Taylor, *The finite element method: Solid mechanics*, volume 2, Butterworth-Heinemann, Oxford, 2000.
[34] L. Xiao. *Symmetric weak-form integral equation method for three-dimensional fracture analysis*, Dissertation (PhD), The University of Texas at Austin, Texas, 1998.
[35] H.B. Li, and G.M. Han, “A new method for evaluating singular integral in stress analysis of solids by the direct boundary element method”, *International Journal for Numerical Methods in Engineering*, 21: 2071-2098, 1985.
[36] H. Tada, P.C. Paris and G.R. Irwin, *The Stress Analysis of Cracks Handbook*, American Society of Mechanical Engineers, 2000.
[37] M.K. Kassir, G.C. Sih, *Three-dimensional Crack Problems: A New Selection of Crack Solutions in Three-dimensional Elasticity*, vol. 2, Noordhoff International Publishing, Leyden, 1975.

[38] C. Zeng-shen, Discussion on the SIF for points on border of elliptical flat crack inside infinite solid under uniform tension, *Applied Mathematics and Mechanics*, 3(4): 521-526, 1982.
[39] A.E. Green, I.N. Sneddon, The distribution of stress in the neighborhood of a flat elliptical crack in an elastic solid, *Mathematical Proceedings of the Cambridge Philosophical Society*, 46(1):159–163, 1950.

Elastic Layer under Axisymmetric Surface Loads and Influence of Surface Stresses

P. Tuttipongsawat[a], J. Rungamornrat[a,*], T. Senjuntichai[a]

[a]Department of Civil Engineering, Faculty of Engineering, Chulalongkorn University Bangkok, Thailand 10330

(Submitted to *Applied Mathematical Modeling*)

ABSTRACT

This paper presents the analysis of an infinite, rigid based elastic layer under the action of axisymmetric surface loads by taking the surface energy effects into account. The corresponding boundary value problems for the bulk and the surface are formulated based on a classical theory of linear elasticity and a complete Gurtin-Murdoch constitutive relation. An analytical technique using Love's representation and Hankel integral transform is adopted to derive an explicit integral-form solution for both the displacement and stress fields. A selected numerical quadrature is subsequently applied to efficiently evaluate all involved integrals. After conducting an extensive parametric study, the surface stresses show strong influence on responses in the region relatively close to the surface and also when a length scale of the problem is comparable to the intrinsic length of the surface. Such influence is more evident when the contribution of the residual surface tension is taken into account. Results for general axisymmetric surface loads are then used to derive fundamental solutions for a unit normal concentrated load, a unit normal ring load and a unit tangential ring load. Such basic results constitute the essential basis for the development of boundary integral equations governing other related problems such as contact and nano-indentation problems.

***Keywords*:** Elastic layer, Gurtin-Murdoch model, Hankel integral transform, Nano-scale influence, Surface stresses

1. INTRODUCTION

Nowadays, nanotechnology gains remarkable recognition in various disciplines including biology, chemistry, physics, medicines, material sciences, and also engineering. This is due to the fact that materials in the nano-scale level exhibit desirable physical, mechanical, and other crucial properties very different from those of a larger scale and this, therefore, enables their unique applications in various fields. For instance, nano-crystals are employed in household lightings to convert electricity into light instead of wasting away into heat; a newly

* Corresponding author, Associate Professor, Tel.: +1 66 2218 6460, E-mail address: Jaroon.r@chula.ac.th

invented device, called nano-shell, is used in the medical applications to destroy a tumor after activated by a laser beam without any harm to contiguous cells; and nano-crystalline silicon carbide is found in the hard protective coatings of cutting tools and computer hard disks. To aid the optimal design and development of those newly invented, nano-scale devices, advanced material researches related to nano-scale and nano-structured materials are essential for profoundly understanding their fundamental properties and behaviors.

Various sophisticated techniques and physically suitable mathematical models have been proposed continuously, in the past three decades, to investigate the behavior and properties of nano-scale and nano-structured materials. Experimental methods have been widely employed in the characterization of mechanical properties of materials in nano-scale due to their advantages of perceiving the actual behavior. For instance, Wong et al. [1] utilized an atomic-force microscope to determine the mechanical properties of isolated silicon carbide nano-rods (SiC-NRs) and multi-wall carbon nano-tubes (MWNTs); Mao et al. [2] also employed the atomic-force microscope to investigate the hardness of both ZnO and SnO_2 nano-belts; and Poncharal et al. [3] statically and dynamically measured the bending modulus of carbon nano-tubes in a transmission electron microscope. Although experimental investigations have boosted significant progress in the area, obtained results and findings are, in general, highly dependent on testing conditions and, in addition, sophisticated testing devices and high-precision testing procedures are required.

Due to the significant breakthrough of numerical analysis and computational devices, mathematical modeling and simulations have become an attractive candidate and been widely used in the study of nano-scale problems. Once integrating essential inherent features via selected governing physics and properly calibrated with data from basic experiments, mathematical models have been found capable of simulating responses under various conditions and yielding sufficiently accurate results (e.g., [4-13]). Among existing techniques, the molecular dynamics or atomistic calculations are robust and generally yield highly accurate response prediction (e.g. [6, 7, 10-11]). However, those techniques still possess a major drawback associated with the requirement of tremendous computational resources in the solution procedure. As a result, continuum-based models enhanced by incorporating the nano-scale influence have been increasingly proposed due to their simplified governing physics and computational efficiency (e.g., [4, 8-9, 12-13]).

Resulting from atomistic simulations, it was discovered that the energy at the free surface is generally different from that of atoms in the bulk material (e.g., [5]). The intrinsic

length scale, which is defined as the ratio of surface free energy and Young's modulus is an inevitable material parameter [14] because it becomes comparable to the characteristic length of the material at a nano-scale. For this particular situation, the surface free energy plays an important role on the properties of materials and they, therefore, become size-dependent (e.g., [4]). As a result, the effect of surface stresses should be integrated into the classical continuum models to be capable of capturing the mechanical behavior of nano-scale materials. The concepts of surface energy and surface stress were originally introduced by Gibbs [15]. Gibbsian thermodynamics, one of the most useful tools for studying various surface phenomena, can be found in several studies of surface stresses (e.g., [16-18]). Gurtin-Murdoch's surface elasticity model, one that incorporates the influence of the surface free energy into the classical continuum-based theory, proposed by Gurtin and his co-workers [19-21] has been extensively employed. The surface, which has its own constitutive law, is assumed to be very thin and modeled as a mathematical layer with zero thickness and perfectly bonded to the bulk. Material parameters contained in the constitutive relation were generally obtained from atomistic simulation is utilized [7, 22].

The validity of the Gurtin-Murdoch model has been extensively examined and verified in various investigations (e.g., [5, 7, 22-23]). For instance, Miller and Shenoy [22] and Shenoy [23] applied the Gurtin-Murdoch constitutive relation to investigate the behavior of nano-scale bars, beams and plates under uniaxial tension, bending, and torsion. Results from their study were compared with those from atomistic simulations and good agreement among those results was concluded. Dingreville et al. [5] studied the size-dependency of elastic properties of nano-sized particles, wires, and films by using an analytical technique. The effective Young's modulus of thin films of various thicknesses in their analytical study was found in excellent agreement with results generated by molecular static (MS) simulations. Moreover, they also pointed out that their proposed formulation was much more computationally efficient than the MS simulations. According to the accuracy of predicted responses and computational efficiency of related solution procedures, Gurtin-Murdoch continuum-based model has gained significant popularity and been widely used in the study of nano-scale problems such as ultra-thin elastic films [24-25], nano-inclusions [26-27], nano-scale inhomogeneities [8-9], and nano-scale indentations [13, 28].

Problems of surface loadings and contacts are considered fundamental in nano-mechanics and have a wide range of applications including the investigation of mechanical properties such as hardness and elastic modulus. Work towards the modeling of near-surface

fields under different surface loading conditions by using enhanced continuum-based models to characterize the surface energy effects has started gaining attention from various researchers in the past two decades since it offers computationally efficient techniques capable of reasonably predicting the behavior of materials at a nano-scale level. For instance, Wang and Feng [29] studied the responses of an elastic half-plane subjected to surface pressure by considering the influence of a constant residual surface tension but ignoring the surface elastic constants. Huang and Yu [30] extended the work of Wang and Feng [29] by incorporating the surface elastic constants. Recently, Zhao and Rajapakse [31] studied the near-surface responses and size dependency of a two-dimensional and an axisymmetric three-dimensional infinite elastic layers under surface loads by using Fourier and Hankel integral transform techniques. It should be emphasized, however, that the Gurtin-Murdoch model used in their study was still incomplete since the out-of-plane contribution of the residual surface tension was ignored in their formulation. Intarit et al. [32] studied the effect of surface stresses on the near-surface responses of semi-infinite dislocations and buried loads in an elastic half-plane. Again, the contribution of out-of-plane terms was still not considered. Most recently, Intarit et al. [33] generalized the work of Intarit et al. [32] by integrating the influence of the residual surface tension in addition to the surface elastic constants to model a two-dimensional elastic layer under buried loading conditions.

On the basis of an extensive literature survey, the study of near-surface responses of a three-dimensional elastic layer using a complete version of Gurtin-Murdoch model has not been well recognized. In particular, an analytical solution of a three-dimensional elastic layer subjected to arbitrary axisymmetric surface loads by incorporating both in-plane and out-of-plane contribution of surface stresses is still not available in the literature and is the main focus of the present study. Results from this fundamental problem should not only shed some light on the nano-scale influence but also be potentially useful in the investigation of more complex boundary value problems such as nano-indentations.

2. PROBLEM FORMULATION

This section begins with the clear description and essential assumptions of the boundary value problem considered in the present study. All basic field equations for the bulk material and the surface are then briefly summarized. A solution technique to determine the general solution of elastic fields within the bulk is also outlined with the final results. Finally, the boundary conditions derived from the surface equations are enforced to determine a complete

solution of the given boundary value problem.

2.1 Problem Description

Consider a three-dimensional, infinite, elastic layer of constant thickness *h* subjected to arbitrary axisymmetric surface loads with its base fully restrained against the movement as shown schematically in Fig. 1. The reference cylindrical coordinate system is chosen such that the origin is located at the free surface and the positive *z*-axis directs downward whereas other axes follow the standard right-hand rule. The entire domain is treated as a body consisting of two different parts, the bulk material occupying a three-dimensional region defined by $0 < z \leq h$ and the zero-thickness layer occupying the plane $z = 0$ and perfectly bonded to the bulk material. The former is made of a homogeneous, isotropic, linear elastic material with Lamé constants $\{\mu, \lambda\}$ whereas the latter possesses the surface Lamé constants $\{\mu^s, \lambda^s\}$ and the residual surface tension τ^s. The normal and tangential loads acting on the surface (i.e., the top side of the zero-thickness layer) are denoted by $p = p(r)$ and $q = q(r)$, respectively. In the presence study, the bulk part is assumed to be free of the body force and remote loadings. For brevity, in what follows, the term "*surface*" is utilized throughout to signify the zero-thickness layer unless stated otherwise. The statement of the problem is to determine the complete elastic fields (e.g., the displacement and stress fields) within the bulk due to the arbitrary (axisymmetric) applied surface loads $p(r)$ and $q(r)$ and the influence of surface stresses.

2.2 Basic Equations

Basic field equations for the bulk follow directly the classical theory of isotropic, linear elasticity [34, 35]. In the absence of the body force and under axisymmetric deformation, equilibrium equations, constitutive laws, and strain-displacement relations (referring to the cylindrical coordinate system) are given by

$$\frac{\partial \sigma_{rr}}{\partial r} + \frac{\partial \sigma_{rz}}{\partial z} + \frac{\sigma_{rr} - \sigma_{\theta\theta}}{r} = 0\ , \quad \frac{\partial \sigma_{rz}}{\partial r} + \frac{\partial \sigma_{zz}}{\partial z} + \frac{\sigma_{rz}}{r} = 0 \tag{1}$$

$$\begin{aligned} &\sigma_{rr} = (\lambda + 2\mu)\varepsilon_{rr} + \lambda\varepsilon_{\theta\theta} + \lambda\varepsilon_{zz}, \quad \sigma_{\theta\theta} = \lambda\varepsilon_{rr} + (\lambda + 2\mu)\varepsilon_{\theta\theta} + \lambda\varepsilon_{zz} \\ &\sigma_{zz} = \lambda\varepsilon_{rr} + \lambda\varepsilon_{\theta\theta} + (\lambda + 2\mu)\varepsilon_{zz}, \quad \sigma_{rz} = 2\mu\varepsilon_{rz} \end{aligned} \tag{2}$$

$$\varepsilon_{rr} = \frac{\partial u_r}{\partial r}, \varepsilon_{\theta\theta} = \frac{u_r}{r}, \varepsilon_{zz} = \frac{\partial u_z}{\partial z}, \varepsilon_{rz} = \varepsilon_{zr} = \frac{1}{2}\left(\frac{\partial u_r}{\partial z} + \frac{\partial u_z}{\partial r}\right) \tag{3}$$

where $\{\sigma_{rr}, \sigma_{\theta\theta}, \sigma_{zz}, \sigma_{rz}\}$ are non-zero stress components; $\{\varepsilon_{rr}, \varepsilon_{\theta\theta}, \varepsilon_{zz}, \varepsilon_{rz} = \varepsilon_{zr}\}$ are non-zero strain components; and $\{u_r, u_z\}$ are non-zero displacement components.

For the surface (i.e., the zero-thickness layer), the equilibrium conditions on the surface in terms of the generalized Young-Laplace equation [36], Gurtin-Murdoch constitutive relation (e.g., [19, 20]), and strain-displacement relation are given, for the axisymmetric case and the undeformed flat surface, by

$$\frac{d\sigma_{rr}^s}{dr}+\frac{\sigma_{rr}^s-\sigma_{\theta\theta}^s}{r}+t_r^s+q(r)=0\ ,\ \ \frac{d\sigma_{rz}^s}{dr}+\frac{\sigma_{rz}^s}{r}+t_z^s+p(r)=0 \tag{4}$$

$$\sigma_{rr}^s=\tau^s+(2\mu^s+\lambda^s)\varepsilon_{rr}^s+(\lambda^s+\tau^s)\varepsilon_{\theta\theta}^s,\ \ \sigma_{\theta\theta}^s=\tau^s+(2\mu^s+\lambda^s)\varepsilon_{\theta\theta}^s+(\lambda^s+\tau^s)\varepsilon_{rr}^s,\ \ \sigma_{rz}^s=\tau^s\frac{du_z^s}{dr} \tag{5}$$

$$\varepsilon_{rr}^s=\frac{du_r^s}{dr},\varepsilon_{\theta\theta}^s=\frac{u_r^s}{r} \tag{6}$$

where the superscript ‘s’ is used to denote quantities corresponding to the surface and $\mathbf{t}^s$ denote the traction exerted on the bottom side of the surface by the bulk material. It is worth noting that the out-of-plane contribution of the residual surface tension indicated by the third equations of (5) is generally ignored in several earlier studies (e.g., [31, 32]) but it was pointed out by certain investigators that the influence of such out-of-plane stress on elastic responses can become significant (e.g., [13, 33]). By combining equations (4)-(6), it leads to two governing field equations for the surface in terms of the surface displacement $\{u_r^s,u_z^s\}$:

$$\frac{d\overline{\tau}^s}{d\overline{r}}\left(1+\frac{\overline{u}_r^s}{\overline{r}}\right)+\frac{2(\overline{\lambda}+1)}{\overline{\lambda}+2}\left(\frac{d^2\overline{u}_r^s}{d\overline{r}^2}+\frac{1}{\overline{r}}\frac{d\overline{u}_r^s}{d\overline{r}}-\frac{\overline{u}_r^s}{\overline{r}^2}\right)+2(\overline{\lambda}+1)\overline{t}_r^s+\overline{q}(\overline{r})=0 \tag{7}$$

$$\frac{d}{d\overline{r}}\left(\overline{\tau}^s\frac{d\overline{u}_z^s}{d\overline{r}}\right)+\frac{\overline{\tau}^s}{\overline{r}}\frac{d\overline{u}_z^s}{d\overline{r}}+2\overline{t}_z^s(\overline{\lambda}+1)+\overline{p}(\overline{r})=0 \tag{8}$$

where various normalized quantities appearing in (7) and (8) are defined as follows: $\overline{\tau}^s=\tau^s/\mu\Lambda$, $\overline{u}_r^s=u_r^s/\Lambda$, $\overline{u}_z^s=u_z^s/\Lambda$, $\overline{t}_r^s=t_r^s/2(\lambda+\mu)$, $\overline{t}_z^s=t_z^s/2(\lambda+\mu)$, $\overline{\lambda}=\lambda/\mu$, $\overline{r}=r/\Lambda$, $\overline{z}=z/\Lambda$, $\overline{q}(\overline{r})=q(r)/\mu$, $\overline{p}(\overline{r})=p(r)/\mu$, $\Lambda=\kappa^s(\lambda+2\mu)/2\mu(\lambda+\mu)$, and $\kappa^s=2\mu_s+\lambda_s$.

2.3 Boundary Conditions for Bulk

Due to the movement restraint at the base of the elastic layer, all components of the displacement must vanish at $\overline{z}=\overline{h}=h/\Lambda$, i.e.,

$$\overline{u}_r\big|_{\overline{z}=\overline{h}}=0 \tag{9}$$

$$\bar{u}_z\big|_{\bar{z}=\bar{h}} = 0 \tag{10}$$

where $\bar{u}_r = u_r / \Lambda$ and $\bar{u}_z = u_z / \Lambda$. Since the surface is perfectly bonded to the bulk material, the normalized displacements $\{\bar{u}_r^s, \bar{u}_z^s\}$ and the normalized tractions $\{\bar{t}_r^s, \bar{t}_z^s\}$ on the surface can be related directly to the displacement and stress within bulk by

$$\bar{u}_r^s = \bar{u}_r\big|_{\bar{z}=0},\ \bar{u}_z^s = \bar{u}_z\big|_{\bar{z}=0} \tag{11}$$

$$\bar{t}_r^s + \bar{\sigma}_{rz}\big|_{\bar{z}=0} = 0,\ \bar{t}_z^s + \bar{\sigma}_{zz}\big|_{\bar{z}=0} = 0 \tag{12}$$

where $\bar{\sigma}_{rz} = \sigma_{rz} / 2(\lambda + \mu)$ and $\bar{\sigma}_{zz} = \sigma_{zz} / 2(\lambda + \mu)$. By employing (7), (8) and (11), and assuming that $\bar{\tau}^s$ is spatially independent, the relations (12) can be further expressed as

$$\bar{\sigma}_{zz}\big|_{\bar{z}=0} = -\frac{\beta\bar{\tau}^s}{2(\bar{\lambda}+1)}\left(\frac{d^2\bar{u}_z}{d\bar{r}^2} + \frac{1}{\bar{r}}\frac{d\bar{u}_z}{d\bar{r}}\right) - \frac{\bar{p}(\bar{r})}{2(\bar{\lambda}+1)} \tag{13}$$

$$\bar{\sigma}_{rz}\big|_{\bar{z}=0} = -\frac{\alpha}{(\bar{\lambda}+2)}\left(\frac{d^2\bar{u}_r}{d\bar{r}^2} + \frac{1}{\bar{r}}\frac{d\bar{u}_r}{d\bar{r}} - \frac{\bar{u}_r}{\bar{r}^2}\right) - \frac{\bar{q}(\bar{r})}{2(\bar{\lambda}+1)} \tag{14}$$

where constants α and β are introduced only to differentiate among models with and without the consideration of the surface stress effects and the out-of-plane contribution of the residual surface tension; in particular, $\alpha = 1$ if the surface stresses are taken into account otherwise $\alpha = 0$, and $\beta = 1$ if the out-of-plane contribution is taken into account otherwise $\beta = 0$. It is evident that for the special case of $\alpha = \beta = 0$, (13) and (14) simply reduce to traction boundary conditions for the classical case (without the influence of surface stresses). The relations (9)-(10) and (13)-(14) constitute a sufficient set of mixed boundary conditions for the bulk material.

2.4 General Solution of Field Quantities within Bulk

A form of the general solution for the normalized displacement and normalized stress within the bulk material can be obtained by following a standard procedure via Love's strain potential representation and the Hankel integral transform technique (see more details in [37, 38]). The final expressions are given explicitly by

$$\bar{u}_r = (\bar{\lambda}+1)\int_0^\infty \bar{\xi}^2 \frac{dG}{d\bar{z}} J_1(\bar{\xi}\bar{r})\, d\bar{\xi} \tag{15}$$

$$\bar{u}_z = \int_0^\infty \bar{\xi}\left[\frac{d^2G}{d\bar{z}^2} - (\bar{\lambda}+2)\bar{\xi}^2 G\right] J_0(\bar{\xi}\bar{r})d\bar{\xi} \tag{16}$$

$$\bar{\sigma}_{rr} = \left(\int_0^\infty \bar{\xi}\left[\frac{\bar{\lambda}+2}{2(\bar{\lambda}+1)}\bar{\xi}^2\frac{dG}{\partial\bar{z}} + \frac{\bar{\lambda}}{2(\bar{\lambda}+1)}\frac{d^3G}{d\bar{z}^3}\right] J_0(\bar{\xi}\bar{r})d\bar{\xi}\right) - \frac{1}{\bar{r}}\int_0^\infty \bar{\xi}^2\frac{dG}{d\bar{z}} J_1(\bar{\xi}\bar{r})d\bar{\xi} \tag{17}$$

$$\bar{\sigma}_{\theta\theta} = \frac{\bar{\lambda}}{2\left(\bar{\lambda}+1\right)}\int_0^\infty \bar{\xi}\left[\frac{d^3G}{d\bar{z}^3} - \bar{\xi}^2\frac{dG}{d\bar{z}}\right] J_0(\bar{\xi}\bar{r})d\bar{\xi} + \frac{1}{\bar{r}}\int_0^\infty \bar{\xi}^2\frac{dG}{d\bar{z}} J_1(\bar{\xi}\bar{r})d\bar{\xi} \tag{18}$$

$$\bar{\sigma}_{zz} = \int_0^\infty \bar{\xi}\left[\frac{\left(\bar{\lambda}+2\right)}{2\left(\bar{\lambda}+1\right)}\frac{d^3G}{d\bar{z}^3} - \frac{(3\bar{\lambda}+4)}{2\left(\bar{\lambda}+1\right)}\bar{\xi}^2\frac{dG}{d\bar{z}}\right] J_0(\bar{\xi}\bar{r})d\bar{\xi} \tag{19}$$

$$\bar{\sigma}_{rz} = \int_0^\infty \bar{\xi}^2\left[\frac{\bar{\lambda}}{2\left(\bar{\lambda}+1\right)}\frac{d^2G}{d\bar{z}^2} + \frac{(\bar{\lambda}+2)}{2\left(\bar{\lambda}+1\right)}\bar{\xi}^2 G(\bar{\xi},\bar{z})\right] J_1(\bar{\xi}\bar{r})d\bar{\xi} \tag{20}$$

where $J_n(\bar{\xi})$ denotes the Bessel function of the first kind of order *n*, and ξ is the Hankel transform parameter. In addition, $G = G(\bar{\xi},\bar{z})$ is a solution of the bi-harmonic equation in the Hankel transform domain, i.e., the function *G* satisfies

$$\left(\frac{d^2}{d\bar{z}^2} - \bar{\xi}^2\right)^2 G(\bar{\xi},\bar{z}) = 0 \tag{21}$$

A general solution of the homogeneous ordinary differential equation (21) is given by

$$G(\bar{\xi},\bar{z}) = (A + B\bar{z})e^{-\bar{\xi}\bar{z}} + (C + D\bar{z})e^{\bar{\xi}\bar{z}} \tag{22}$$

where *A*, *B*, *C*, and *D* are unknown functions of $\bar{\xi}$ and can be determined by employing appropriate boundary conditions.

2.5 Determination of A, B, C and D

To obtain the complete solution of a particular boundary value problem, the four unknown functions *A*, *B*, *C* and *D* must be determined. This can be achieved by enforcing the boundary conditions at the top and bottom surfaces of the bulk (i.e., at $\bar{z} = 0$ and $\bar{z} = \bar{h}$). By taking Hankel integral transform of all four boundary conditions (9)-(10) and (13)-(14) along with exploiting the relations (15)-(16) and (19)-(20), it leads to a system of four linear algebraic equations in terms of *A*, *B*, *C* and *D*:

$$\begin{bmatrix} \bar{\lambda}+1+\beta\delta\bar{\xi} & 1+\beta\bar{\tau}^s\bar{\xi} & -\bar{\lambda}-1+\beta\delta\bar{\xi} & 1-\beta\bar{\tau}^s\bar{\xi} \\ \bar{\lambda}+1+\alpha\gamma\bar{\xi} & -\bar{\lambda}-\alpha\gamma\bar{\xi} & \bar{\lambda}+1-\alpha\gamma\bar{\xi} & \bar{\lambda}-\alpha\gamma\bar{\xi} \\ -e^{-\bar{\xi}\bar{h}} & (1-\bar{\xi}\bar{h})e^{-\bar{\xi}\bar{h}} & e^{\bar{\xi}\bar{h}} & (1+\bar{\xi}\bar{h})e^{\bar{\xi}\bar{h}} \\ e^{-\bar{\xi}\bar{h}} & \left(\bar{\xi}\bar{h}+\frac{2}{\bar{\lambda}+1}\right)e^{-\bar{\xi}\bar{h}} & e^{\bar{\xi}\bar{h}} & \left(\bar{\xi}\bar{h}-\frac{2}{\bar{\lambda}+1}\right)e^{\bar{\xi}\bar{h}} \end{bmatrix} \begin{Bmatrix} A\bar{\xi} \\ B \\ C\bar{\xi} \\ D \end{Bmatrix} = \begin{Bmatrix} \dfrac{Z(\bar{\xi})}{2\bar{\xi}^2} \\ \dfrac{R(\bar{\xi})}{2\bar{\xi}^2} \\ 0 \\ 0 \end{Bmatrix} \tag{23}$$

where $\gamma=(\bar{\lambda}+1)^2/(\bar{\lambda}+2)$, $\delta=(\bar{\lambda}+1)\bar{\tau}^s/2$, and the functions $Z(\bar{\xi})$ and $R(\bar{\xi})$ are given in terms of the surface loads $\bar{p}(\bar{r})$ and $\bar{q}(\bar{r})$ by

$$Z\left(\bar{\xi}\right)=-\int_0^\infty \bar{p}(\bar{r})J_0(\bar{\xi}\bar{r})\bar{r}d\bar{r} \tag{24}$$

$$R\left(\bar{\xi}\right)=-\int_0^\infty \bar{q}(\bar{r})J_1(\bar{\xi}\bar{r})\bar{r}d\bar{r} \tag{25}$$

A system of equations (23) is sufficient for uniquely determining *A*, *B*, *C*, and *D* as functions of $\bar{\xi}$ and the applied surface loads $Z(\bar{\xi})$ and $R(\bar{\xi})$, and the final explicit solution is given by

$$A=\frac{1}{4}\left[\frac{A_{Z0}+\alpha A_{Z1}}{F}\right]\frac{Z(\bar{\xi})}{\bar{\xi}^3}+\frac{1}{4}\left[\frac{A_{R0}+\beta A_{R1}}{F}\right]\frac{R(\bar{\xi})}{\bar{\xi}^3} \tag{26}$$

$$B=\frac{1}{4}\left[\frac{B_{Z0}+\alpha B_{Z1}}{F}\right]\frac{Z(\bar{\xi})}{\bar{\xi}^2}+\frac{1}{4}\left[\frac{B_{R0}+\beta B_{R1}}{F}\right]\frac{R(\bar{\xi})}{\bar{\xi}^2} \tag{27}$$

$$C=\frac{1}{4}\left[\frac{C_{Z0}+\alpha C_{Z1}}{F}\right]\frac{Z(\bar{\xi})}{\bar{\xi}^3}+\frac{1}{4}\left[\frac{C_{R0}+\beta C_{R1}}{F}\right]\frac{R(\bar{\xi})}{\bar{\xi}^3} \tag{28}$$

$$D=\frac{1}{4}\left[\frac{D_{Z0}+\alpha D_{Z1}}{F}\right]\frac{Z(\bar{\xi})}{\bar{\xi}^2}+\frac{1}{4}\left[\frac{D_{R0}+\beta D_{R1}}{F}\right]\frac{R(\bar{\xi})}{\bar{\xi}^2} \tag{29}$$

where $\{A_{Z0},A_{R0},A_{Z1},A_{R1}\}$, $\{B_{Z0},B_{R0},B_{Z1},B_{R1}\}$, $\{C_{Z0},C_{R0},C_{Z1},C_{R1}\}$, $\{D_{Z0},D_{R0},D_{Z1},D_{R1}\}$ and *F* are given by

$$\begin{aligned}
A_{Z0}&=\frac{\bar{\lambda}(\bar{\lambda}+3)}{(\bar{\lambda}+1)^2}e^{2\bar{\xi}\bar{h}}+2\bar{\xi}^2\bar{h}^2-\frac{2\bar{\xi}\bar{h}\bar{\lambda}}{\bar{\lambda}+1}+\frac{\bar{\lambda}^2+3\bar{\lambda}+4}{(\bar{\lambda}+1)^2} \\
A_{Z1}&=\frac{\bar{\xi}}{\bar{\lambda}+2}\left\{(\bar{\lambda}+3)(e^{2\bar{\xi}\bar{h}}-1)-2\bar{\xi}\bar{h}(\bar{\xi}\bar{h}-1)(\bar{\lambda}+1)\right\} \\
A_{R0}&=\frac{\bar{\lambda}+3}{(\bar{\lambda}+1)^2}e^{2\bar{\xi}\bar{h}}+\frac{3\bar{\lambda}+5}{(\bar{\lambda}+1)^2}+\frac{2\bar{\xi}\bar{h}}{\bar{\lambda}+1}+2\bar{\xi}^2\bar{h}^2 \\
A_{R1}&=\frac{\bar{\tau}^s\bar{\xi}}{2}\left\{\frac{2(\bar{\lambda}+3)}{(\bar{\lambda}+1)^2}(e^{2\bar{\xi}\bar{h}}-1)-\frac{4\bar{\xi}\bar{h}}{\bar{\lambda}+1}-2\bar{\xi}^2\bar{h}^2\right\}
\end{aligned} \tag{30}$$

$$B_{Z0}=(1-2\bar{\xi}\bar{h})+\frac{\bar{\lambda}+3}{\bar{\lambda}+1}e^{2\bar{\xi}\bar{h}},\ B_{Z1}=\frac{\bar{\xi}}{\bar{\lambda}+2}\left\{(e^{2\bar{\xi}\bar{h}}-1)(\bar{\lambda}+3)+2\bar{\xi}\bar{h}(\bar{\lambda}+1)\right\}$$
$$B_{R0}=-(1+2\bar{\xi}\bar{h})-\frac{\bar{\lambda}+3}{\bar{\lambda}+1}e^{2\bar{\xi}\bar{h}},\ B_{R1}=\frac{\bar{\tau}^{s}\bar{\xi}}{2}\left\{\frac{\bar{\lambda}+3}{\bar{\lambda}+1}(1-e^{2\bar{\xi}\bar{h}})+2\bar{\xi}\bar{h}\right\} \tag{31}$$

$$C_{Z0}=-\frac{\bar{\lambda}(\bar{\lambda}+3)}{(\bar{\lambda}+1)^2}e^{-2\bar{\xi}\bar{h}}-2\bar{\xi}^2\bar{h}^2-\frac{2\bar{\xi}\bar{h}\bar{\lambda}}{\bar{\lambda}+1}-\frac{\bar{\lambda}^2+3\bar{\lambda}+4}{(\bar{\lambda}+1)^2}$$
$$C_{Z1}=\frac{\bar{\xi}}{\bar{\lambda}+2}\left\{(\bar{\lambda}+3)(e^{-2\bar{\xi}\bar{h}}-1)-2\bar{\xi}\bar{h}(1+\bar{\xi}\bar{h})(\bar{\lambda}+1)\right\}$$
$$C_{R0}=\frac{\bar{\lambda}+3}{(\bar{\lambda}+1)^2}e^{-2\bar{\xi}\bar{h}}+\frac{3\bar{\lambda}+5}{(\bar{\lambda}+1)^2}-\frac{2\bar{\xi}\bar{h}}{\bar{\lambda}+1}+2\bar{\xi}^2\bar{h}^2 \tag{32}$$
$$C_{R1}=\frac{\bar{\tau}^{s}\bar{\xi}}{2}\left\{-\frac{2(\bar{\lambda}+3)}{(\bar{\lambda}+1)^2}(e^{-2\bar{\xi}\bar{h}}-1)-\frac{4\bar{\xi}\bar{h}}{\bar{\lambda}+1}+2\bar{\xi}^2\bar{h}^2\right\}$$

$$D_{Z0}=(1+2\bar{\xi}\bar{h})+\frac{\bar{\lambda}+3}{\bar{\lambda}+1}e^{-2\bar{\xi}\bar{h}}\ ,\ D_{Z1}=\frac{\bar{\xi}}{\bar{\lambda}+2}\left\{(1-e^{-2\bar{\xi}\bar{h}})(\bar{\lambda}+3)+2\bar{\xi}\bar{h}(\bar{\lambda}+1)\right\}$$
$$D_{R0}=(1-2\bar{\xi}\bar{h})+\frac{\bar{\lambda}+3}{\bar{\lambda}+1}e^{-2\bar{\xi}\bar{h}}\ ,\ D_{R1}=\frac{\bar{\tau}^{s}\bar{\xi}}{2}\left\{\frac{\bar{\lambda}+3}{\bar{\lambda}+1}(1-e^{-2\bar{\xi}\bar{h}})-2\bar{\xi}\bar{h}\right\} \tag{33}$$

$$\begin{aligned}F=&\frac{\bar{\lambda}^2+4\bar{\lambda}+5}{\bar{\lambda}+1}+2(\bar{\lambda}+1)\bar{h}^2\bar{\xi}^2+(\bar{\lambda}+3)\cosh(2\bar{\xi}\bar{h})\\&+\alpha\left\{2(\bar{\lambda}+1)\bar{h}\bar{\xi}^2+(\bar{\lambda}+3)\bar{\xi}\sinh(2\bar{\xi}\bar{h})\right\}\\&+\beta\left\{\frac{\bar{\tau}^{s}\bar{\xi}}{2}\left[(\bar{\lambda}+3)\frac{\bar{\lambda}+2}{\bar{\lambda}+1}\sinh(2\bar{\xi}\bar{h})-2\bar{\xi}\bar{h}(\bar{\lambda}+2)\right]\right\}\\&+\alpha\beta\left\{\frac{\bar{\tau}^{s}\bar{\xi}^2}{2(\bar{\lambda}+2)}\left[(\bar{\lambda}+3)^2\cosh(2\bar{\xi}\bar{h})-(\bar{\lambda}+3)^2-2\bar{\xi}^2\bar{h}^2(\bar{\lambda}+1)^2\right]\right\}\end{aligned} \tag{34}$$

Once the functions *A*, *B*, *C*, and *D* are solved, the displacement and stress within the bulk material can then be obtained by using the relations (15)-(20) along with (22).

3. NUMERICAL INTEGRATION

Although all functions *A*, *B*, *C*, and *D* are obtained in a closed form in terms of the transform parameter $\bar{\xi}$ and applied surface loads, determination of the displacement and stress fields within the bulk material still requires evaluation of various integrals arising from the Hankel transform inversion. Due to the complexity of integrands, the direct integration procedure is not suitable and, in the present study, an efficient numerical quadrature is utilized.

It is evident that all integrals appearing in (15)-(20) are improper with the upper limit equal to infinity. To evaluate such integrals numerically, it is common to truncate the domain

of integration from $(0,\infty)$ to $(0,\ \bar{\xi}_R)$ where $\bar{\xi}_R$ is a finite real number. The approximate displacement and stress fields in terms of *A*, *B*, *C*, and *D* and truncation parameter $\bar{\xi}_R$ are therefore given by

$$\bar{u}_r = (\bar{\lambda}+1)\int_0^{\bar{\xi}_R} \bar{\xi}^2 \left\{\left[-A\bar{\xi}+B(1-\bar{\xi}\bar{z})\right]e^{-\bar{\xi}\bar{z}}+\left[C\bar{\xi}+D(1+\bar{\xi}\bar{z})\right]e^{\bar{\xi}\bar{z}}\right\}J_1(\bar{\xi}\bar{r})d\bar{\xi} \tag{35}$$

$$\bar{u}_z = -(\bar{\lambda}+1)\int_0^{\bar{\xi}_R} \bar{\xi}^2 \left\{\left[A\bar{\xi}+B(\frac{2}{(\bar{\lambda}+1)}+\bar{\xi}\bar{z})\right]e^{-\bar{\xi}\bar{z}}+\left[C\bar{\xi}-D(\frac{2}{(\bar{\lambda}+1)}-\bar{\xi}\bar{z})\right]e^{\bar{\xi}\bar{z}}\right\}J_0(\bar{\xi}\bar{r})d\bar{\xi} \tag{36}$$

$$\begin{aligned}\bar{\sigma}_{rr} = &\int_0^{\bar{\xi}_R} \bar{\xi}^3 \left\{\left[-A\bar{\xi}+B\left(\frac{2\bar{\lambda}+1}{\bar{\lambda}+1}-\bar{\xi}\bar{z}\right)\right]e^{-\bar{\xi}\bar{z}}+\left[C\bar{\xi}+D\left(\frac{2\bar{\lambda}+1}{\bar{\lambda}+1}+\bar{\xi}\bar{z}\right)\right]e^{\bar{\xi}\bar{z}}\right\}J_0(\bar{\xi}\bar{r})d\bar{\xi}\\ &-\frac{1}{\bar{r}}\int_0^{\bar{\xi}_R} \bar{\xi}^2 \left(\left[-A\bar{\xi}+B(1-\bar{\xi}\bar{z})\right]e^{-\bar{\xi}\bar{z}}+\left[C\bar{\xi}+D(1+\bar{\xi}\bar{z})\right]e^{\bar{\xi}\bar{z}}\right)J_1(\bar{\xi}\bar{r})d\bar{\xi}\end{aligned} \tag{37}$$

$$\begin{aligned}\bar{\sigma}_{\theta\theta} = &\frac{\bar{\lambda}}{\bar{\lambda}+1}\int_0^{\bar{\xi}_R} \bar{\xi}^3 \left\{Be^{-\bar{\xi}\bar{z}}+De^{\bar{\xi}\bar{z}}\right\}J_0(\bar{\xi}\bar{r})d\bar{\xi}\\ &+\frac{1}{\bar{r}}\int_0^{\bar{\xi}_R} \bar{\xi}^2 \left(\left[-A\bar{\xi}+B(1-\bar{\xi}\bar{z})\right]e^{-\bar{\xi}\bar{z}}+\left[C\bar{\xi}+D(1+\bar{\xi}\bar{z})\right]e^{\bar{\xi}\bar{z}}\right)J_1(\bar{\xi}\bar{r})d\bar{\xi}\end{aligned} \tag{38}$$

$$\bar{\sigma}_{zz} = \int_0^{\bar{\xi}_R} \bar{\xi}^3 \left\{\left[A\bar{\xi}+B\left(\frac{1}{\bar{\lambda}+1}+\bar{\xi}\bar{z}\right)\right]e^{-\bar{\xi}\bar{z}}+\left[-C\bar{\xi}+D\left(\frac{1}{\bar{\lambda}+1}-\bar{\xi}\bar{z}\right)\right]e^{\bar{\xi}\bar{z}}\right\}J_0(\bar{\xi}\bar{r})d\bar{\xi} \tag{39}$$

$$\bar{\sigma}_{rz} = \int_0^{\bar{\xi}_R} \bar{\xi}^3 \left\{\left[A\bar{\xi}-B\left(\frac{\bar{\lambda}}{\bar{\lambda}+1}-\bar{\xi}\bar{z}\right)\right]e^{-\bar{\xi}\bar{z}}+\left[C\bar{\xi}+D\left(\frac{\bar{\lambda}}{\bar{\lambda}+1}+\bar{\xi}\bar{z}\right)\right]e^{\bar{\xi}\bar{z}}\right\}J_1(\bar{\xi}\bar{r})d\bar{\xi} \tag{40}$$

While the convergence of above approximate integrals to an analytical solution is ensured mathematically as $\bar{\xi}_R$ approaches infinity, in the numerical calculations, it suffices to choose a relatively large $\bar{\xi}_R$ such that the error from the approximation is less than a specified tolerance since all integrands possess a desirable rate of decay at infinity. However, due to the oscillating nature of their integrands introduced by Bessel functions $J_0(\bar{\xi}\bar{r})$ and $J_1(\bar{\xi}\bar{r})$, the numerical evaluation of all truncated integrals appearing in (35)-(40) by standard Gaussian quadrature over a single interval generally requires a large number of integrations points. To enhance the computation efficiency, the integral over the interval $[0,\bar{\xi}_R]$ is first divided into *N* sub-integrals and Gaussian quadrature is then applied to each sub-integral. As *N* increases, the oscillating behavior of the integrand in each sub-integral essentially

disappears and they can, therefore, be integrated accurately by using low-order Gaussian quadrature.

In the present study, the suitable truncated parameter ($\bar{\xi}_R$), number of sub-integrals (N), and number of integration points (n) utilized in the numerical integration are fully investigated to ensure the accuracy of numerical results while still consuming reasonable computational time. Both n and N have the direct influence on the accuracy of the numerical integration for a fixed truncation parameter $\bar{\xi}_R$. In general, by increasing N, each sub-integral requires less number of integration points since the oscillating behavior of the integrand gradually disappears. In the numerical experiment, for a fixed $\bar{\xi}_R$, N is increased until the value of the integral converges (for a specified tolerance) by using a low order Gaussian quadrature for each sub-integral. The ratio $\bar{\xi}_R / N$ is then recorded and used to indicate the size of the sub-interval over which the integrand is sufficiently well-behaved to be integrated using low order Gaussian quadrature. Finally, a proper choice of the truncation parameter $\bar{\xi}_R$ is obtained by increasing such upper limit until the value of the integral converges (for a specified tolerance). It is important to remark that in such process, the number of sub-integrals must be increased accordingly in order to maintain the size of the sub-intervals ($\bar{\xi}_R / N$) sufficiently small to allow the use of low-order Gaussian quadrature.

4. NUMERICAL RESULTS AND DISCUSSION

To verify both the formulation and numerical integration scheme, obtained results are first compared with available benchmark solutions. Once the proposed technique is fully tested, extensive studies for a layer under both axisymmetric normal and axisymmetric tangential surface loads are investigated to understand the nano-scale influence and size-dependent behaviors through the surface stress effects (with/without the contribution of the residual surface tension). Moreover, fundamental results of an elastic layer under a unit normal point load, a unit normal ring load, and a unit tangential ring load are also demonstrated and fully discussed.

4.1 Verification

In this sub-section, results obtained in the present study are verified with three available benchmark solutions. Without the integration of surface stresses in the mathematical model, the present numerical results are verified with the classical solutions of an elastic layer

proposed by Burmister [39-40] and an elastic half space reported by Ahlvin and Ulery [41], respectively. Moreover, obtained results are also compared with the solution proposed by Zhao [28] for the case that the influence of surface stresses is taken into account without the out-of-plane contribution of the residual surface tension.

4.1.1 Infinite rigid-based elastic layer under normal point force

Consider a point load P_{pt}, normalized such that $\bar{P}_{pt} = P_{pt} / \mu\Lambda^2$, acting normal to the surface of a rigid-based layer with the normalized thickness $\bar{h} = 1.0$ and Poisson's ratio $\nu = 0.2$ as shown in Fig. 2(a). Results for this particular case without the influence of surface stresses can readily be obtained by setting $\alpha = 0$ and $\beta = 0$. The radial and vertical displacements at the surface and non-zero stress components at $\bar{z} = 0.1$ along the radial direction are reported and compared with analytical solutions proposed by Bumister [39-40], which were tabulated by Poulos [42], in Tables 1-3. It is obvious from this set of results that solutions obtained from the present study show very good agreement with the benchmark solution.

4.1.2 Elastic half-space under uniformly distributed normal traction

A three-dimensional, elastic half-space with Poisson's ratio $\nu = 0.2$ and subjected to uniformly distributed normal traction p_0 over a circular area of normalized radius $\bar{a} = a / \Lambda$ shown in Fig. 2(b) is considered without the surface stress effects. To treat this classical case, α and β are taken to be zero and the normalized thickness $\bar{h}$ is chosen to be sufficiently large in the analysis to represent the half-space. Results for non-zero displacement and stress components are reported in Table 4 along with those reported by Ahlvin and Ulery [41]. Similar to the previous case, solutions obtained from the current study are almost indistinguishable from the reference results.

4.1.3 Infinite rigid-based elastic layer under uniformly distributed normal traction

Consider, next, an infinite, rigid-based, elastic layer with the normalized thickness $\bar{h} = 30$ and subjected to uniformly distributed normal traction p_0, normalized such that $\bar{p}_0 = p_0 / \mu$, over a circular area of normalized radius $\bar{a} = a / \Lambda = 10$ as shown in Fig. 2(c). To allow a direct comparison with available results proposed by Zhao [28], the same set of material constants obtained from atomistic simulation [7, 22] is utilized (i.e., λ = 58.17x10^9 N/m^2, μ = 26.13x10^9 N/m^2, λ^s = 6.8511 N/m, μ^s = -0.376 N/m, τ^s = 1 N/m). Note that this particular set of material properties is also employed for the rest of numerical study presented hereafter. Results for the classical case, and the case accounting for the surface stress effects without

the out-of-plane contribution of the residual surface tension can be obtained by simply setting $\alpha = 0, \beta = 0$, and $\alpha = 1, \beta = 0$, respectively. By comparing results for the surface displacement and stresses at $\bar{z} = 0.1$ along the radial direction with those presented by Zhao [28] for $\bar{h} / \bar{a} = 3$ as shown in Figs. 3 and 4, it is found that solutions obtained from the present study are in excellent agreement with the benchmark solutions.

4.2 Influence of Surface Stresses

After the proposed solution and numerical scheme are verified, extensive parametric studies are performed to demonstrate the influence of surface stresses, the significant contribution of the residual surface tension, and the size-dependent behavior of the elastic field of the layer under normal and tangential axisymmetric surface loads.

4.2.1 Infinite rigid-based elastic layer under uniformly distributed normal traction

Consider an infinite, rigid-based, elastic layer subjected to uniformly distributed normal traction p_0 over a circular area of normalized radius $\bar{a}$ as shown in Fig. 2(c). Results for both radial and vertical surface displacements along the radial direction for $\bar{a} = 10$ and various values of the normalized thickness $\bar{h}$ are reported in Fig. 5. It is apparent from this set of results that a model incorporating the out-of-plane component of the surface stresses (i.e., the third equation of (5)) predicts much lower surface displacement or, equivalently, renders materials stiffer whereas the solution obtained from a model excluding the out-of-plane contribution exhibits significant influence of the surface stresses only in the case of the radial displacement. This implies that the out-of-plane contribution of the residual surface tension is significant and, in general, cannot be neglected. In addition, results for all cases show similar trend for all values of $\bar{h}$ considered; in particular, the magnitude of the displacement is larger as the normalized thickness of the layer increases.

For non-zero stress components, results are obtained for $\bar{h} = 10$, $\bar{a} = 1$, and three different normalized depths $\bar{z} \in \{0.25, 0.5, 1.0\}$. The variation of the normalized vertical stress in the radial direction is reported in Fig. 6(a). Clearly, the vertical stresses for all cases reach the maximum value at $\bar{r} = 0$ and decay monotonically and rapidly to zero as $\bar{r}$ increases. Due to the presence of surface stresses, values of the vertical stress are lesser within the region under the surface loads ($\bar{r} / \bar{a} \le 1.0$) and insignificantly higher for $\bar{r} / \bar{a} > 1.0$ in comparison with the classical solution. It can also be concluded from this set of results that the influence of surface stresses is more significant in the region relatively close to the

surface. In addition, such behavior becomes more apparent if the model incorporating the out-of-plane contribution of the residual surface tension is utilized in the analysis.

Results for the normalized shear stress $\bar{\sigma}_{rz}$ are also reported in Fig. 6(c) for various normalized depths. The shear stress along the radial direction predicted by three different models exhibit the similar trend. In particular, the shear stress vanishes at $\bar{r} = 0$ due to the symmetry, rapidly increases and reaches its peak near the edge of the loading area (i.e., $\bar{r} / \bar{a} \approx 1$), and promptly decay after reaching the peak. It is worth noting that, in the region very near the edge of the loading area, the surface stresses especially in a model including the out-of-plane contribution of the residual surface tension significantly lower the magnitude of the shear stress. As anticipated, the influence of surface stresses is quite large in a region near the surface and becomes negligible in a region far away from the surface. The variation of the normalized radial stress $\bar{\sigma}_{rr}$ and normalized hoop stress $\bar{\sigma}_{\theta\theta}$ along the radial direction are also presented for various depths in Figs. 6(b) and 6(d), respectively. While all three different models yield qualitatively similar stress profiles, presence of the surface stresses generally lowers the magnitude of stresses and the discrepancy from the classical solution is magnified when the out-of-plane component is included.

Through the proper normalization, solutions obtained by a classical case without the surface stress effects exhibit no size-dependency. However, this is different for results predicted by the other two models integrating the surface stresses with/without the out-of-plane term. The size-dependent behavior can be observed due to the existence of an intrinsic length scale associated with the presence of the surface stresses. In this study, the size-dependency of all normalized stresses is investigated by varying the radius of the loading region while maintaining the ratio $\bar{h} / \bar{a}$. Results for $\bar{h} / \bar{a} = 3$ and $\bar{r} / \bar{a} = 0.5$ of three different depths are reported in Fig. 7. Unlike the classical solutions, results obtained from the two models accounting for surface stresses depend strongly on the normalized radius $\bar{a}$ for relatively small $\bar{a}$ and such dependence gradually disappear as $\bar{a}$ increases. It is worth emphasizing that results predicted by the model taking the out-of-plane contribution of the residual surface tension exhibit much stronger size-dependency than that excluding the out-of-plane term.

4.2.2 Infinite rigid-based elastic layer under linearly distributed tangential traction

For this particular case, the infinite, rigid-based elastic layer subjected to linearly distributed, tangential traction $q(r) = q_0 r / a$ over a circular area of normalized radius $\bar{a}$ as shown in Fig.

2(d) is investigated. The prescribed traction is normalized such that $\bar{q}(\bar{r}) = \bar{q}_0 \bar{r} / \bar{a}$ where $\bar{q}_0 = q_0 / \mu$ and q_0 is the maximum traction at the edge of the loading region. Results for the normalized radial and vertical displacements for different thicknesses of the layer are reported in Fig. 8. It is evident from these results that the presence of surface stresses significantly lowers the magnitude of the displacement. However, the out-of-plane surface stress has a very strong influence on the vertical displacement and becomes negligible for the radial displacement. Moreover, when the thickness of the layer increases, both the radial and vertical displacements increase.

For non-zero stress components, results are obtained for $\bar{h} = 10$, $\bar{a} = 1$, and three different normalized depths $\bar{z} \in \{0.25, 0.5, 1.0\}$. Profiles of the normalized vertical stresses $\bar{\sigma}_{zz}$ along the radial direction are reported in Fig. 9(a). At a relatively small depth, the tensile stress is observed within a region under the loading area and it gradually changes to the compressive stress when passing the edge of the loading area. The vertical stress profiles also show the strong influence of the surface stresses for the region relatively near the surface. Moreover, the discrepancy of results predicted by the two models with/without the out-of-plane contribution of the residual surface tension is more apparent for the vertical stress but insignificant for the radial stresses $\bar{\sigma}_{rr}$ and the hoop stresses $\bar{\sigma}_{\theta\theta}$ (see Figs. 9(b) and 9(d)). Results for the normalized shear stress $\bar{\sigma}_{rz}$ are also reported in Fig. 9(c) for various depths. For this particular loading condition, the shear stress increases to reach its peak near the edge of the loading region and then abruptly decreases to zero after passing the edge of the loading area. Again, the influence of the surface stresses on this shear stress component is more apparent for the region close to the surface.

To demonstrate the size-dependent behavior of solutions for a layer subjected to the linearly distributed tangential traction, a scheme similar to that used to study a layer under uniformly distributed normal traction is employed. The layer thickness and the radius of the loading region are varied while their ratio is fixed with $\bar{h} / \bar{a} = 3$. The relationship between the normalized stress components and the normalized radius of the loading region for three different depths and $\bar{r} / \bar{a} = 0.5$ are reported in Fig. 10. Unlike the case of uniformly distributed normal load, the out-of-plane contribution of the residual surface tension has very strong influences only on the vertical stress whereas, for other stress components, such contribution becomes negligible. However, solutions obtained from the two models accounting for the surface stresses still show the size-dependency. In particular, as the

normalized radius $\bar{a}$ and the normalized depth $\bar{z}$ decrease, the surface stress effects become more significant and the size-dependency of the predicted solution is obvious.

4.3 Fundamental Solutions

Since the formulation has been established for arbitrarily distributed, axisymmetric surface loads, general results can be further specialized to construct certain fundamental solutions. Here, solutions of an infinite, rigid-based, elastic layer subjected to three special loading conditions including a normal concentrated load at the origin, a normal ring load, and a tangential ring load are obtained. Although only results for the surface displacement are reported and discussed for the sake of brevity, other field quantities such as the displacement and stress at any location within the bulk can also be determined in a similar fashion.

4.3.1 Infinite rigid-based elastic layer under normal concentrated load at origin

Consider an infinite, rigid-based, elastic layer subjected to a normal concentrated load P_{pt} (with the normalized load $\bar{P}_{pt} = P_{pt} / \mu\Lambda^2$) as shown in Fig. 2(a). Profiles of the normalized radial displacement $\bar{u}_r$ and the normalized vertical displacement $\bar{u}_z$ at the surface obtained by three different models are reported in Fig. 11 for four different layer thicknesses $\bar{h} \in \{0.5, 1.0, 2.0, 3.0\}$. It is found that the normalized radial displacement is singular at $\bar{r} = 0$ except the solution obtained from a model accounting for the out-of-plane contribution of the residual surface stress. On the other hand, results of the normalized vertical displacement tend to be infinite under the concentrated load for all cases and reduce rapidly when $\bar{r}$ increases. In addition, the similar behavior is observed for all layer thicknesses considered and the magnitude of the displacement is higher as the layer thickness increases.

4.3.2 Infinite rigid-based elastic layer under normal ring load

Consider, next, an infinite, rigid-based, elastic layer subjected to a normal ring load at the radius *a*, i.e., $p(r) = p_r \delta(r - a)$ where p_r is a prescribed constant. The prescribed ring load is normalized such that $\bar{p}(\bar{r}) = \bar{p}_r \delta(\bar{r} - \bar{a})$ where $\bar{p}_r = p_r / \mu\Lambda$. Results for the normalized radial displacement $\bar{u}_r$ and the normalized vertical displacement $\bar{u}_z$ at the surface are plotted along the radial direction as shown in Fig. 12 for four different layer thicknesses $\bar{h} \in \{0.5, 1.0, 2.0, 3.0\}$ and $\bar{a} = 1$. It is apparent from this set of results that the radial displacement for the classical case exhibits rapid variation at the location of the applied ring load while those obtained from the other two models are finite, smooth, and significantly

different from the classical solution. On the contrary, the vertical displacements predicted by the classical model and a model accounting for the surface stresses without the out-of-plane term are slightly different and singular at the location of applied load whereas that obtained from a model incorporating the out-of-plane term is finite and significantly different from the other two solutions.

4.3.3 Infinite rigid-based elastic layer under tangential ring load

Finally, consider an infinite, rigid-based, elastic layer subjected to a tangential ring load at the radius a, i.e., $q(r) = q_r \delta(r-a)$ where q_r is a prescribed constant. Such applied load is normalized such that $\bar{q}(\bar{r}) = \bar{q}_r \delta(\bar{r} - \bar{a})$ where $\bar{q}_r = q_r / \mu\Lambda$. Results for the normalized radial displacement $\bar{u}_r$ and the normalized vertical displacement $\bar{u}_z$ at the surface along the radial direction are reported in Fig. 13, once again, for four different layer thicknesses $\bar{h} \in \{0.5, 1.0, 2.0, 3.0\}$ and $\bar{a} = 1$. For this particular loading condition, both the radial and vertical surface displacements obtained from the classical model are singular at the location of the applied ring load whereas those obtained from the two models accounting for the surface stresses are finite everywhere. While the results obtained from the two models exhibit huge discrepancy from the classical solution, the contribution of the out-of-plane surface stress is insignificant especially for the surface radial displacement.

5. APPLICATIONS OF FUNDAMENTAL SOLUTIONS

Results obtained in sub-section 4.3 for three fundamental loading conditions can be employed to construct Green's function for both the displacements and stresses. Such Green's functions possess vast applications such as in the calculation of an elastic field of the layer under arbitrarily distributed, axisymmetric surface loads and in the development of governing integral equations for contact and indentation problems.

To clearly demonstrate their applications, let us consider a three-dimensional, infinite, rigid-based, elastic layer subjected to arbitrarily distributed, axisymmetric normal traction $p(r)$ and tangential traction $q(r)$. Once solutions of all field quantities due to both unit normal and unit tangential ring loads are determined, they can be utilized along with a method of superposition to obtain the integral relations for both the displacement and stress on the surface and within the bulk material due to the tractions $p(r)$ and $q(r)$. For instance, the radial and vertical displacements at any distance $\hat{r}$ on the surface are given by

$$u_r(\hat{r}) = \int_0^\infty U_r^N(\hat{r}, r)\, p(r) dr + \int_0^\infty U_r^T(\hat{r}, r) q(r) dr \tag{41}$$

$$u_z(\hat{r}) = \int_0^\infty U_z^N(\hat{r}, r)\, p(r) dr + \int_0^\infty U_z^T(\hat{r}, r) q(r) dr \tag{42}$$

where $U_r^N(\hat{r}, r)$ and $U_z^N(\hat{r}, r)$ are radial and vertical displacements at any distance $\hat{r}$ on the surface due to a unit normal ring load acting on the surface of the layer at the radius *r*, respectively, and $U_r^T(\hat{r}, r)$ and $U_z^T(\hat{r}, r)$ are radial and vertical displacements at any distance $\hat{r}$ on the surface due to a unit tangential ring load acting on the surface of the layer at the radius *r*. Other field quantities at any point ($\hat{r}$, $\hat{z}$) within the bulk material, denoted generically by $\mathcal{R}(\hat{r}, \hat{z})$, can also be obtained in a similar fashion as

$$\mathcal{R}(\hat{r}, \hat{z}) = \int_0^\infty \mathcal{R}^N(\hat{r}, \hat{z}; r)\, p(r) dr + \int_0^\infty \mathcal{R}^T(\hat{r}, \hat{z}; r) q(r) dr \tag{43}$$

where $\mathcal{R}^N(\hat{r}, \hat{z}; r)$ and $\mathcal{R}^T(\hat{r}, \hat{z}; r)$ are corresponding responses at any point ($\hat{r}$, $\hat{z}$) within the bulk material due to the unit normal ring load and unit tangential ring load acting on the surface of the layer at the radius *r*, respectively. Clearly, for a problem where the surface traction *p*(*r*) and *q*(*r*) are fully prescribed, the integral relations (41)-(43) can be directly employed to determine all field quantities.

For contact and nano-indentation problems, the traction *p*(*r*) and *q*(*r*) under an indentor are unknown a priori and they must be determined before the integral relation (43) can be used. For a special case of an axisymmetric, rigid, frictionless, nano-indentation problem, the tangential traction *q*(*r*) vanishes and the vertical displacement under the indentor is fully prescribed in terms of the known indentor profile v^p and the prescribed indentation depth *d*. The integral relation (42) for any $\hat{r}$ under the indentor becomes

$$u_z(\hat{r}) = \int_0^a U_z^N(\hat{r}, r)\, p(r) dr = d + v^p(\hat{r}) \quad , \quad \hat{r} \le a \tag{44}$$

where *a* denotes the contact radius. The integral equation (44) can be solved to obtain the unknown contact pressure *p*(*r*). Once *p*(*r*) is determined, all other field quantities can readily be obtained from the integral relation (43) with *q*(*r*) = 0.

For an axisymmetric, rigid, fully bonded, nano-indentation problem, the radial displacement under the indentor identically vanishes and the vertical displacement under the indentor is fully prescribed in terms of the known indentor profile v^p and the prescribed indentation depth d. The integral relations (41) and (42) for any $\hat{r}$ under the indentor become

$$u_r(\hat{r}) = \int_0^a U_r^N(\hat{r}, r)\, p(r) dr + \int_0^a U_r^T(\hat{r}, r) q(r) dr = 0 \quad , \quad \hat{r} \le a \tag{45}$$

$$u_z(\hat{r}) = \int_0^a U_z^N(\hat{r}, r)\, p(r) dr + \int_0^a U_z^T(\hat{r}, r) q(r) dr = d + v^p(\hat{r}) \quad , \quad \hat{r} \le a \tag{46}$$

The two integral equations (45)-(46) are sufficient for solving the unknown traction $p(r)$ and $q(r)$. Once the unknown traction is obtained, all other field quantities can be computed, again, from the integral relation (43).

For an axisymmetric, rigid, rough, nano-indentation problem, the tangential traction $q(r)$ can be related to the normal traction $p(r)$ via a selected friction model and, once again, the vertical displacement under the indentor is fully prescribed in terms of the known indentor profile v^p and the prescribed indentation depth d. The integral relation (42) for any $\hat{r}$ under the indentor becomes

$$u_z(\hat{r}) = \int_0^a U_z^N(\hat{r}, r)\, p(r) dr + \int_0^a U_z^T(\hat{r}, r)\, f(p(r)) dr = d + v^p(\hat{r}) \quad , \quad \hat{r} \le a \tag{47}$$

where a prescribed function f denotes the relation between p and q via the friction model. The integral equation (47) can be employed to solve for the unknown normal traction $p(r)$. Once $p(r)$ is determined, the tangential traction $q(r)$ can readily be obtained from the function f and all other field quantities can be computed from the integral relation (43).

By following the same strategy, solutions of all field quantities due to a unit normal concentrated load applied to the surface of a layer can also be utilized as Green's functions to establish integral relations for field quantities due to arbitrary distributed, normal traction on the surface. In addition, the integral relation for the vertical displacement on the surface can be employed to form the integral equation governing the unknown pressure under the rigid, frictionless indentor of arbitrary profiles.

While the formulation of the integral equations sufficient for solving the indentation problems is already established here, it still requires non-trivial and challenging tasks

regarding to various computational issues such as the efficiency and accuracy of the numerical procedure and approximate solutions, and this should deserve further investigation.

6. CONCLUSIONS AND REMARKS

A complete solution of a three-dimensional, infinite, rigid-based, elastic layer under axisymmetric normal and tangential surface loads with consideration of the surface stresses has been derived. A novel feature of the present study is the use of a complete version of Gurtin-Murdoch constitutive relation to model the free surface of the elastic layer. In the solution procedure, Love's strain potential representation along with Hankel integral transform technique has been applied to obtain the general solution for the bulk material whereas the surface equations and conditions at the rigid base supply sufficient boundary conditions to determine all arbitrary constants. The displacement and stress fields within the bulk material have been obtained via a selected efficient numerical quadrature. Once the obtained solutions were verified by comparing with available benchmark solutions, extensive parametric study has been carried out to gain insight into the nano-scale influence and also fully investigate the size-dependent behavior. Moreover, fundamental solutions corresponding to normal concentrated load, normal ring load, and tangential ring load have also been constructed.

Results from extensive parametric studies have confirmed the significance of the surface stresses and the necessity to properly treat such influence in the continuum-based model. In the region relatively close to the surface, the presence of the surface stresses exhibits very strong influence on both the displacement and stress fields. Magnitudes of field quantities obtained from models accounting for the surface effects are generally less than those obtained from the classical model. This is due to the fact that the applied surface loads do not entirely transfer into the bulk but part of them is carried by the surface through the equilibrium of the surface and the membrane-like action. Such influences also depend primarily on the length scale of the problem; the influence of the surface stresses becomes significant when the length scale is comparable to the intrinsic length of the surface. Moreover, it is worth pointing out that such behavior of the out-of-plane responses under the normal traction is more apparent in the model that integrates the out-of-plane contribution of the residual surface tension. This additionally confirms the necessity to treat such crucial contribution in the modeling of soft elastic solids and nano-scale problems.

In addition, the surface radial and vertical displacements of a layer under either a normal ring load or a tangential ring load predicted by a model employed in the present study are finite everywhere. If the out-of-plane component of the surface stresses is neglected, the predicted vertical displacement due to the normal ring load is still singular at the location where the load is applied. For the case of a normal concentrated load, the vertical displacement obtained from both the classical model and the model incorporating the surface stresses is singular at the location of the applied load and only the radial displacement obtained from a model accounting for the out-of-plane term is finite.

ACKNOWLEDGEMENT

The work presented in this paper was supported by the Thailand Research Fund (Grant No. BRG5480006). This support is gratefully acknowledged.

REFERENCES

[1] Wong, E. W., Sheehan, P. E., Lieber, C. M. Nanobeam mechanics: Elasticity, strength, and toughness of nanorods and nanotubes, *Science*, **277**, 1997, pp. 1971-1975

[2] Mao, S. X., Zhao, M., Wang, Z. L. Nanoscale mechanical behavior of individual semiconducting nanobelts, *Applied Physics Letters*, **83**, 2003, pp. 993-995

[3] Poncharal, P., Wang, Z. L., Ugarte, D., de Heer, W. A. Electrostatic deflections and electromechanical resonances of carbon nanotubes, *Science*, **283**, 1999, pp. 1513-1516

[4] He, L.H., Lim, C.W. Surface green function for a soft elastic half-space: Influence of surface stress, *International Journal of Solids and Structures*, **43**, 2006, pp. 132–143

[5] Dingreville, R., Qu, J., Cherkaoui, M. Surface free energy and its effect on the elastic behavior of nano-sized particles, wires and films, *Journal of the Mechanics and Physics of Solids*, **53**, 2005, pp. 1827-1854

[6] Zhang, S., Mielke, S.L., Khare, R., Troya, D., Ruoff, R.S., Schatz, G.C., Belytschko, T. Mechanics of defects in carbon nanotubes: Atomistic and multiscale simulations, *Physical Review B*, **71**, 2005, 115403

[7] Shenoy, V.B. Atomistic calculations of elastic properties of metallic fcc crystal surfaces, *Physical Review B*, **71**, 2005, 094104

[8] Tian, L., Rajapakse, R.K.N.D. Analytical solution for size-dependent elastic field of a nanoscale circular inhomogeneity, *Journal of Applied Mechanics*, **74**, 2007, pp. 568-574

[9] Tian, L., Rajapakse, R.K.N.D. Elastic field of an isotropic matrix with a nanoscale elliptical inhomogeneity, *International Journal of Solids and Structures*, **44**, 2007, pp. 7988-8005.

[10] Pugno, N., Carpinteri, A., Ippolito, M., Mattoni, A., Colombo, L. Atomistic fracture: QFM vs. MD, *Engineering Fracture Mechanics*, **75**, 2008, pp. 1794-1803

[11] Phan, A.V., Tippur, H.V. Shape-sensitivity-based evaluation of the stress intensity factors at the nanoscale by means of quantized fracture mechanics, *Mechanics Research Communications*, **36**, 2009, pp. 336-342

[12] Wang, W., Zeng, X., Ding, J. Finite element modeling of two-dimensional nanoscale structures with surface effects, *World Academy of Science, Engineering and Technology*, **72**, 2010, pp. 867-872

[13] Pinyochotiwong, Y., Rungamornrat, J., Senjuntichai, T. Rigid frictionless indentation on elastic half space with influence of surface stresses, *International Journal of Engineering Science*, **71**, 2013, pp. 15-35

[14] Yakobson, B.I. Nanomechanics, in: Goddard, W.A., Brenner, D.W., Lyshevski, S.E., Iafrate, G.J. (Eds.), *Handbook of Nanoscience*, Engineering and Technology, CRC Press, Florida, 2003, pp. 17.1-17.18

[15] Gibbs, J.W. *The Scientific Papers of J. Willard Gibbs*, Vol. 1, Longmans Green, London, 1906

[16] Cammarata, R.C. Surface and interface stress effects in thin films, *Progress in Surface Science*, **46**, 1994, pp. 1-38

[17] Cammarata, R.C. Surface and interface stress effects on interfacial and nanostructured materials, *Materials Science and Engineering A*, **237**, 1997, pp. 180-184

[18] Fischer, F.D., Waitz, T., Vollath, D., Simha, N.K. On the role of surface energy and surface stress in phase-transforming nanoparticles, *Progress in Materials Science*, **53**, 2008, pp. 481-527

[19] Gurtin, M.E., Murdoch, A.I. A continuum theory of elastic material surfaces, *Archive for Rational Mechanics and Analysis*, **57**, 1975, pp. 291-323

[20] Gurtin, M.E., Murdoch, A.I. Surface stress in solid, *International Journal of Solids and Structures*, **14**, 1978, pp. 431-440

[21] Gurtin, M.E., Weissmüller, J., Larché, F. A general theory of curved deformable interfaces in solids at equilibrium, *Philosophical Magazine A*, **78**, 1988, pp. 1093-1109

[22] Miller, R.E., Shenoy, V.B. Size-dependent elastic properties of nanosized structural elements, *Nanotechnology*, **11**, 2000, pp. 139-147

[23] Shenoy, V.B. Size-dependent rigidities of nanosized torsional elements, *International Journal of Solids and Structures*, **39**, 2002, pp. 4039–4052

[24] He, L.H., Lim, C.W., Wu, B.S. A continuum model for size-dependent deformation of elastic films of nano-scale thickness, *International Journal of Solids and Structures*, **41**, 2004, pp. 847-857

[25] Huang, D.W. Size-dependent response of ultra-thin films with surface effects, *International Journal of Solids and Structures*, **45**, 2008, pp. 568-579

[26] Sharma, P., Ganti, S., Bhate, N. Effect of surfaces on the size-dependent elastic state of nano-inhomogeneities, *Applied Physics Letters*, **82**, 2003, pp. 535-537

[27] Sharma, P., Wheeler, L.T. Size-dependent elastic state of ellipsoidal nano-inclusions incorporating surface/interface tension, *Journal of Applied Mechanics-Transactions of the ASME*, **74**, 2007, pp. 447-454

[28] Zhao, X.J. Surface loading and rigid indentation of an elastic layer with surface energy effects, *Master thesis*, The University of British Columbia, Canada, 2009

[29] Wang, G.F., Feng, X.Q. Effect of surface stresses on a contact problem at nanoscale, *Journal of Applied Physics*, **101**, 2007, 013510

[30] Huang, G.Y., Yu, S.W. Effect of surface elasticity on the interaction between steps, *Journal of Applied Mechanics*, **74**, 2007, pp. 821-823

[31] Zhao, X.J., Rajapakse, R.K.N.D. Analytical solutions for a surface-loaded isotropic elastic layer with surface energy effects, *International Journal of Engineering Science*, **47**, 2009, pp. 1433-1444

[32] Intarit, P., Senjuntichai, T., Rajapakse, R.K.N.D. Dislocations and internal loading in a semi-infinite elastic medium with surface stresses, *Engineering Fracture Mechanics*, 77, 2010, pp. 3592-3603

[33] Intarit, P., Senjuntichai, T., Rungamornrat, J., Rajapakse, R.K.N.D. Surface Elasticity and Residual Stress Effect on the Elastic Field of a Nanoscale Elastic Layer, *Interaction and Multiscale Mechanics*, **4**, 2011, pp. 85-105

[34] Barber, J.R. *Elasticity*. Kluwer Academic Publisher, Netherlands, 1992

[35] Timoshenko, S., Goodier, J.N. *Theory of Elasticity*. McGraw-Hill, New York, 1951

[36] Povstenko, Y.Z. Theoretical investigation of phenomena caused by heterogeneous surface tension in solids, *Journal of the Mechanics and Physics of Solids*, **41**, 1993, pp. 1499-1514

[37] Sheddon, I.N. *Fourier transform*. McGraw-Hill, New York, 1951

[38] Selvadurai, A.P.S. *Partial differential equations in mechanics 2*. Springer, Germany, 2000

[39] Burmister, D.M. The theory of stresses and displacements in layered systems and applications to the design of airport runways, *Proceedings of Highway Research Board*, **23**, 1943, pp. 127-148

[40] Burmister, D.M. The general theory of stresses and displacements in layered soil systems, *Applied Physics*, **16**, 1945, pp. 89-96, 126-127, 296-302

[41] Ahlvin, R.G., Ulery, H.H. Tabulated values for determining the complete pattern of stresses, strains, and deflections beneath a uniform load on a homogeneous half space, *Highway Research Board*, Bulletin **342**, 1962, pp. 1-13

[42] Poulos, H.G. *Elastic solutions for soil and rock mechanics*. John Wiley, USA, 1974

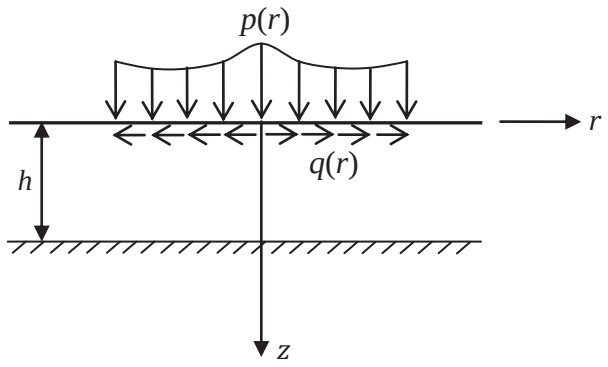

Fig.1 A three-dimensional, infinite, elastic layer subjected to axisymmetric surface loads.

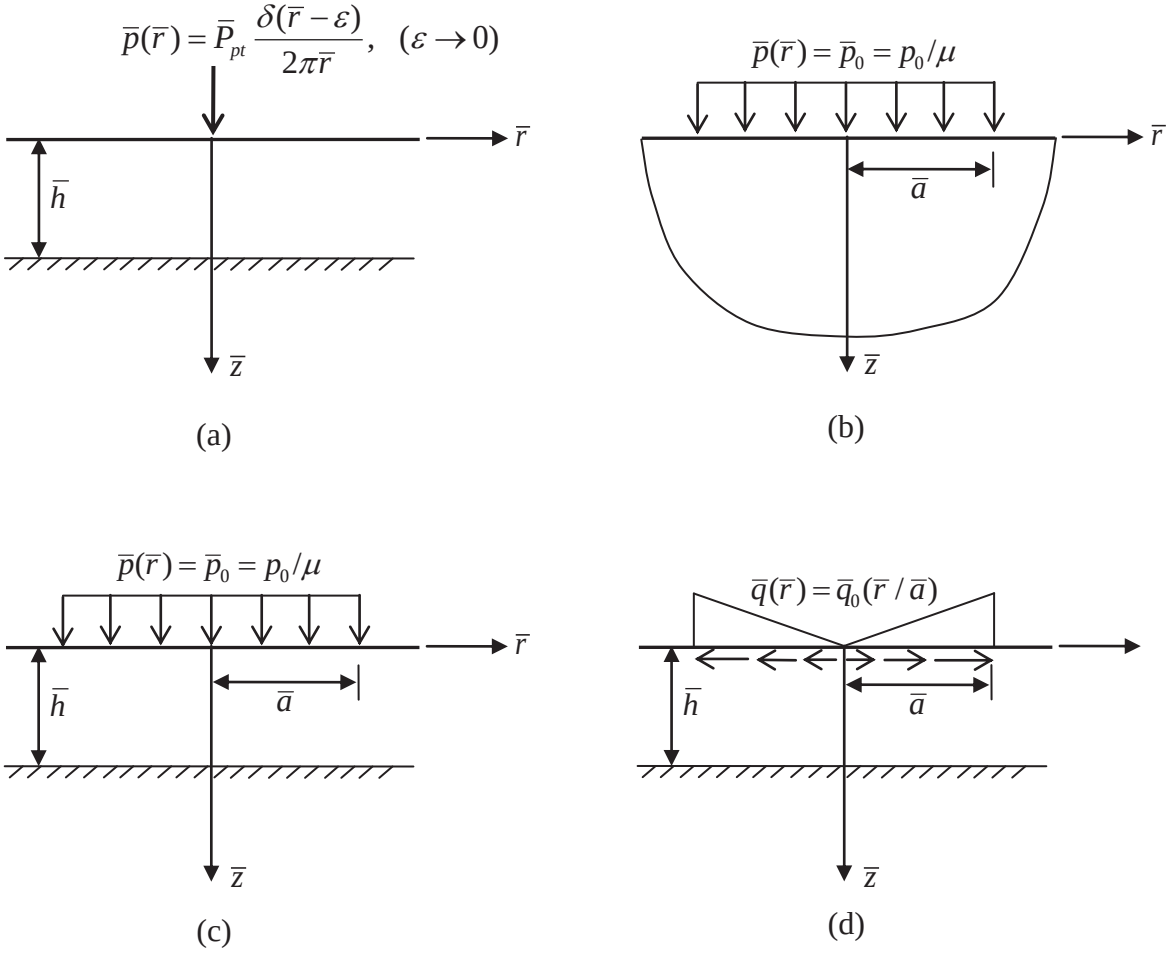

Fig. 2 (a) Three-dimensional, infinite, rigid-based, elastic layer subjected to a normal point load; (b) an elastic half-space subjected to uniformly distributed normal traction; (c) three-dimensional, infinite, rigid-based, elastic layer subjected to uniformly distributed normal traction; and (d) three-dimensional, infinite, rigid-based, elastic layer subjected to linearly distributed tangential traction.

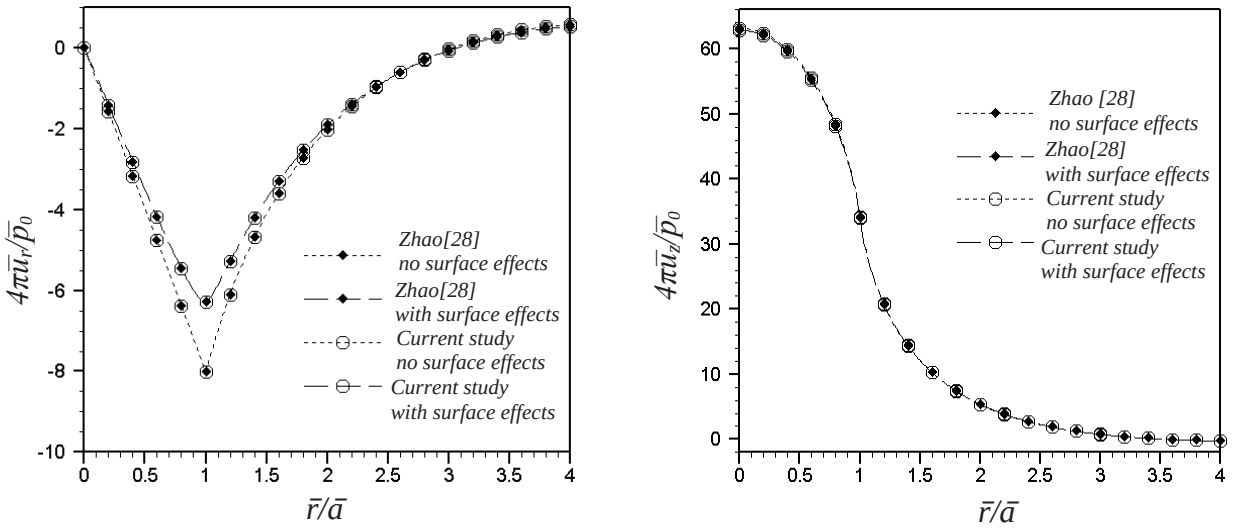

Fig. 3 Normalized displacement profiles of an infinite elastic layer under uniformly distrubuted normal traction: (a) radial displacement and (b) vertical displacement.

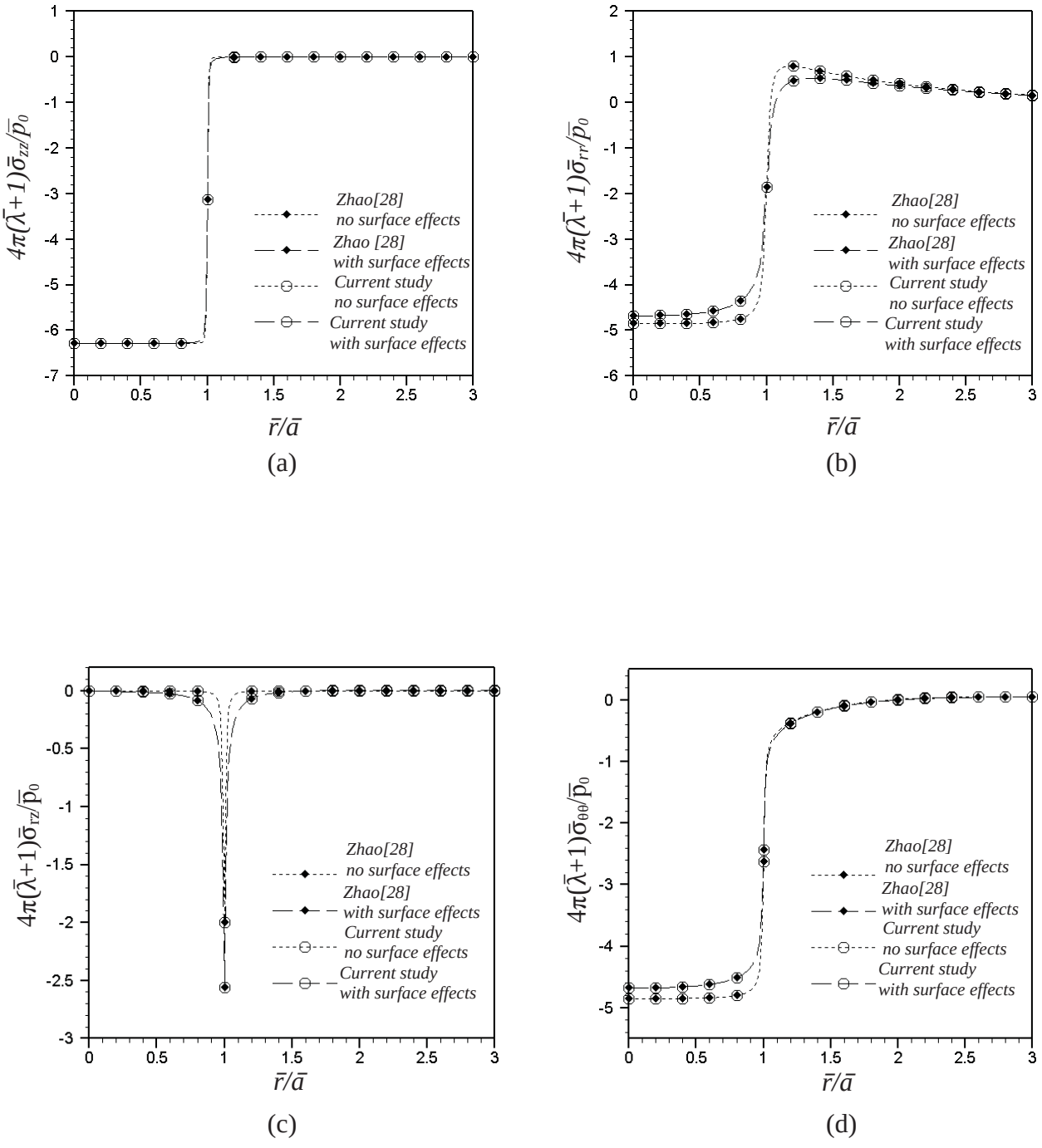

Fig. 4 Normalized stress profiles of an infinite elastic layer under uniformly distrubuted normal traction: (a) vertical stress, (b) radial stress, (c) shear stress, and (d) hoop stress.

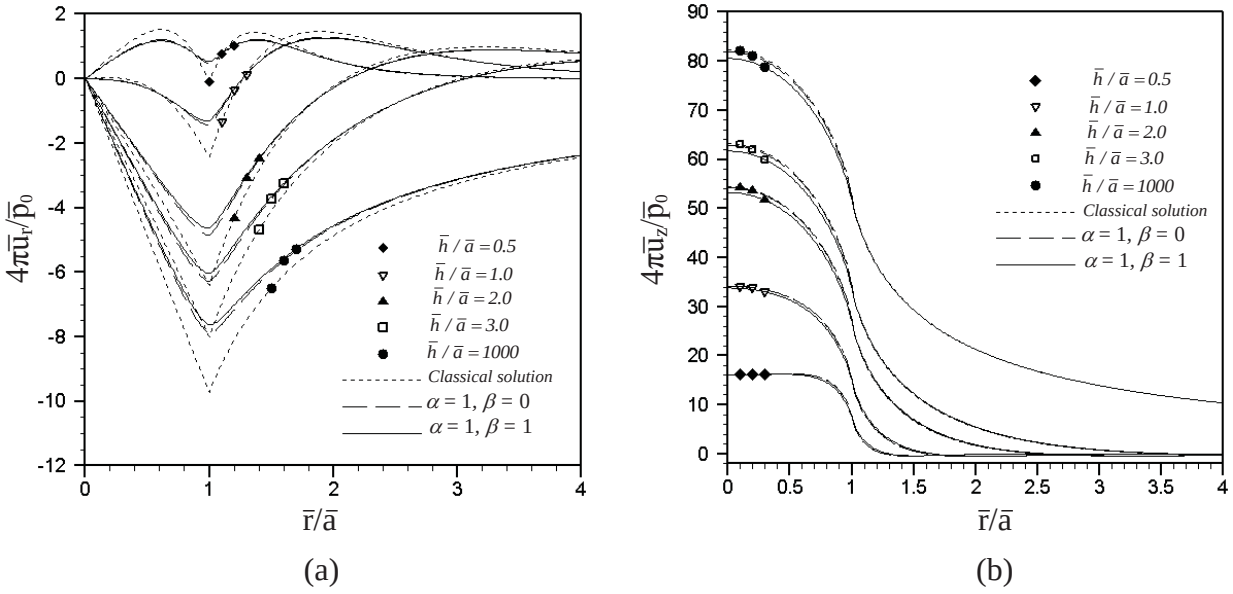

(a) (b)

Fig. 5 Normalized displacement profiles of an infinite elastic layer under uniformly distrubuted normal traction: (a) radial displacement and (b) vertical displacement.

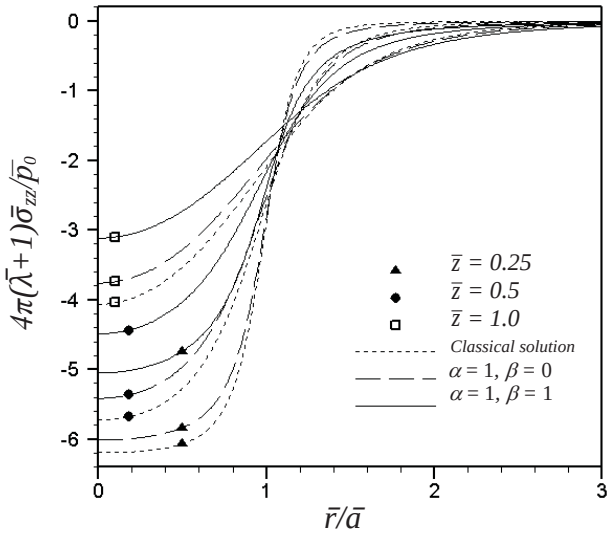

(a)

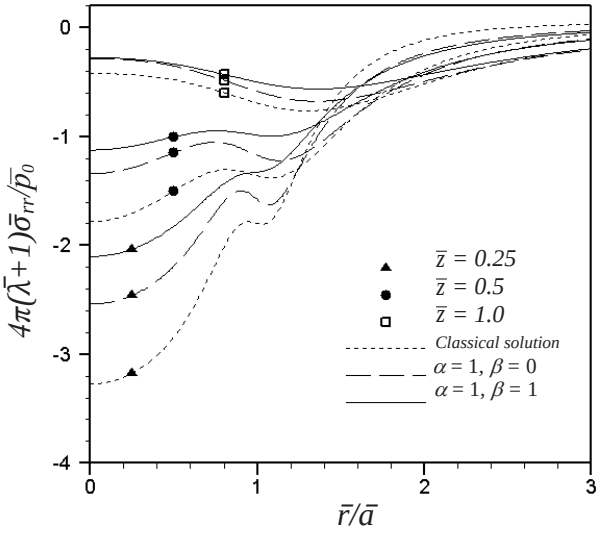

(b)

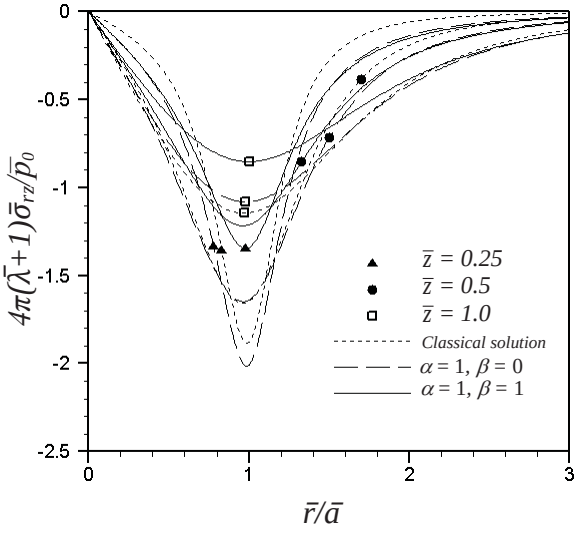

(c)

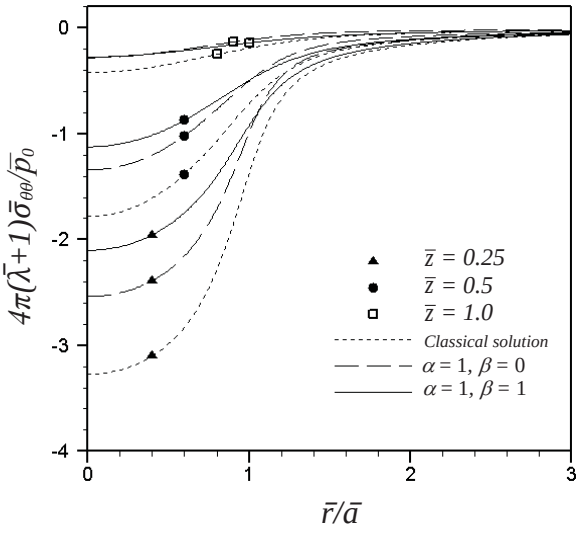

(d)

Fig. 6 Normalized stress profiles of an infinite elastic layer under uniformly distrubuted normal traction for $\bar{h}=10$ and $\bar{a}=1$: (a) vertical stress, (b) radial stress, (c) shear stress, and (d) hoop stress.

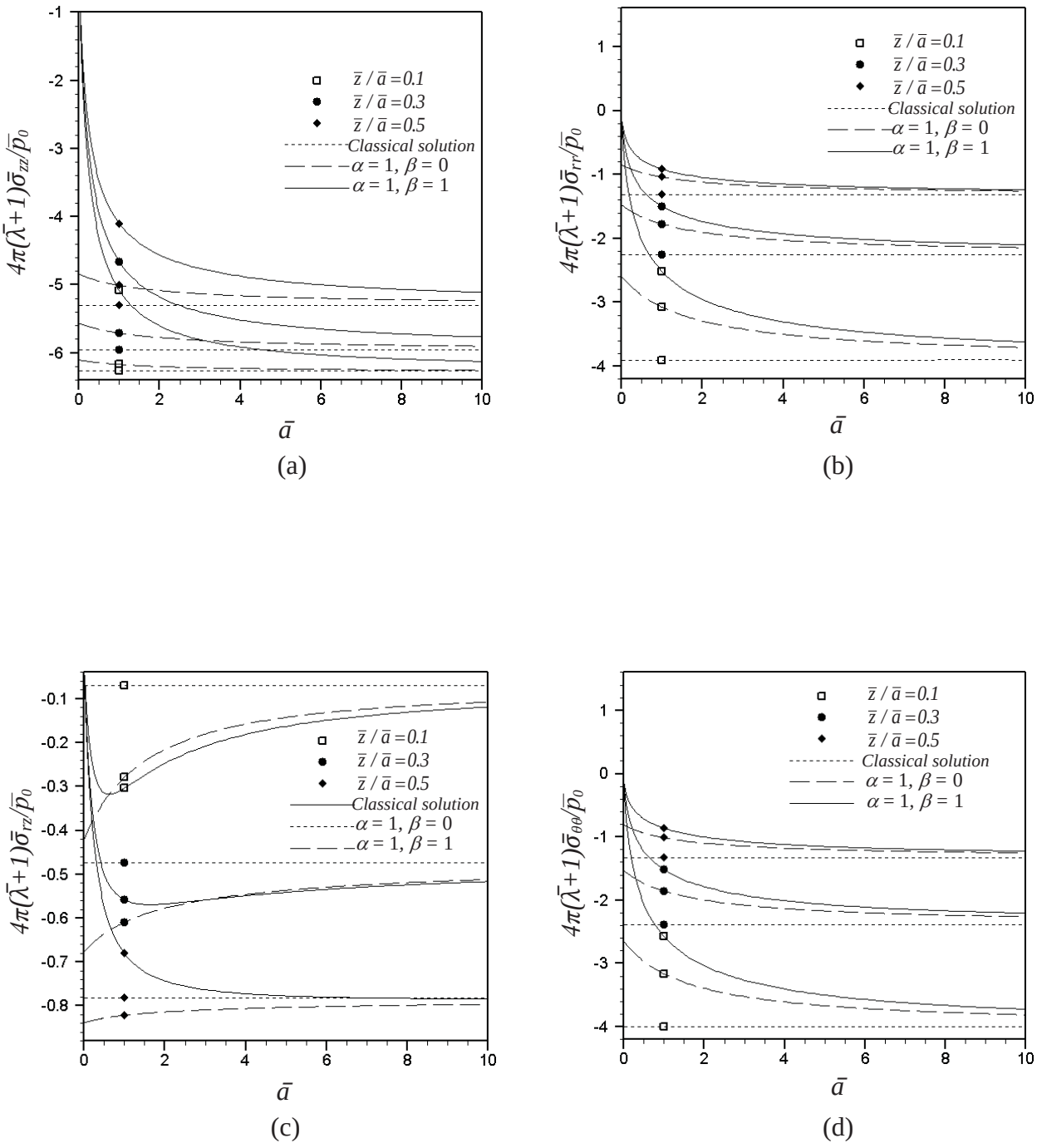

Fig. 7 Normalized stresses of an infinite elastic layer under uniformly distrubuted normal traction for $\bar{h}/\bar{a}=3$ and $\bar{r}/\bar{a}=0.5$: (a) vertical stress, (b) radial stress, (c) shear stress, and (d) hoop stress.

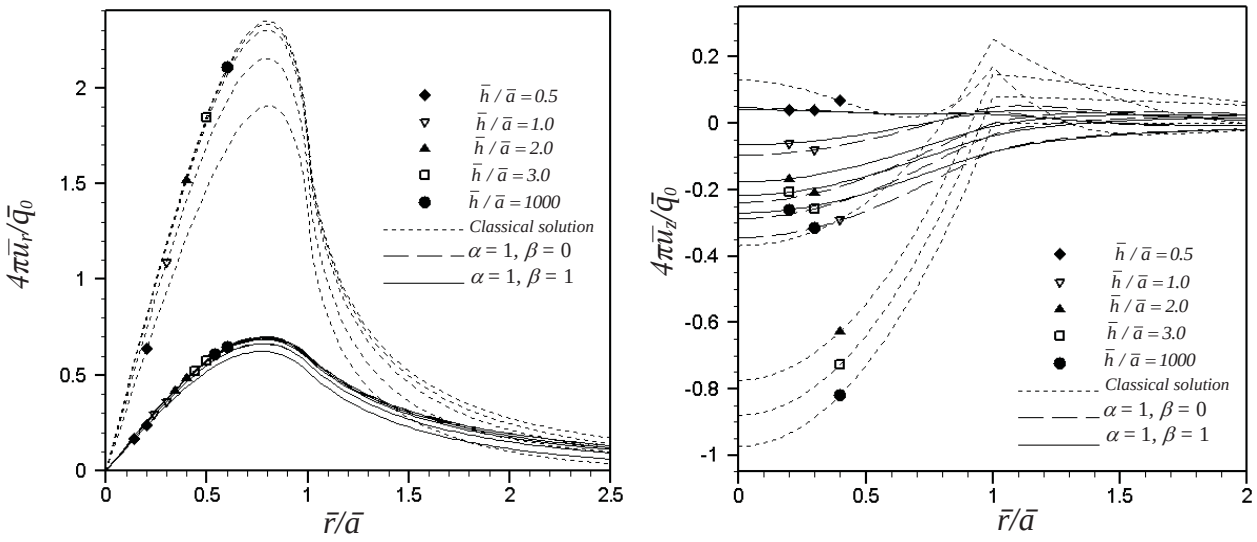

Fig. 8 Normalized displacement profiles of an infinite elastic layer under linearly distrubuted tangential load: (a) radial displacement, and (b) vertical displacement.

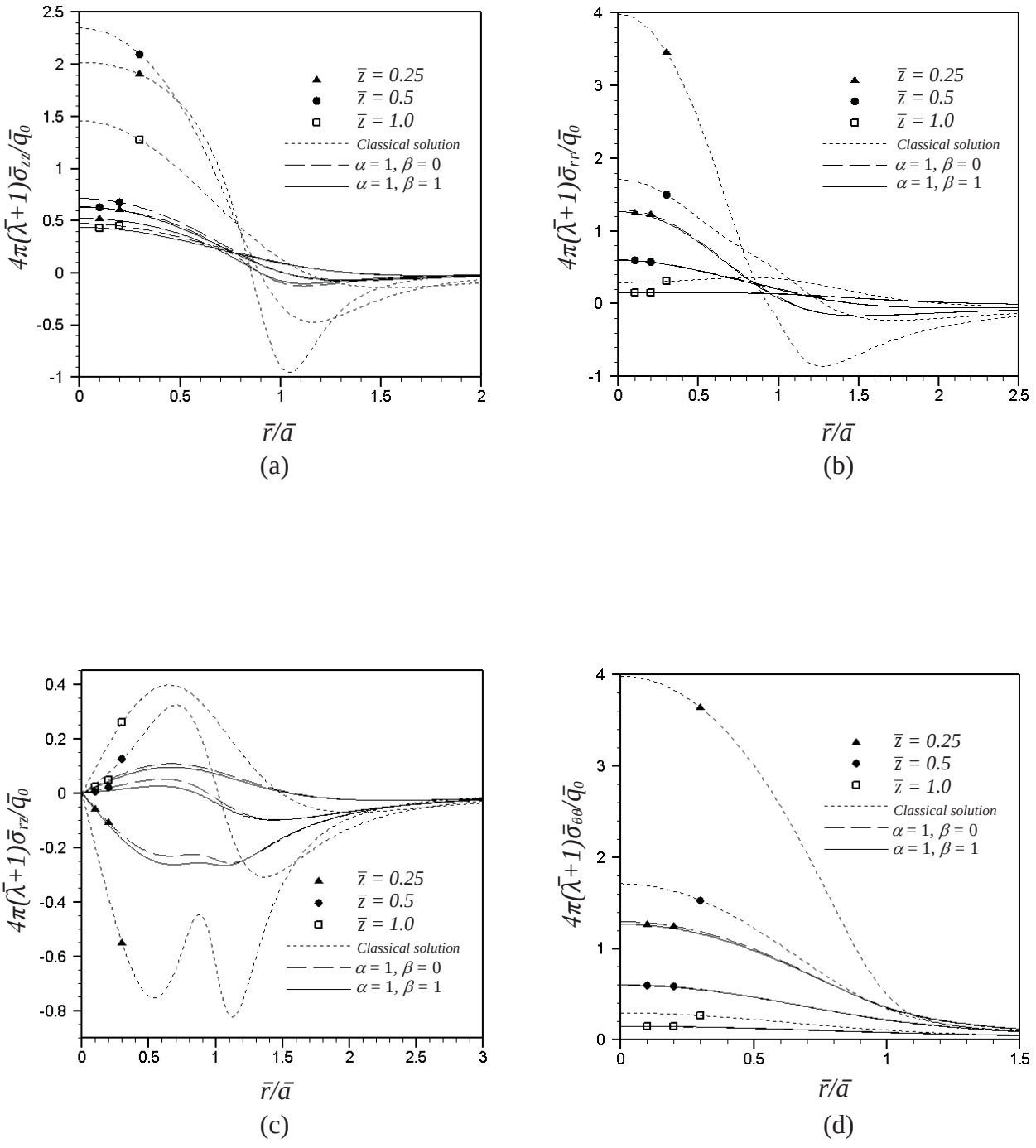

Fig. 9 Normalized stress profiles of an infinite elastic layer under linearly distrubuted tangential load for $\bar{h} = 10$ and $\bar{a} = 1$: (a) vertical stress, (b) radial stress, (c) shear stress, and (d) hoop stress.

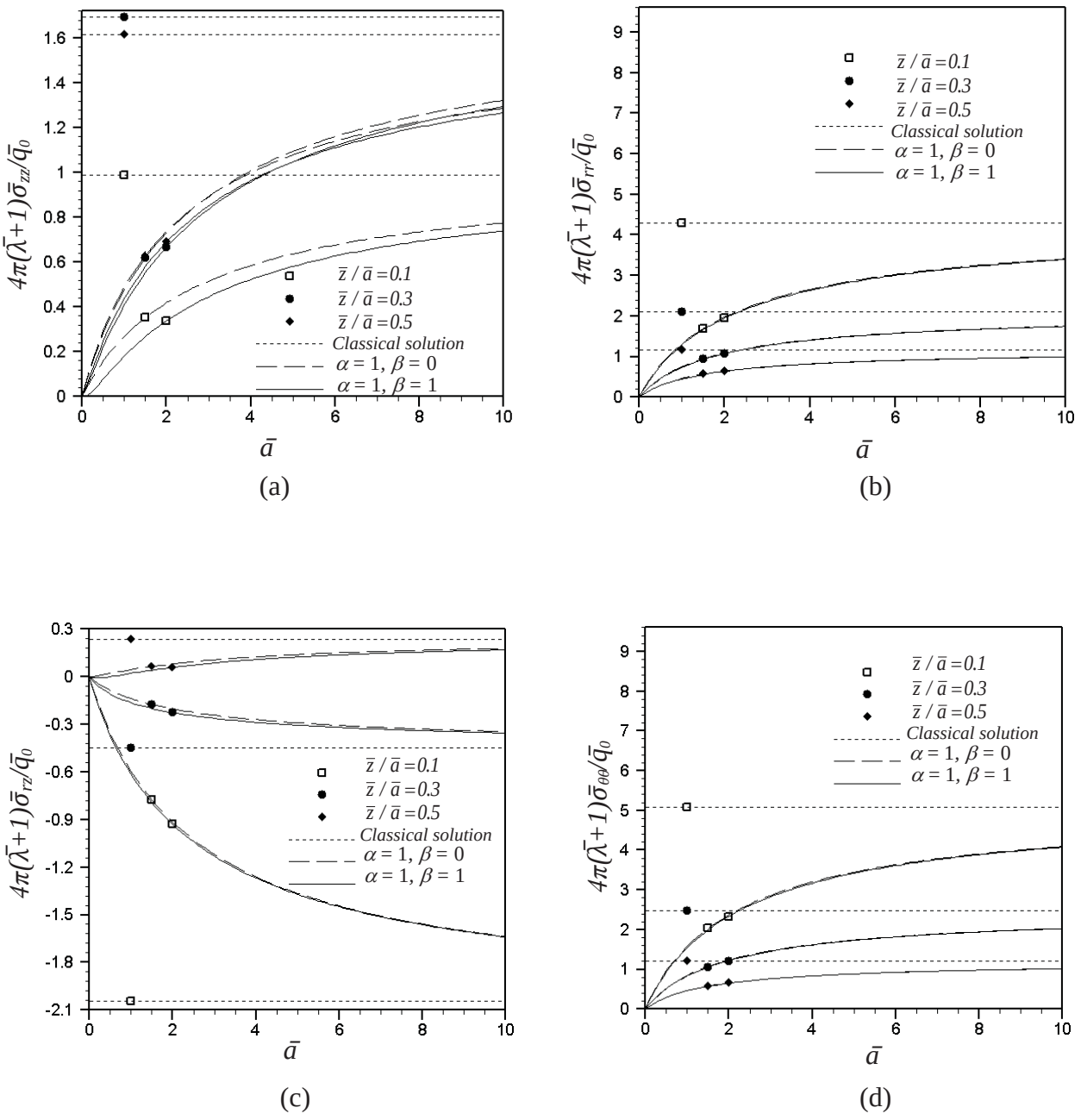

Fig. 10 Normalized stresses of an infinite elastic layer under linearly distrubuted tangential load for $\bar{h}/\bar{a}=3$ and $\bar{r}/\bar{a}=0.5$: (a) vertical stress, (b) radial stress, (c) shear stress, and (d) hoop stress.

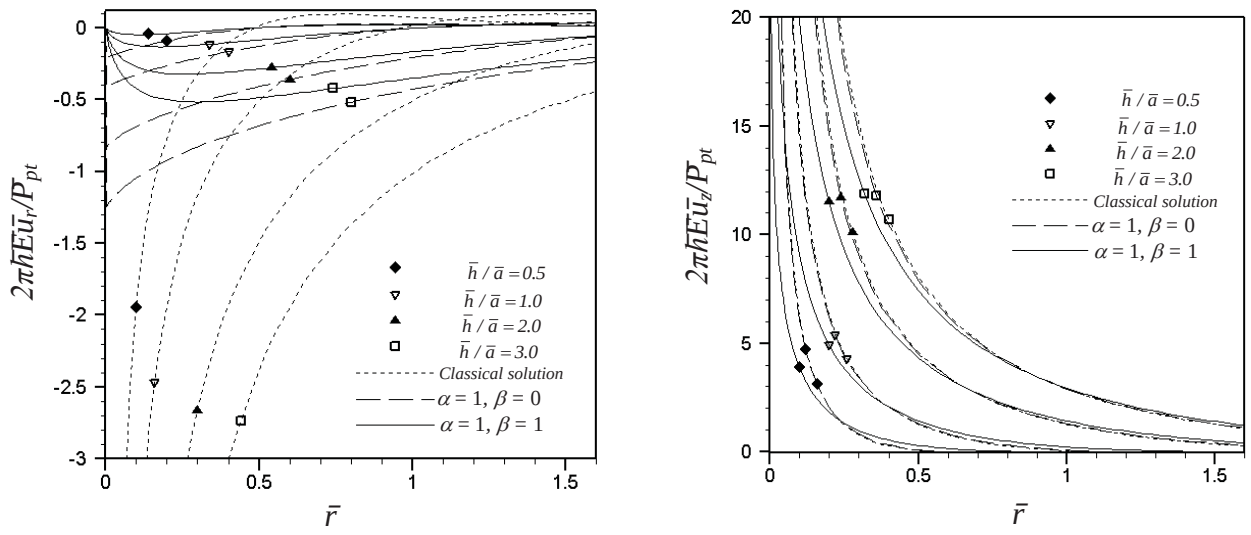

(a) (b)

Fig.11 Normalized displacement profiles of an infinite elastic layer under normal concentrated load: (a) radial displacement and (b) vertical displacement.

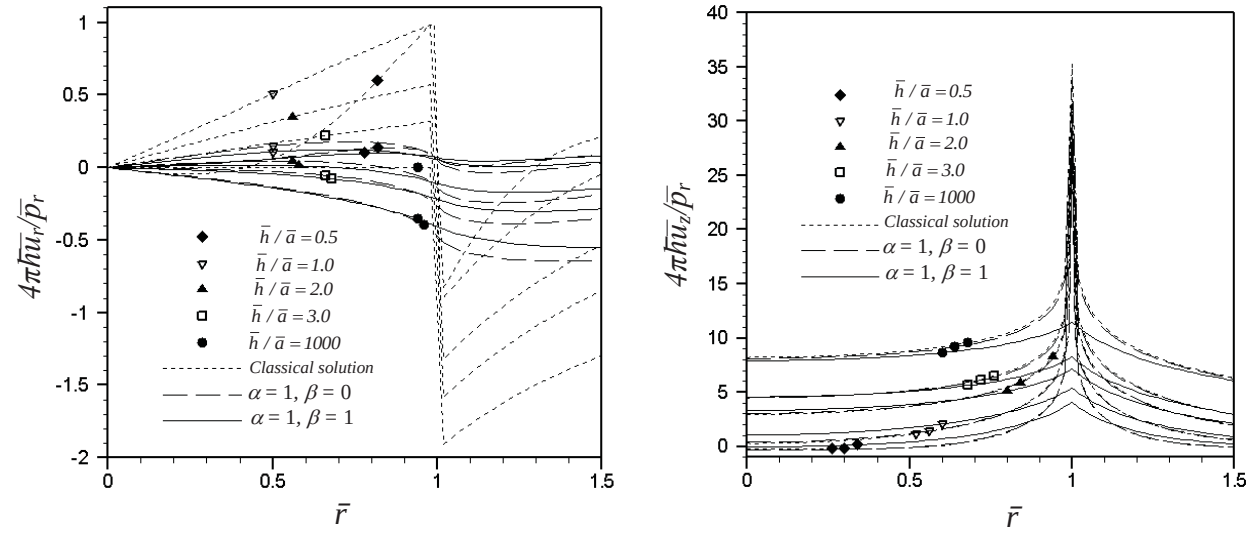

(a) (b)

Fig.12 Normalized displacement profiles of an infinite elastic layer under normal ring load: (a) radial displacement and (b) vertical displacement.

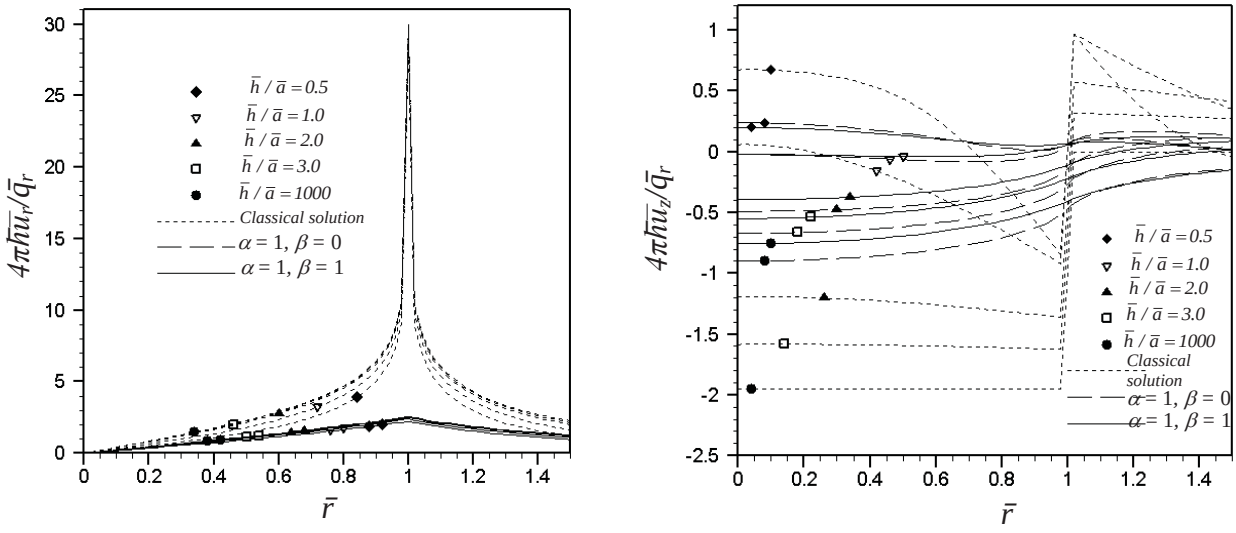

Fig. 13 Normalized displacement profiles of an infinite elastic layer under tangential ring load: (a) radial displacement and (b) vertical displacement.

Table 1 Normalized vertical and radial displacements of a three-dimensional, infinite, rigid-based, elastic layer subjected to a normal point load

$\bar{r}$	$2\pi\bar{h}\bar{E}\bar{u}_r / \bar{P}_{pt}$		$2\pi\bar{h}\bar{E}\bar{u}_z / \bar{P}_{pt}$	
	Burmister [39, 40]	Present study	Burmister [39, 40]	Present study
0.05	-14.362	-14.344	35.921	35.310
0.1	-7.124	-7.172	16.728	16.554
0.2	-3.455	-3.477	7.162	7.195
0.3	-2.184	-2.178	4.016	4.050
0.4	-1.523	-1.512	2.478	2.473
0.5	-1.064	-1.109	1.599	1.579
0.6	-0.824	-0.830	1.048	1.048
0.7	-0.62	-0.620	0.69	0.704
0.8	-0.465	-0.461	0.45	0.458

Table 2 Normalized vertical and radial stress components of a three-dimensional, infinite, rigid-based, elastic layer subjected to a normal point load

$\bar{r}$	$4\pi\bar{h}^2(\bar{\lambda}+1)\bar{\sigma}_{zz} / \bar{P}_{pt}$		$4\pi\bar{h}^2(\bar{\lambda}+1)\bar{\sigma}_{rr} / \bar{P}_{pt}$	
	Burmister [39, 40]	Present study	Burmister [39, 40]	Present study
0	300	300	-30.71	-30.72
0.1	53.08	53.06	34.75	34.75
0.2	5.415	5.395	12.5	12.49
0.3	0.994	0.974	3.347	3.344
0.4	0.293	0.273	0.614	0.611
0.5	0.124	0.103	-0.259	-0.262
0.6	0.067	0.048	-0.528	-0.530
0.7	0.041	0.025	-0.578	-0.579
0.8	0.026	0.013	-0.544	-0.544
0.9	0.016	0.006	-0.479	-0.478

Table 3 Normalized shear and hoop stress components of a three-dimensional, infinite, rigid-based, elastic layer subjected to a normal point load

$\bar{r}$	$4\pi\bar{h}^2(\bar{\lambda}+1)\bar{\sigma}_{rz}/\bar{P}_{pt}$		$4\pi\bar{h}^2(\bar{\lambda}+1)\bar{\sigma}_{\theta\theta}/\bar{P}_{pt}$	
	Burmister [39, 40]	Present study	Burmister [39, 40]	Present study
0	0	0.000	-30.71	-30.720
0.1	53	53.003	-4.342	-4.355
0.2	10.68	10.676	2.237	2.224
0.3	2.765	2.765	1.996	1.983
0.4	0.909	0.908	1.349	1.337
0.5	0.326	0.324	0.877	0.865
0.6	0.102	0.099	0.566	0.554
0.7	0.005	0.002	0.363	0.352
0.8	-0.038	-0.043	0.231	0.221
0.9	-0.056	-0.061	0.144	0.135

Table 4 Normalized displacement and stress components of a three-dimensional, infinite, elastic half-space subjected to a uniformly distributed normal traction

$\bar{z}/\bar{a}$	$2(\bar{\lambda}+1)\bar{\sigma}_{zz}/\bar{p}_0$		$2(\bar{\lambda}+1)\bar{\sigma}_{rr}/\bar{p}_0$		$2(\bar{\lambda}+1)\bar{\sigma}_{\theta\theta}/\bar{p}_0$		$\bar{u}_z/\bar{p}_0$	
	Ahlvin and Ulery [41]	Present study	Ahlvin and Ulery [41]	Present study	Ahlvin and Ulery [41]	Present study	Ahlvin and Ulery [41]	Present study
0	1.000	0.993	0.700	0.695	0.700	0.695	0.800	0.800
0.1	0.999	0.999	0.581	0.581	0.581	0.581	0.769	0.769
0.2	0.992	0.992	0.468	0.468	0.468	0.468	0.736	0.736
0.3	0.976	0.976	0.367	0.367	0.367	0.367	0.702	0.702
0.4	0.949	0.949	0.280	0.280	0.280	0.280	0.667	0.667
0.5	0.911	0.911	0.208	0.208	0.208	0.208	0.633	0.633
0.6	0.864	0.864	0.151	0.151	0.151	0.151	0.599	0.599
0.7	0.811	0.811	0.106	0.106	0.106	0.106	0.566	0.566
0.8	0.756	0.756	0.072	0.072	0.072	0.072	0.535	0.535
0.9	0.701	0.701	0.047	0.047	0.047	0.047	0.505	0.505
1	0.646	0.646	0.028	0.028	0.028	0.028	0.478	0.478
1.2	0.547	0.547	0.005	0.005	0.005	0.005	0.429	0.429
1.5	0.424	0.424	-0.010	-0.010	-0.010	-0.010	0.368	0.368
2	0.284	0.284	-0.016	-0.016	-0.016	-0.016	0.294	0.294
2.5	0.200	0.200	-0.014	-0.014	-0.014	-0.014	0.243	0.243
3	0.146	0.146	-0.012	-0.012	-0.012	-0.012	0.207	0.207
4	0.087	0.087	-0.008	-0.008	-0.008	-0.008	0.158	0.158
5	0.057	0.057	-0.005	-0.005	-0.005	-0.005	0.128	0.128
6	0.040	0.040	-0.004	-0.004	-0.004	-0.004	0.107	0.107
7	0.030	0.030	-0.003	-0.003	-0.003	-0.003	0.092	0.092